Phase Space Ray Tracing for Illumination Optics

Carmela Filosa

Cover art:
Photography:

A catalogue record is available from the Eindhoven University of Technology Library

ISBN: 978-90-386-3972-7

Phase Space Ray Tracing for Illumination Optics

PROEFSCHRIFT

ter verkrijging van de graad van doctor aan de Technische Universiteit Eindhoven, op gezag van de rector magnificus prof.dr.ir. F.P.T. Baaijens, voor een commissie aangewezen door het College voor Promoties, in het openbaar te verdedigen

door

Carmela Filosa

geboren te Torre del greco, Italië

Dit proefschrift is goedgekeurd door de promotoren en de samenstelling van de promotiecommissie is als volgt:

voorzitter:	prof.dr.
1e promotor:	prof.dr. W.L. IJzerman
copromotor:	dr. J.H.M. ten Thije Boonkkamp
leden:	

Het onderzoek of ontwerp dat in dit proefschrift wordt beschreven is uitgevoerd in overeenstemming met de TU/e Gedragscode Wetenschapsbeoefening.

Contents

List of symbols

t	time
Q	Total energy emitted from a light sorce or received by a target
Φ_r	Radiant flux
Φ	Luminous flux
λ	Wavelength
Ψ_r	Power per wavelength
$\bar{y}(\lambda)$	Luminousity function
E	Illuminance
$\mathrm{d}\Omega$	Solid angle
I	Intensity
L	Luminance
U	étendue
$\boldsymbol{\nu}$	Surface normal
n	Index of refraction of the medium in which a surface is immersed
θ	Angle between the direction of the solid angle and the normal $\boldsymbol{\nu}$
n_i	Index of refraction of the medium in which the incident ray travels
$n_\mathrm{r} = n_\mathrm{i}$	Index of refraction of the medium in which the reflected ray is located
n_t	Index of refraction of the medium in which the transmitted ray travels
$n_{\mathrm{i,t}}$	$\frac{n_\mathrm{i}}{n_\mathrm{t}}$
θ_i	Angle between the incident ray and the normal $\boldsymbol{\nu}$
θ_r	Angle between the reflected ray and the normal $\boldsymbol{\nu}$
θ_t	Angle between the transmitted ray and the normal $\boldsymbol{\nu}$
θ_c	Critical angle
$\boldsymbol{t}_\mathrm{i}$	Direction of the incident ray
$\boldsymbol{t}_\mathrm{r}$	Direction of the reflected ray
$\boldsymbol{t}_\mathrm{t}$	Direction of the transmitted ray
$\boldsymbol{\nu}_j$	Normal to the line j
t_j	Angle that the ray located on line j forms with respect to the optical axis
θ_j	Angle between the ray and the normal $\boldsymbol{\nu}_j$ to line j
n_j	Index of refraction of the medium in which line j is located

Chapter 1

Introduction

1.1 Motivation

1.2 Methods and results

1.3 Content of this thesis

Chapter 2

Illumination optics

This chapter provides some concepts of illumination optics used in this thesis. We start explaining the difference between radiometry and photometry. In particular, we focus on the photometric variables, defining them both in three and two dimensions. The reflection and refraction laws and the phenomenon of total internal reflection are explained next . The last paragraph of the chapter gives a brief introduction to Fresnel reflection.

2.1 Radiometric and photometric variables

Radiometry is concerned with the measurement of electromagnetic radiation across the entire electromagnetic spectrum. Photometry is the subfield of radiometry that takes into account only the portion of the electromagnetic spectrum corresponding to the visible light [1]. Radiometry deals with radiometric quantities. An important radiometric quantity is the radiant flux Φ_{r} (unit watt W) which is the total energy emitted from a source or received by a target per unit time:

$$\Phi_{\mathrm{r}} = \frac{\mathrm{d}Q}{\mathrm{d}t}\,, \tag{2.1.1}$$

where Q is the energy and T the time.

In illumination optics the measurement of light is given in terms of the impression that it gives on the human eye. Therefore, illumination optics deals with photometric variables rather than with radiometric variables. The most important photometric variables are defined in the following using the notation adopted by Chaves in [2]. The luminous flux Φ (unit lumen lm) is defined as the *perceived* power of light by the human eye. The radiant and the luminous flux are related by the luminous efficacy function y, unit lm/W, which defines how many lumen correspond to one Watt of power at a given wavelength. The luminous efficacy reaches its maximum at a wavelength of 555 nm where it is equal to 683 lm/W. We may normalize the luminous efficacy function with its maximum value of 683. The normalized function $\bar{y}(\lambda)$ is the luminous efficiency shown in Figure 2.1 where λ is the wavelength. It is a dimensionless quantity with a range of value between 0 and 1, [3].

The luminous flux corresponding to one Watt of radiation power at any wavelength

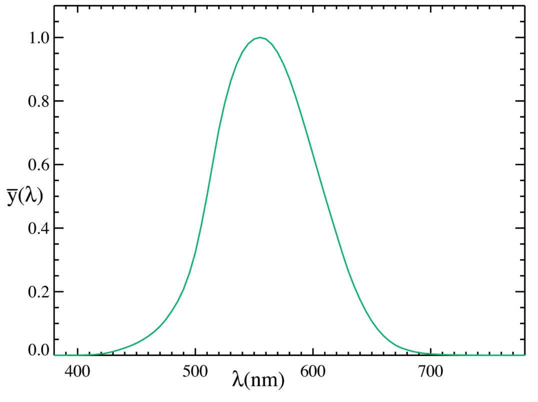

Figure 2.1: Luminosity function $\bar{y}(\lambda)$: relation between the eye's sensitivity and the wavelength of light. The luminosity function is dimensionless, [4].

is given by the product of 683 lm/W and the luminosity function at the same wavelength, i.e. $683\,\bar{y}(\lambda)$. Hence, the total luminous flux Φ has unit lumen (lm) and it is defined as:

$$\Phi = 683 \int_0^\infty \Phi_\mathrm{r}(\lambda)\bar{y}(\lambda)\mathrm{d}\lambda, \tag{2.1.2}$$

where $\Phi_\mathrm{r}(\lambda)$ is the spectral radiant flux, i.e. the radiant flux per unit wavelength (unit W/m). The luminous emittance $M = M(x,\theta)$ is the total flux emitted in all direction from a unit area. It is measured in lumens pr square meters (lm/m^2).

A beam of light can be described as a collection of parallel light rays, where a light ray can be interpreted as a path along which the energy travels. The luminous flux $\mathrm{d}\Phi$ incident on a surface is called illuminance E (unit lm/m^2) and is defined as:

$$E = E(x) = \frac{\mathrm{d}\Phi}{\mathrm{d}A}\,, \tag{2.1.3}$$

where $\mathrm{d}A$ is an infinitesimal area receiving radiation. The density of light emitted by a point source in a given direction is determined by the solid angle.

The solid angle in a given direction is expressed by a cone of rays emitted in that particular direction by a point source located at the center of the unit sphere, [3]. Let $\mathrm{d}S$ be the area on the unit sphere subtended by the cone, the infinitesimal solid angle $\mathrm{d}\Omega$ is given by:

$$\mathrm{d}\Omega = \mathrm{d}S = \sin(\theta)\mathrm{d}\theta\mathrm{d}\phi \tag{2.1.4}$$

where θ and ϕ are the polar and the azimuthal angle that the normal $\boldsymbol{\nu}$ to $\mathrm{d}A$ makes with the direction of the central line of $\mathrm{d}\Omega$, respectively (see Figure 2.2). The solid angle on the entire sphere is $\Omega = 4\pi$ and its unit is steradian sr, [5]. The luminous intensity I (unit candela cd = lm/sr) is defined as the luminous flux $\mathrm{d}\Phi$ per solid angle $\mathrm{d}\Omega$ and is given by:

$$I = I(\theta,\phi) = \frac{\mathrm{d}\Phi}{\mathrm{d}\Omega}\,. \tag{2.1.5}$$

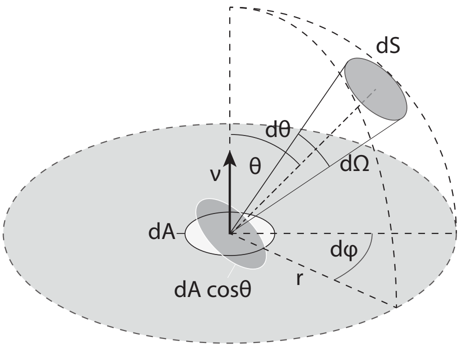

Figure 2.2: Solid angle $\mathrm{d}\Omega$ in a given direction θ with θ the angle that the central line forms with the normal to the area $\mathrm{d}A$.

Let us now consider a finite source $\mathrm{d}A$. The luminance $L = L(\boldsymbol{x}, \theta)$ (unit cd/m^2) depends both on the position and the direction, it is the luminous flux per unit solid angle $\mathrm{d}\Omega$ and per unit projected area $\cos\theta \mathrm{d}A$. L is given by:

$$L = L(\boldsymbol{x}, \theta) = \frac{\mathrm{d}\Phi}{\cos\theta \mathrm{d}A \mathrm{d}\Omega}\,. \tag{2.1.6}$$

Note that from (2.1.5) and (2.1.6) we can derive a relation between the intensity and the luminance. The intensity I emitted by the infinitesimal area $\mathrm{d}A$ is given by:

$$I = \frac{\mathrm{d}\Phi}{\mathrm{d}\Omega} = L(\boldsymbol{x}, \theta)\cos\theta \mathrm{d}A\,. \tag{2.1.7}$$

When the luminance is uniform over a finite area A, the luminous intensity emitted in the direction θ is:

$$I(\boldsymbol{x}, \theta) = I(\theta) = L(\theta)A\cos\theta\,. \tag{2.1.8}$$

Thus, when $L(\boldsymbol{x}, \theta)$ does not depend on the position and the direction (i.e. $L(\boldsymbol{x}, \theta) = L$), we obtain Lambert's cosine law:

$$I(\theta) = I_0 \cos\theta\,. \tag{2.1.9}$$

where $I_0 = I(\theta = 0) = LA$.

Finally, the étendue U (unit [m sr]) describes the ability of a source to emitt light or the capability of an optical system to receive light, [6]. The quantity $\mathrm{d}U$ is defined as:

$$\mathrm{d}U = n^2 \cos\theta \mathrm{d}A \mathrm{d}\Omega. \tag{2.1.10}$$

where n is the index of refraction of the medium in which the surface A is immersed. In optics the étendue is considered to be a volume in phase space (or an area for two-dimensional systems). This concept will be clarified in Chapter 4 in which we treat the phase space in more detail. An important property of the étendue is that it is conserved within an optical system in absence of absorption. We now show, using the approach of Chaves in [2], how conservation of this quantity can be derived. Consider a light ray emitted from an infinitesimal area $\mathrm{d}A_1$ to the area $\mathrm{d}A_2$. Suppose that

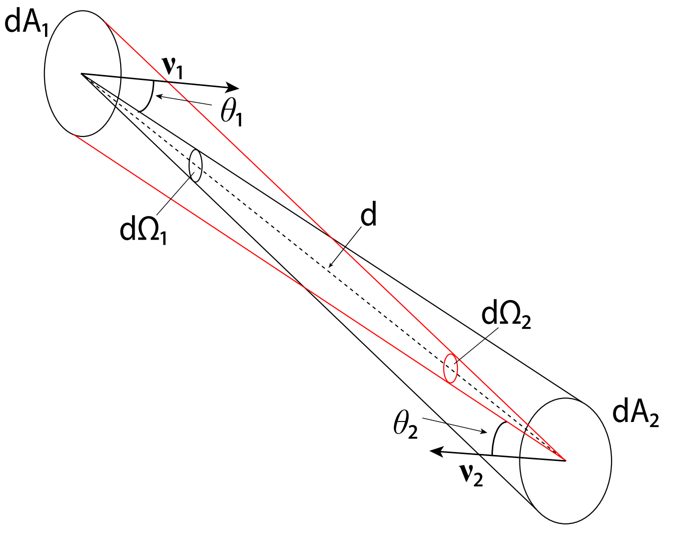

Figure 2.3: $\mathrm{d}A_1$ and $\mathrm{d}A_2$ are two surfaces with normals ν_1 and ν_2, respectively. Their centers are located at a distance d. θ_1 and θ_2 are the angles made by the central ray with the normals ν_1 and ν_2, respectively.

the centers of $\mathrm{d}A_1$ and $\mathrm{d}A_2$ are located at a distance d to each other, see Figure 2.3. Indicating with $\boldsymbol{\nu}_1$ and $\boldsymbol{\nu}_2$ the normals to the surfaces $\mathrm{d}A_1$ and $\mathrm{d}A_2$, respectively and with θ_1 and θ_2 the angles that the central ray forms with $\boldsymbol{\nu}_1$ and $\boldsymbol{\nu}_2$, respectively, the flux $\mathrm{d}\Phi_1$ passing through $\mathrm{d}A_2$ coming from $\mathrm{d}A_1$ and the corresponding solid angle $\mathrm{d}\Omega_1$ are defined as:

$$\begin{aligned} \mathrm{d}\Phi_1 &= L\cos\theta_1 \mathrm{d}A_1 \mathrm{d}\Omega_1, \\ \mathrm{d}\Omega_1 &= \frac{\mathrm{d}A_2\cos(\theta_2)}{d^2}\,. \end{aligned} \tag{2.1.11}$$

Similarly, the flux $\mathrm{d}\Phi_2$ passing through $\mathrm{d}A_1$ coming from $\mathrm{d}A_2$ is equal to:

$$\begin{aligned} \mathrm{d}\Phi_2 &= L\cos\theta_2 \mathrm{d}A_2 \mathrm{d}\Omega_2 \\ \mathrm{d}\Omega_2 &= \frac{\mathrm{d}A_1\cos\theta_1}{d^2}\,. \end{aligned} \tag{2.1.12}$$

Then from Eq. (2.1.10) we obtain the following relations:

$$\begin{aligned} \mathrm{d}U_1 &= n^2 \mathrm{d}A_1\cos\theta_1 \mathrm{d}\Omega_1 = \frac{n^2 \mathrm{d}A_1\cos\theta_1 \mathrm{d}A_2\cos\theta_2}{d^2}, \\ \mathrm{d}U_2 &= n^2 \mathrm{d}A_2\cos\theta_2 \mathrm{d}\Omega_2 = \frac{n^2 \mathrm{d}A_2\cos\theta_2 \mathrm{d}A_1\cos\theta_1`}{d^2} \end{aligned} \tag{2.1.13}$$

for $\mathrm{d}A_1$ and $\mathrm{d}A_2$, respectively. From the previous equations we can conclude that $\mathrm{d}U_1 = \mathrm{d}U_2$ and therefore the étendue $\mathrm{d}U$ is conserved along a beam of light. Since also the flux through the areas $\mathrm{d}A_1$ and $\mathrm{d}A_2$ is conserved, the following relation holds:

$$L := n^2\frac{\mathrm{d}\Phi}{\mathrm{d}U} = constant\,. \tag{2.1.14}$$

In the optical systems we will consider in this work, the source and the target are located in the same medium (air) with $n = 1$, so the luminance L equals the basic luminance $L^* = L/n^2$ at the source and the target of the system.

In this thesis we consider two-dimensional optical systems. Hence, the definitions of the photometric parameters have to be given in two dimensions. An infinitesimal line segment of length da that emits a light beam and the ray that makes an angle θ with the normal $\boldsymbol{\nu}$ are considered, see Fig. 2.4.

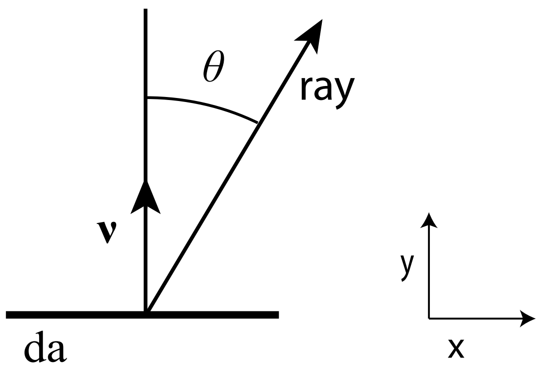

Figure 2.4: Ray emitted by an infinitesimal line segment da that makes an angle θ with respect to the line normal $\boldsymbol{\nu}$.

The two-dimensional illuminance $\big($unit $[\mathrm{lm/m}]\big)$ denotes the luminous flux falling on an infinitesimal line segment of length da and it is given by:

$$E = \frac{\mathrm{d}\Phi}{\mathrm{d}a}\ . \tag{2.1.15}$$

The luminous intensity $\big($unit $[\mathrm{lm/rad}]\big)$ is the luminous flux per angle dθ:

$$I = \frac{\mathrm{d}\Phi}{\mathrm{d}\theta}\ . \tag{2.1.16}$$

The two-dimensional luminance $\big($unit $[\mathrm{lm/(rad\cdot m)}]\big)$ is given by:

$$L = \frac{\mathrm{d}\Phi}{\cos\theta\,\mathrm{d}a\,\mathrm{d}\theta}. \tag{2.1.17}$$

Thus the following relation holds:

$$I = L(x,\theta)\cos\theta\,\mathrm{d}a \tag{2.1.18}$$

where x is a certain position at the light source da. Finally, the étendue dU (unit $[\mathrm{m}\cdot\mathrm{rad}]$) in two dimensions is given by:

$$\mathrm{d}U = n\cos\theta\mathrm{d}a\,\mathrm{d}\theta. \tag{2.1.19}$$

In order to determine the light distribution on a surface and to compute the photometric variables on that surface, we need to understand how the light emitted from the source propagates. In the field of geometric optics the light propagation is described by light rays. The propagation of a light ray traveling through different media is determined by the reflection and refraction law. In the following we introduce these two laws and we explain the total internal reflection phenomenon.

2.2 Reflection and refraction law

A light ray is described by a position vector $\boldsymbol{x}$ on a surface and a direction vector $\boldsymbol{t}$ and can be parameterized by the arc length s. Light rays travel in a homogeneous medium along straight lines, once they hit a reflective surface their direction changes. Denoting with $\boldsymbol{t}_\mathrm{i}$ the direction of the incident ray and with $\boldsymbol{\nu}$ the unit normal to the surface at the location of incidence, the direction $\boldsymbol{t}_\mathrm{r}$ of the reflected ray is given by:

$$\boldsymbol{t}_\mathrm{r} = \boldsymbol{t}_\mathrm{i} - 2(\boldsymbol{t}_\mathrm{i} \cdot \boldsymbol{\nu})\boldsymbol{\nu}\,, \tag{2.2.1}$$

where the vectors $\boldsymbol{t}_\mathrm{i}$ and $\boldsymbol{\nu}$ are unit vectors and $\boldsymbol{t}_\mathrm{i} \cdot \boldsymbol{\nu}$ indicates the scalar product between $\boldsymbol{t}_\mathrm{i}$ and $\boldsymbol{\nu}$. From Eq. (2.2.1) it follows that the vector $\boldsymbol{t}_\mathrm{r}$ is a unit vector too, indeed considering the scalar product $(\boldsymbol{t}_\mathrm{r}, \boldsymbol{t}_\mathrm{r})$ we conclude:

$$\boldsymbol{t}_\mathrm{r} \cdot \boldsymbol{t}_\mathrm{r} = \boldsymbol{t}_\mathrm{i} \cdot \boldsymbol{t}_\mathrm{i} - 4(\boldsymbol{t}_\mathrm{i} \cdot \boldsymbol{\nu})(\boldsymbol{t}_\mathrm{i} \cdot \boldsymbol{\nu}) + 4(\boldsymbol{t}_\mathrm{i} \cdot \boldsymbol{\nu})^2(\boldsymbol{\nu} \cdot \boldsymbol{\nu}) = 1. \tag{2.2.2}$$

The vectors $\boldsymbol{t}_\mathrm{i}$, $\boldsymbol{t}_\mathrm{r}$ and $\boldsymbol{\nu}$ live all in the same plane. Defining the incident angle θ_i and the reflective angle θ_r such that θ_i, $\theta_\mathrm{r} \in [0, \pi/2)$. the reflection law states that $\theta_\mathrm{i} = \theta_\mathrm{r}$, see Fig. 2.5.

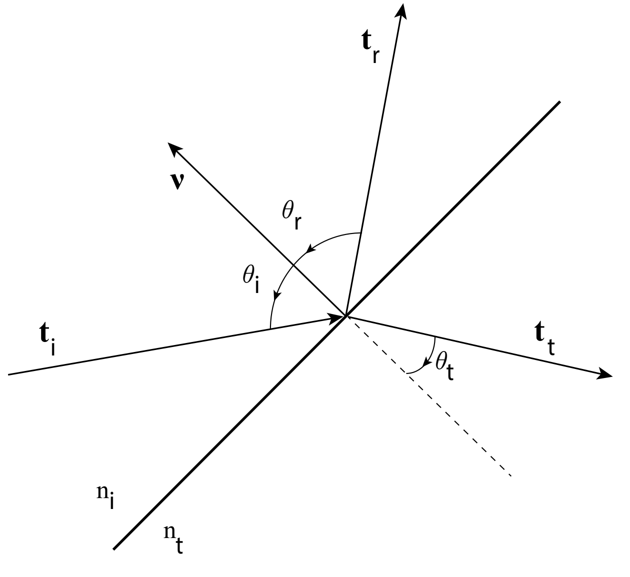

Figure 2.5: Propagation of a ray through two different media with index of refraction n_i and n_t.

When a ray propagates through two different media, its direction changes according to the law of refraction. Indicating with n_i the index of refraction of the medium in which the incident ray travels and with n_t the index of refraction of the medium of the transmitted ray, the direction $\boldsymbol{t}_\mathrm{t}$ of the transmitted ray is given by:

$$\boldsymbol{t}_\mathrm{t} = n_{\mathrm{i,t}}\, \boldsymbol{t}_\mathrm{i} + \left[\sqrt{1 - n_{\mathrm{i,t}}^2 + n_{\mathrm{i,t}}^2(\boldsymbol{\nu} \cdot \boldsymbol{t}_\mathrm{i})^2} - n_{\mathrm{i,t}}(\boldsymbol{\nu} \cdot \boldsymbol{t}_\mathrm{i})\right]\boldsymbol{\nu}\,, \tag{2.2.3}$$

where $n_{\mathrm{i,t}} = n_\mathrm{i}/n_\mathrm{t}$, [2]. Note that in Eq. (2.2.1) the direction of the normal $\boldsymbol{\nu}$ to the surface is not relevant for the computation of the direction of the reflective ray, since:

$$\boldsymbol{t}_\mathrm{r} = \boldsymbol{t}_\mathrm{i} - 2(\boldsymbol{t}_\mathrm{i} \cdot \boldsymbol{\nu})\boldsymbol{\nu} = \boldsymbol{t}_\mathrm{i} - 2(\boldsymbol{t}_\mathrm{i} \cdot -\boldsymbol{\nu})(-\boldsymbol{\nu}), \tag{2.2.4}$$

however, this is not the case for Eq. (2.2.3), therefore in the latter case we need to specify the direction of $\boldsymbol{\nu}$ which is usually chosen in such a way that the angle that it forms with the incident ray $\boldsymbol{t}_\mathrm{i}$ is smaller than or equal to $\pi/2$. Hence, if $(\boldsymbol{t}_\mathrm{i}, \boldsymbol{\nu}) \leq 0$ the normal $\boldsymbol{\nu}$ directed inside the same medium in which travels the incident ray is taken as in Fig. 2.5, otherwise the normal $-\boldsymbol{\nu}$ directed inside the same medium in which the transmitted ray will travel has to be considered.

Eq. (2.2.3) is only valid for

$$1 - n_{\mathrm{i,t}}^2 + n_{\mathrm{i,t}}^2(\boldsymbol{\nu} \cdot \boldsymbol{t}_\mathrm{i})^2 \geq 0 \tag{2.2.5}$$

which implies that

$$\frac{n_\mathrm{t}}{n_\mathrm{i}} \geq \sqrt{1 - (\boldsymbol{\nu} \cdot \boldsymbol{t}_\mathrm{i})^2} \tag{2.2.6}$$

from which we obtain:

$$n_\mathrm{t} \geq n_\mathrm{i} \sin\theta_\mathrm{i}\,. \tag{2.2.7}$$

The angle θ_c for which the equality holds is

$$\theta_\mathrm{c} = \arcsin\left(\frac{n_\mathrm{t}}{n_\mathrm{i}}\right) \tag{2.2.8}$$

and it is called the critical angle, [2]. When the incident angle θ_i is exactly equal to the critical angle θ_c, the square root in Eq. (2.2.3) is zero and the inner product $(\boldsymbol{t}_\mathrm{t}, \boldsymbol{\nu}) = 0$, hence the transmitted ray propagates parallel to the refractive surface. When $\theta_\mathrm{i} > \theta_\mathrm{c}$ the light ray is no longer refracted but is only reflected by the surface. This phenomenon is called total internal reflection (TIR). When TIR occurs, 100% of light is reflected and there is no loss of energy. Therefore, optical systems designed such that rays are reflected by TIR are very efficient. Lght that hits an ordinary refractive surface can be reflected and refracted. The energy that is reflected and refracted is determined by the Fresnel's coefficients. In the next paragraph an overview of the Fresnel coefficients is given.

2.3 Fresnel's equations

In order to derive Fresnel's equations we need to describe light as an electromagnetic wave. It is therefore useful to study the light propagation from the perspective of electromagnetic theory which gives information about the incident, reflected and transmitted radiant flux density that are denoted with E_i, E_r and E_t, respectively. Any component of the electric field $\boldsymbol{\mathcal{E}}$ can be written as

$$\boldsymbol{\mathcal{E}}(\boldsymbol{x}, t) = \boldsymbol{\mathcal{E}}_0(\boldsymbol{x}) e^{i(\boldsymbol{k}\cdot\boldsymbol{x} - \omega t)} \tag{2.3.1}$$

where $\boldsymbol{x}$ is the position vector and T is the time. The amplitude $\boldsymbol{\mathcal{E}}_0(\boldsymbol{x})$ is constant in time and $\omega = \frac{ck}{n}$ is the value of the angular frequency with c the velocity of light and n the index of refraction in which the wave is traveling, which is the ratio of the speed of light c in vacuum and the speed of light v in the material. Note that the angular frequency can be also written as $\omega = vk$, in particular when a wave travels in vacuum $n = 1$ and $\omega = ck$. The vector $\boldsymbol{k}$ has the same direction of the wave and its absolute value $|\boldsymbol{k}| = k = \frac{2\pi}{\lambda}$ is the wave number in vacuum, with λ the wavelength. Similarly, the magnetic field has the form:

$$\boldsymbol{\mathcal{B}}(\boldsymbol{x}, t) = \boldsymbol{\mathcal{B}}_0(\boldsymbol{x}) e^{i(\boldsymbol{k}\cdot\boldsymbol{x} - \omega t)}\,. \tag{2.3.2}$$

Light can be seen as an electromagnetic wave, that is an oscillating electric field $\boldsymbol{\mathcal{E}}$ and an oscillating magnetic filed $\boldsymbol{\mathcal{B}}$ which propagates always perpendicular to $\boldsymbol{\mathcal{E}}$. Th eelectric field oscillates perpendicular to the wave propagation. Light is said to be polarized if the direction of the electic field is well defined. When the electric field propagates in different directions we talk about unpolarized light. By convention, we refer to the light's polarization as the direction of the electric field $\boldsymbol{\mathcal{E}}$, [7] with respect to the incident plane that is defined by the incident and reflected rays as is shown in Fig. 2.6.

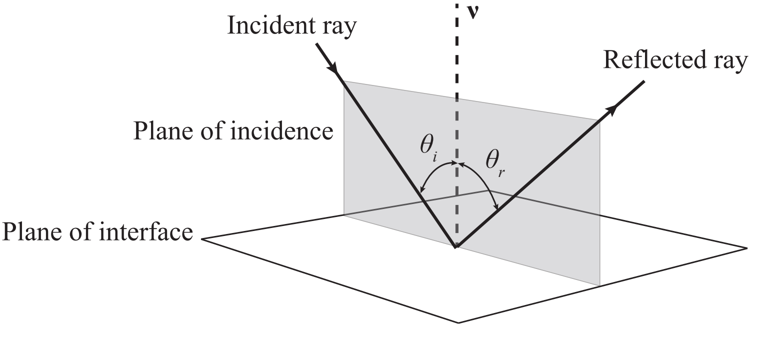

Figure 2.6: Light ray that hits a mirror located on the reflecting plane. The incident and the reflected ray leave in the same plane of the normal to the mirror that is called plane of incident.

In order to derive the Fresnel's coefficients the polarization of light must to be taken into account. Those coefficients are obtained considering Maxwell's equations and the boundary conditions due to the conservation of energy. The details of Fresnel's equations are widely explained in the literature. In the following we provide Fresnel coefficients and we briefly explain their physical interpretation. We refer the reader to [8, 9] for more details. Fresnel's coefficients can also be derived using a different approach that does not involve Maxwell's equations, this method is explained in [10]. The following particular cases of light's polarization need are considered.

1. $\boldsymbol{\mathcal{E}}$ is perpendicular to the plane of incidence (see Fig. 2.7). In this case light is said to be *s*-polarized.

2. $\boldsymbol{\mathcal{E}}$ is parallel to the plane of incidence (see Fig. 2.8). In this case light is said to be *p*-polarized.

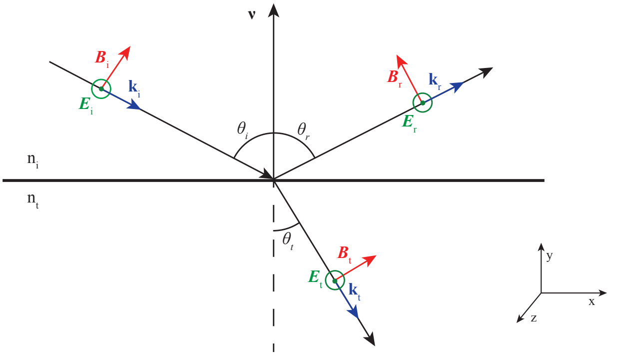

Figure 2.7: Propagation of an electromagnetic wave where $\boldsymbol{\mathcal{E}}$ is perpendicular to the incident plane. The components of $\boldsymbol{\mathcal{E}}$ are is indicated with the green circles. The components of $\boldsymbol{\mathcal{B}}$ are indicated with red arrows.

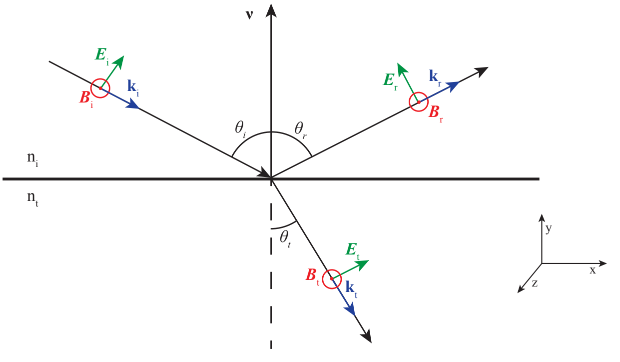

Figure 2.8: Propagation of an electromagnetic wave where $\boldsymbol{\mathcal{E}}$ is parallel to the incident plane. The components of $\boldsymbol{\mathcal{B}}$ are indicated with the red circle. The components of $\boldsymbol{\mathcal{E}}$ are indicated with greed arrows.

Energy conservation gives the boundary conditions of the electromagnetic field at the plane of the interface (which is perpendicular to the incident plane). In the following we derive Fresnel's coefficients for case 1. Similarly, the Fresnel's coefficients can be derived for the second case.

For *s*-polarized light the tangential components of $\boldsymbol{\mathcal{E}}$ and $\boldsymbol{\mathcal{B}}/\mu$ across the boundary between the two different media must be continuous. The continuity of the tangential component of $\boldsymbol{\mathcal{E}}$ leads to:

$$|\boldsymbol{\mathcal{E}}_{0\mathrm{i}}| + |\boldsymbol{\mathcal{E}}_{0\mathrm{r}}| = |\boldsymbol{\mathcal{E}}_{0\mathrm{t}}|, \tag{2.3.3}$$

while the continuity of the tangential component of $\boldsymbol{\mathcal{B}}/\mu$ gives:

$$-\frac{|\boldsymbol{\mathcal{B}}_{0,\mathrm{i}}|}{\mu_\mathrm{i}}\cos\theta_\mathrm{i} + \frac{|\boldsymbol{\mathcal{B}}_{0,\mathrm{r}}|}{\mu_\mathrm{r}}\cos\theta_\mathrm{r} = -\frac{|\boldsymbol{\mathcal{B}}_{0,\mathrm{t}}|}{\mu_\mathrm{t}}\cos\theta_\mathrm{t}, \tag{2.3.4}$$

where the negative sign in front of $|\boldsymbol{\mathcal{B}}_{0,\mathrm{i}}|$ and $|\boldsymbol{\mathcal{B}}_{0,\mathrm{t}}|$ is due to the convention that a positive direction is considered with increasing x. Since $\boldsymbol{\mathcal{B}} = \boldsymbol{\mathcal{E}}/v$, Eq. (2.3.4) can be written as

$$\frac{1}{\mu_\mathrm{i} v_\mathrm{i}}(|\boldsymbol{\mathcal{E}}_{0,\mathrm{i}}| - |\boldsymbol{\mathcal{E}}_{0,\mathrm{r}}|)\cos\theta_\mathrm{i} = \frac{1}{\mu_\mathrm{t} v_\mathrm{t}}|\boldsymbol{\mathcal{E}}_{0,\mathrm{t}}|\cos\theta_\mathrm{t}, \tag{2.3.5}$$

where we employed the fact that $v_\mathrm{i} = v_\mathrm{r}$, and $\theta_\mathrm{i} = \theta_\mathrm{r}$. Using Eq. (2.3.1) and $n = c/v$, the previous equation becomes:

$$\frac{n_\mathrm{i}}{\mu_\mathrm{i}}(|\boldsymbol{\mathcal{E}}_{0\mathrm{i}}| - |\boldsymbol{\mathcal{E}}_{0\mathrm{r}}|)\cos\theta_\mathrm{i} = \frac{n_\mathrm{t}}{\mu_\mathrm{i}}|\boldsymbol{\mathcal{E}}_{0\mathrm{t}}|\cos\theta_\mathrm{t} \tag{2.3.6}$$

Finally, assuming that $\mu_\mathrm{i} = \mu_\mathrm{t} = \mu_0$ and employing Eq. (2.3.3) we obtain:

$$\begin{aligned} r_s &= \frac{|\boldsymbol{\mathcal{E}}_{0\mathrm{r}}|_s}{|\boldsymbol{\mathcal{E}}_{0\mathrm{i}}|_s} = \frac{n_\mathrm{i}\cos\theta_\mathrm{i} - n_\mathrm{t}\cos\theta_\mathrm{t}}{n_\mathrm{i}\cos\theta_\mathrm{i} + n_\mathrm{t}\cos\theta_\mathrm{t}}, \\ t_s &= \frac{|\boldsymbol{\mathcal{E}}_{0\mathrm{t}}|_s}{|\boldsymbol{\mathcal{E}}_{0\mathrm{i}}|_s} = \frac{2n_\mathrm{i}\cos\theta_\mathrm{i}}{n_\mathrm{i}\cos\theta_\mathrm{i} + n_\mathrm{t}\cos\theta_\mathrm{t}}. \end{aligned} \tag{2.3.7}$$

The coefficients r_s and t_s are amplitude coefficients for the reflected and transmitted light. They are the perpendicular components of r and t for s-polarized light. Using Snell's law, that is $n_\mathrm{i}\sin\theta_\mathrm{i} = n_\mathrm{t}\sin\theta_\mathrm{t}$, the relations for r_s and t_s are simplified as follows:

$$\begin{aligned} r_s &= -\frac{\sin(\theta_i - \theta_t)}{\sin(\theta_i + \theta_t)}, \\ t_s &= -\frac{2\sin\theta_t\cos\theta_i}{\sin(\theta_i + \theta_t)}\;. \end{aligned} \tag{2.3.8}$$

A similar argument for the p-polarized light leads to the calculation of the parallel components r_p and t_p of r and t. In case $\boldsymbol{\mathcal{E}}$ is parallel to the plane of incidence the amplitude coefficients are:

$$\begin{aligned} r_p &= \frac{n_t\cos\theta_i - n_i\cos\theta_t}{n_i\cos\theta_t + n_t\cos\theta_i}, \\ t_p &= \frac{2n_i\cos\theta_i}{n_i\cos\theta_t + n_t\cos\theta_i}\;, \end{aligned} \tag{2.3.9}$$

and their simplified relations are:

$$\begin{aligned} r_p &= \frac{\tan(\theta_i - \theta_t)}{\theta_i + \theta_t}, \\ t_p &= \frac{2\sin\theta_t\cos\theta_i}{\sin(\theta_i + \theta_t)\cos(\theta_i - \theta_t)}. \end{aligned} \tag{2.3.10}$$

Furthermore, it can be checked that

$$\begin{aligned} t_s - r_s &= 1, \\ t_p + r_p &= 1. \end{aligned} \tag{2.3.11}$$

The amplitude coefficients are shown in Fig. 2.9 for the case in which light travels from a less dense to a more dense medium ($n_i < n_t$), that is external reflection. In Fig. 2.10 the reflection coefficients are shown for the case in which $n_i > n_t$, that is internal reflection. Note from Fig. 2.9 that r_p approaches to 0 when θ_i approaches to θ_p and it gradually decreases reaching -1 for an incident angle $\theta_i = 90°$. The angle θ_p is called Brewster's angle or polarization angle as only the component perpendicular to the incident plane is reflected at that angle and therefore light is perfectly polarized. Similarly, Fig. 2.10 shows that $r_p = 0$ for $\theta_i = \theta_{p\prime}$. It can be show that $\theta_p + \theta_{p\prime} = 90°$. Both r_p and r_s reach 1 when $\theta_i = \theta_c$. θ_c is called the critical angle. Light that hits the incident plane with an incident angle equal to or greater than the critical angle is totally reflected back and no transmitted light is observed. This phenomenon is called total internal reflection.

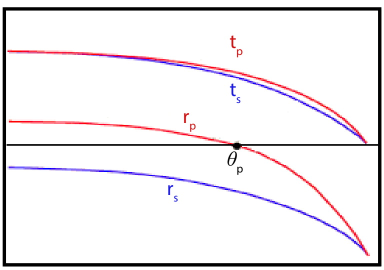

Figure 2.9: Amplitude coefficients of reflection and transmission as a function of the incident angle θ_i in the case of external reflection, i.e. $n_t < n_i$ ($n_t = 1$ and $n_i = 1.5$). θ_p is the polarization angle, [9].

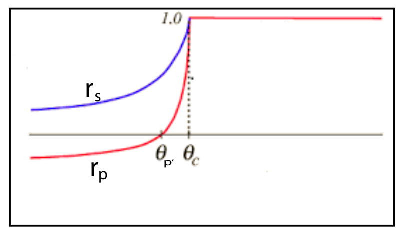

Figure 2.10: Reflection coefficients as a function of the incident angle θ_i in the case of internal reflection, i.e. $n_t > n_i$ ($n_t = 1.5$ and $n_i = 1$). $\theta_{p\prime}$ is the polarization angle and θ_c is the critical angle, [9].

The we introduce the Poynting vector $\boldsymbol{P}$ that defines the energy flux of an electromagnetic field. It is measured in [W/m^2], and it is given by:

$$\boldsymbol{P} = \frac{1}{\mu}\Big(\boldsymbol{\mathcal{E}} \times \boldsymbol{\mathcal{B}}\Big), \tag{2.3.12}$$

where $\mu = \frac{1}{\varepsilon v^2}$ is the permeability and ε the permittivity of the medium. In the following, the parameters for vacuum are indicated with the subscript 0. All quantities defined in the media of the incident, reflective and transmitted light are indicated with the subscripts i, r and t, respectively. Optical rays are perpendicular to the wave front of an electromagnetic wave and parallel to the Poynting vector, [11]. The irradiance E is defined as the average energy that crosses in unit time a unit area A perpedicular to the direction of the energy flow. Therefore, defining the average of the vector $\boldsymbol{P}$ over the time as:

$$\langle \boldsymbol{P} \rangle_T = \frac{1}{T}\int_0^T \boldsymbol{P}\mathrm{d}T \tag{2.3.13}$$

we can write the irradiance E as:

$$\boldsymbol{E} = \langle \boldsymbol{P} \rangle_t = v\varepsilon|\boldsymbol{\mathcal{E}}|^2\,. \tag{2.3.14}$$

Considering a beam of light that hits a surface such that an area A is illuminated, the incident, reflected and transmitted beams are $\boldsymbol{E}_{\mathrm{i}} A \cos\theta_{\mathrm{i}}$ $\boldsymbol{E}_{\mathrm{r}} A \cos\theta_{\mathrm{r}}$ and $\boldsymbol{E}_{\mathrm{t}} A \cos\theta_{\mathrm{t}}$, respectively. The reflectance $\mathcal{R}$ is the ratio of the reflected power to the incident power:

$$\mathcal{R} = \frac{|\boldsymbol{E}_{\mathrm{r}}| \cos\theta_r}{|\boldsymbol{E}_{\mathrm{i}}| \cos\theta_{\mathrm{i}}} = \frac{|\boldsymbol{\mathcal{E}}_{0\mathrm{r}}|^2}{|\boldsymbol{\mathcal{E}}_{0\mathrm{i}}|^2} = r^2 \tag{2.3.15}$$

where the second equality holds because $v_{\mathrm{i}} = v_{\mathrm{t}}$, $\varepsilon_{\mathrm{i}} = \varepsilon_{\mathrm{t}}$ and $\theta_{\mathrm{i}} = \theta_{\mathrm{t}}$. Similarly, the transmittance $\mathcal{T}$ is the ratio between the transmitted to the incident power:

$$\mathcal{T} = \frac{|\boldsymbol{E}_{\mathrm{t}}| \cos\theta_{\mathrm{t}}}{|\boldsymbol{E}_{\mathrm{r}}| \cos\theta_{\mathrm{r}}} = \frac{n_{\mathrm{t}} \cos\theta_{\mathrm{t}}}{n_{\mathrm{t}} \cos\theta_{\mathrm{i}}} \frac{|\boldsymbol{\mathcal{E}}_{0\mathrm{t}}|^2}{|\boldsymbol{\mathcal{E}}_{0\mathrm{i}}|^2} = \frac{n_{\mathrm{t}} \cos\theta_{\mathrm{t}}}{n_{\mathrm{t}} \cos\theta_{\mathrm{i}}} t^2 \, . \tag{2.3.16}$$

Employing total energy conservation, that is:

$$\boldsymbol{E}_{\mathrm{i}} A \cos\theta_{\mathrm{i}} = \boldsymbol{E}_{\mathrm{r}} A \cos\theta_{\mathrm{r}} + \boldsymbol{E}_{\mathrm{t}} A \cos\theta_{\mathrm{t}}, \tag{2.3.17}$$

we can easily prove that:

$$\mathcal{R} + \mathcal{T} = 1 \, . \tag{2.3.18}$$

The parallel and perpendicular components of $\mathcal{R}$ and $\mathcal{T}$ are:

$$\begin{aligned}
\mathcal{R}_p &= r_p^2, \\
\mathcal{T}_p &= \frac{n_t \cos\theta_t}{n_t \cos\theta_i} t_p^2, \\
\mathcal{R}_s &= r_s^2, \\
\mathcal{T}_s &= \frac{n_t \cos\theta_t}{n_t \cos\theta_i} t_s^2.
\end{aligned} \tag{2.3.19}$$

it can be show that

$$\begin{aligned}
\mathcal{R}_s + \mathcal{R}_p &= 1, \\
\mathcal{T}_s + \mathcal{T}_p &= 1 \, .
\end{aligned} \tag{2.3.20}$$

For normal incidence, i.e. $\theta_i = 0$, there is no polarization and Eqs. (2.3.19) lead to:

$$\begin{aligned}
\mathcal{R} = \mathcal{R}_p = \mathcal{R}_s &= \left(\frac{n_i - n_t}{n_t + n_i} \right)^2, \\
\mathcal{T} = \mathcal{T}_p = \mathcal{T}_s &= \frac{4 n_i n_t}{(n_t + n_i)^2} \, .
\end{aligned} \tag{2.3.21}$$

Many common light sources such as sunlight, halogen lighting, LED spotlights, and incandescent bulbs produce unpolarized light. In case of unpolarized light the amount of reflected and transmitted light is given by the average of reflectance $\mathcal{R}$ and transmittance $\mathcal{T}$ calculated considering first p-polarized light and then s-polarization, that is:

$$\begin{aligned}
\mathcal{R} &= \frac{\mathcal{R}_p + \mathcal{R}_s}{2}, \\
\mathcal{T} &= \frac{\mathcal{T}_p + \mathcal{T}_s}{2},
\end{aligned} \tag{2.3.22}$$

where $\mathcal{R}_p$, $\mathcal{R}_s$, $\mathcal{T}_p$ and $\mathcal{T}_s$ are given in Eqs. (2.3.19).

With this overview we conclude this chapter. The notions given in Section 2.1 will be used in the entire thesis as our goal is to study the distribution of light at the target of some optical systems. In particular we will focus on the computation of the output intensity distribution. The reflection and refraction laws explained in Section 2.2 are needed to determine how the optical system changes the ray's direction every time that it hits a surfaces (or a line in the two-dimensional case). In Chapters 3, 4, 6, 7 and 8 only systems where the reflection and refraction laws play a role are considered. Systems with Fresnel reflection are treated in the last chapter. The amount of reflected and transmitted light is calculated using the Fresnel's equation (introduced in the last paragraph of this chapter). Since, we restrict ourselves to two-dimensional systems, the value of reflectance and transmittance will be computed using Eqs. (2.3.22).

Chapter 3

Ray tracing

Optical ray tracing is a tool to calculate the transport of light within optical systems. Given an optical system and a set of rays at the source, ray tracing relates the emitted light with its output distribution. The influence of diffraction on the transport of a ray is neglected.

Although the method can be implemented for two or more dimensions and for any optical system, here we consider the two-dimensional case only. From now on, we will thus refer to optical lines instead of optical surfaces. The two-dimensional case has limitations. For example, it may not identify skew rays that are turned back by the system, with the consequence that a 2D analysis cannot guarantee a proper treatment of non meridional rays in 3D. Nevertheless, the two-dimensional case is particularly relevant because it is a good test case to demonstrate the performance of new methods. Optical designers often start with 2D systems, where only the meridional plane is taken into account because it gives a good prediction of the target distribution of the rays (see [12], chapter 4, p.50 − 65).

3.1 Ray tracing for two-dimensional optical systems

Light rays are straight lines and they are reflected or refracted by the optical components. Every ray emitted from the source is followed until it reaches the target. The ray tracing procedure is constructed such that the position and the direction of the rays are calculated on every optical line that they hit.

Given a Cartesian coordinate system (x, z), a two-dimensional optical system symmetric with respect to the z-axis is defined. Hence, usually the optical axis coincides with the z-axis. The optical system is formed by a source S, a target T and some optical components labeled with indexes j where $j \in \{2, \cdots, \mathrm{Nl}-1\}$ and Nl indicates the number of lines that form the system. S and T are indicated with the indexes 1 and Nl, respectively. The index of refraction of the medium in which line j is located is indicated with n_j. Every ray emitted by S (line 1) can hit some optical components $j \in \{2, \cdots, \mathrm{Nl}-1\}$ before reaching T (line Nl). The intersection point of the rays with line j are $(x_j, z_j)_{j=1,\cdots,\mathrm{Nl}}$ and, $\boldsymbol{s}_j = (-\sin t_j, \cos t_j)$ indicates the direction vector of the rays that leave j, with t_j the angle that the ray forms with respect to the optical axis measured counterclockwise. As we consider only forward rays, the angles

$t_j \in (-\pi/2, \pi/2)$. Therefore, a ray segment between (x_j, z_j) and (x_k, z_k) with $k \neq j$ is parameterized in real space by:

$$\boldsymbol{r}(s) = \begin{pmatrix} x_j - s \sin t_j \\ z_j + s \cos t_j \end{pmatrix} \qquad 0 < s \leq s_{\max}, \tag{3.1.1}$$

where s denotes the arc-length and $s_{\max}$ is the maximum value that it can assume. Fig. 3.1 shows an example where a single ray is traced inside a very simple optical system, the so-called two-faceted cup. The light source $\mathsf{S}= [-a, a]$ (line 1) and the

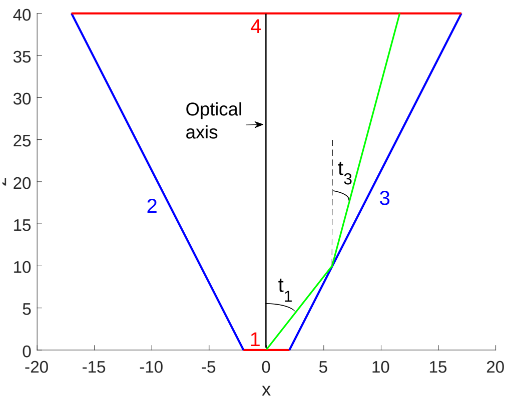

Figure 3.1: Shape of the two-faceted cup. Each line of the system is labeled with a number. The source $\mathsf{S}= [-2, 2]$ (line number 1) is located on the x-axis. The target $\mathsf{T}= [-17, 17]$ (line 4) is parallel to the source and is located at a height $z = 40$. The left and right reflectors (line 2 and 3) connect the source with the target.

target $\mathsf{T} = [-b, b]$ (line 4) are two segments normal to the z-axis, where $a = 2$ and $b = 17$. The left and right reflectors (line 2 and 3) are oblique segments that connect the source and the target. All the optical lines $j \in \{1, \cdots, 4\}$ are located in air, thus the refractive index is $n_j = 1$ for every j.

In order to compute the target photometric variables, we need to know how the optical system influences the direction of the rays when they hit an optical line. Ray tracing relates the position coordinates (x_1, z_1) and the direction vector $\boldsymbol{s}_1$ of every ray at the source S with the corresponding position $(x_{\mathrm{Nl}}, z_{\mathrm{Nl}})$ and direction $\boldsymbol{s}_{\mathrm{Nl}}$ at the target T. In the following we will often use the target coordinates of the rays thus, to simplify the notation, we do not write the subscript Nl for the target coordinates. Hence, we write (x, z) instead of $(x_{\mathrm{Nl}}, z_{\mathrm{Nl}})$, t instead of t_{Nl} and $\boldsymbol{s}$ instead of $\boldsymbol{s}_{\mathrm{Nl}}$ for the target coordinates. The ray tracing algorithm can be outlined as follows:

1. Given a ray that leaves S with initial position (x_1, z_1) and initial direction $\boldsymbol{s}_1 = (-\sin t_1, \cos t_1)$, use Eq. (3.1.1) to implement the ray parametrization $\boldsymbol{r}(s_1)$;

2. Compute the coordinates $(x_k, z_k)_{k=1\cdots,\mathrm{Nl}}$ of the intersection point of the parameterized ray $\boldsymbol{r}(s)$ with all the lines that it crosses

   a) if the shape of the lines is described by an analytical equation, the intersection points are determined analytically;

   b) if there is no analytic description for the optical lines, the intersections need to be determined using iterative methods;

3. Determine the closest line j that the forward ray encounters;
4. If $j = \mathrm{Nl}$ stop the procedure, the target ray's coordinates (x, z) and $\boldsymbol{s}$ are found.
5. Calculate the normal $\boldsymbol{\nu}_i$ to line i at the point (x_i, z_i);
6. Compute the new ray direction $\boldsymbol{s}_j$ of the ray that leaves line j at the point (x_i, z_i):
   a) if the incident line is a reflective line, $\boldsymbol{s}_j$ is given by Eq. (2.2.1);
   b) if the incident line is a refractive line, $\boldsymbol{s}_j$ is given by Eq. (2.2.3);
7. Restart the procedure from 1. for the ray that leaves line j instead of S. Consider as initial ray position coordinates (x_i, z_i) instead of (x_1, z_1) and as initial ray direction $\boldsymbol{s}_j = (-\sin t_j, \cos t_j)$ instead of $\boldsymbol{s}_1$.

The procedure explained above is repeated for every ray traced through the system, [13]. Once the target position and the direction of every ray traced are computed, the target photometric variables can be calculated using the definitions explained in the previous chapter, see section 2.1.

There are different ways to implement the ray tracing procedure. The efficiency of the ray tracing can be related with the distribution of the rays at the source. If the initial position and direction of the rays are chosen randomly we have Monte Carlo (MC) ray tracing. This is a very common method in non-imaging optics as it is very powerful and easy to implement. MC ray tracing will be explained in details in the next paragraph. If the rays are chosen from a so-called low discrepancy sequence we have the Quasi-Monte Carlo (QMC) ray tracing. This approach is discussed in Section 3.3.

3.2 Monte Carlo ray tracing

Before explain MC ray tracing we give a general introduction to the MC methods approximate computation of integrals. Given an interval $D = [\boldsymbol{a}, \boldsymbol{b}]$ with $\boldsymbol{a} = (a_1, \cdots, a_d)$ and $\boldsymbol{b} = (b_1, \cdots, b_d)$ elements of $\mathbb{R}^d$ such that $[\boldsymbol{a}, \boldsymbol{b}] = [a_1, b_1] \times \cdots \times [a_d, b_d]$, a function $f : [\boldsymbol{a}, \boldsymbol{b}] \subset \mathbb{R}^d \mapsto \mathbb{R}$ and a random variable $\boldsymbol{y} \in D$ with probability density function $\rho(\boldsymbol{y})$, the expected value of f with respect of ρ is

$$\mathbb{E}[f] = \int_D f(\boldsymbol{y})\rho(\boldsymbol{y})\mathrm{d}\boldsymbol{y}. \tag{3.2.1}$$

If ρ is a uniform probability density function,

$$\mathbb{E}[f] = \int_D f(\boldsymbol{y})\rho(\boldsymbol{y})\mathrm{d}\boldsymbol{y} = \frac{1}{(\boldsymbol{b} - \boldsymbol{a})} \int_D f(\boldsymbol{y})\mathrm{d}\boldsymbol{y}. \tag{3.2.2}$$

Monte Carlo approximates Eq. (3.2.2) by

$$S_{\mathrm{N}}(f) = \frac{1}{\mathrm{N}} \sum_{i=1}^{\mathrm{N}} f(\boldsymbol{y}_i) \tag{3.2.3}$$

$\{\boldsymbol{y}_i\}_{i=1,\cdots,\mathrm{N}} \in D$ are indipendent samples of the density function ρ, [14]. According to the strong law of large numbers,

$$\Pr\Big(\lim_{\mathrm{N}\to\infty} \frac{1}{\mathrm{N}} \sum_{i=1}^{\mathrm{N}} f(\boldsymbol{y}_i) = \mathbb{E}[f(\boldsymbol{y})]\Big) = 1. \tag{3.2.4}$$

Therefore,

$$\mathbb{E}[f] = \int_D f(\boldsymbol{y})\rho(\boldsymbol{y})\mathrm{d}\boldsymbol{y} \approx \frac{1}{\mathrm{N}} \sum_{i=1}^{\mathrm{N}} f(\boldsymbol{y}_i). \tag{3.2.5}$$

From the linearity of the expected values, it follows the obvious relation

$$\mathbb{E}[S_{\mathrm{N}}(f)] = \frac{1}{\mathrm{N}} \sum_{i=1}^{\mathrm{N}} \mathbb{E}[f] = \mathbb{E}[f], \tag{3.2.6}$$

while the Bienaymé formula leads to

$$\mathrm{Var}(S_{\mathrm{N}}) = \mathrm{Var}\left(\frac{1}{\mathrm{N}} \sum_{i=1}^{\mathrm{N}} f(\boldsymbol{y}_i)\right) = \frac{1}{\mathrm{N}^2} \sum_{i=1}^{\mathrm{N}} \mathrm{Var}\big(f(\boldsymbol{y}_i)\big) \tag{3.2.7}$$

which can be applied because the variables $\{\boldsymbol{y}_i\}_{i=1,\cdots,\mathrm{N}}$ are independent, [15], Chap. 6. Suppose that f has variance $\mathrm{Var}[f] = \mathbb{E}[(f - \mathbb{E}(f))]^2 = \sigma^2[f]$, Eqs. (3.2.6) and (3.2.7) give

$$\mathrm{Var}[S_{\mathrm{N}}(f)] = \mathbb{E}[(S_{\mathrm{N}}(f) - \mathbb{E}[S_{\mathrm{N}}(f)])^2] = \mathbb{E}[(S_{\mathrm{N}}(f) - \mathbb{E}[f])^2] = \sigma[f]^2/\mathrm{N}. \tag{3.2.8}$$

Let us denote the integration error with:

$$\mathrm{err}(f, S_{\mathrm{N}}) = \int_D f(\boldsymbol{y})\rho(\boldsymbol{y})\mathrm{d}\boldsymbol{y} - S_{\mathrm{N}}(f) = \mathbb{E}[f] - S_{\mathrm{N}}(f), \tag{3.2.9}$$

then

$$\mathbb{E}\big[|\mathrm{err}(f, S_{\mathrm{N}})|\big] \leq \sqrt{\mathbb{E}\big[\mathrm{err}(f, S_{\mathrm{N}})^2\big]} = \frac{\sigma[f]}{\sqrt{\mathrm{N}}}, \tag{3.2.10}$$

where the inequality is true because

$$\begin{aligned} \mathbb{E}\big[|\mathrm{err}(f, S_{\mathrm{N}})|\big] &= \frac{1}{\mathrm{N}}\sqrt{\left(\sum_{1=1}^{\mathrm{N}} |\mathrm{err}(f, S_{\mathrm{N}})|\right)^2} \leq \frac{1}{\mathrm{N}}\sqrt{\mathrm{N}\sum_{1=1}^{\mathrm{N}} \big(\mathrm{err}(f, S_{\mathrm{N}})\big)^2} \\ &= \sqrt{\frac{1}{\mathrm{N}}\sum_{1=1}^{\mathrm{N}} \big(\mathrm{err}(f, S_{\mathrm{N}})\big)^2} = \sqrt{\mathbb{E}\big[\mathrm{err}(f, S_{\mathrm{N}})^2\big]} \end{aligned} \tag{3.2.11}$$

and the equality follows from Eqs (3.2.8) and (5.3.5). Hence, the absolute value of the integration error is, on average, bounded by $\sigma[f]/\sqrt{\mathrm{N}}$, where $\sigma[f]$ is the standard deviation of f, [16]. It is very important to note that $\mathrm{err}(f, S_{\mathrm{N}})$ does not depend on the dimension d of f.

MC technique can be combined with the ray tracing procedure in order to compute the light distribution at the target of an optical system. In MC ray tracing the position and the direction of every ray at the source are chosen randomly. In the two-dimensional case (d=2), for every ray we need to choose one position coordinate x_1 at the source and one angular coordinate t_1 at the target, while the z_1 coordinate of every ray at the source is always given (for instance, for the two-faceted cup in Fig. 3.1, $z_1 = 0$ for every ray). Therefore, given a set of random variables $\{\boldsymbol{y}_1, \cdots, \boldsymbol{y}_N\} \in [\boldsymbol{a}, \boldsymbol{b}] \subset \mathbb{R}^2$, the initial position coordinate x_1 of the k-th ray corresponds to the first component of the k-th random variable $\boldsymbol{y}_k$ and, the starting angular coordinate t_1 of the k-th ray corresponds to the second component of the k-th random variable $\boldsymbol{y}_k$. Next, rays with those random coordinates at S are traced from S to T and, a probabilistic interpretation of the output photometric variables is provided. In particular, we are interested in the total target intensity I which is computed as a function of the angular coordinate t. The MC intensity is calculated dividing the target into intervals of equal length, the so-called bins. A partitioning $P_1 : -\pi/2 = t_0 < t_1 < \cdots < t_{\mathrm{Nb}} = \pi/2$ of the interval $[-\pi/2, \pi/2]$ is defined where Nb is the number of bins in P_1. We remark that, with a slight abuse of notation, we indicated the angular coordinates of the rays at the target (line Nl) with t_j instead of $t_{\mathrm{Nl},j}$ for every $j \in \{0, \cdots, \mathrm{Nb}\}$.

The normalized approximated intensity $I_{\mathrm{MC}}(t)$ is a piecewise constant function, whose value over the j-th bin is the ratio between the number of rays that fall into that bin $\mathrm{Nr}[t_{j-1}, t_j)$ and the total number of rays traced $\mathrm{Nr}[-\pi/2, \pi/2)$. Hence, I_{MC} is defined by

$$I_{\mathrm{MC}}(t) = \frac{\mathrm{Nr}[t_{j-1}, t_j)}{\mathrm{Nr}[-\pi/2, \pi/2)} \qquad \text{for } t \in [t_{j-1}, t_j). \tag{3.2.12}$$

The output intensity is computed from the value of the intensity $I_{\mathrm{MC}}(t_{j-1/2})$ along the direction $t_{j-1/2} = (t_{j-1} + t_j)/2$ for every bin $[t_{j-1}, t_j)_{j=1,\cdots,\mathrm{Nb}}$. The intensity $I_{\mathrm{MC}}(t_{j-1/2})$ gives an estimate of the probability that a ray reaches the target with an angle in the j-th interval $[t_{j-1}, t_j)$ of the partitioning P_1. This probability $\mathrm{P}_{j,\Delta t}$ is given by

$$\mathrm{P}_{j,\Delta t} = \Pr(t_{j-1} \le t < t_j) = \frac{\int_{t_{j-1}}^{t_j} I(t)\mathrm{d}t}{\int_{-\pi/2}^{\pi/2} I(t)\mathrm{d}t}\,, \tag{3.2.13}$$

where $I(t)$ is the output intensity (not normalized). Note that $\sum_{j=1}^{\mathrm{Nb}} \mathrm{P}_{j,\Delta t} = 1$. From the mean value theorem for the function $I(t)$, continuous in $[t_{j-1}, t_j]$, there exists a value $t_k \in [t_{j-1}, t_j]$ for which the integral at the numerator of the previous equation can be written as

$$\int_{t_{j-1}}^{t_j} I(t)\mathrm{d}t = \Delta t\, I(t_k). \tag{3.2.14}$$

Hence, $\mathrm{P}_{j,\Delta t}$ is proportional to the size $\Delta t = (t_{\mathrm{Nb}} - t_0)/\mathrm{Nb}$ of the intervals and to $I(t_k)$. Although t_k does depend on the number of bins Nb, $I(t_k)$ is constant as it is the value of the intensity on a given direction, so Eq. (3.2.14) proves that $\mathrm{P}_{j,\Delta t}$ is inversely proportional to the number of bins Nb of the partitioning P_1. Indicating with $\Phi = \int_{-\pi/2}^{\pi/2} I(t)\mathrm{d}t$ the total flux (measured in lumen [lm]), the error between the intensity $I(t_{j-1/2})$ and the averaged MC intensity $\Phi I_{\mathrm{MC}}(t_{j-1/2})/\Delta t$ is given by

$$\begin{aligned} \left| I(t_{j-1/2}) - \frac{\Phi}{\Delta t} I_{\mathrm{MC}}(t_{j-1/2}) \right| \leq & \\ & \left| I(t_{j-1/2}) - \frac{1}{\Delta t} \int_{t_{j-1}}^{t_j} I(t)\mathrm{d}t \right| + \\ & \frac{1}{\Delta t} \left| \int_{t_{j-1}}^{t_j} I(t)\mathrm{d}t - \Phi\, I_{\mathrm{MC}}(t_{j-1/2}) \right| . \end{aligned} \tag{3.2.15}$$

The first term of the right hand side of inequality (3.2.15) gives an estimate of how much the averaged intensity $\frac{1}{\Delta t}\int_{t_{j-1}}^{t_j} I(t)\mathrm{d}t$ differs from the exact intensity $I(t_{j-1/2})$. This term is due to the discretization of the target and therefore it depends on the number of bins Nb considered. Substituting $I(t)$ with its Taylor expansion around the point $t_{j-1/2}$ we obtain that this term is proportional to the square of the size of the bins. Therefore,

$$\left| I(t_{j-1/2}) - \frac{1}{\Delta t} \int_{t_{j-1}}^{t_j} I(t)\mathrm{d}t \right| = \mathrm{C}_1/\mathrm{Nb}^2 \tag{3.2.16}$$

with $C_1 > 0$ a certain constant.

The second part of the right hand side of inequality (3.2.15) gives an estimate of the MC error and therefore it depends also on the number of rays traced. In order to show how this term decreases as a function of the number of rays traced, we define the random variable $X_j(t)$ as the variable that is equal to 1 if the ray with angular coordinate t is inside the interval $[t_{j-1}, t_j)$ and equal to 0 otherwise:

$$X_j(t) = \begin{cases} 1 & \text{if} \quad t \in [t_{j-1}, t_j), \\ 0 & \text{otherwise.} \end{cases} \tag{3.2.17}$$

The Bernoulli trial X_j follows a binomial distribution $B(1, \mathrm{P}_{j,\Delta t})$. Considering a sample of Nr rays, the variable $Y_j = \sum_{k=1}^{\mathrm{Nr}} X_j(t_k)$ follows a binomial distribution $B(\mathrm{Nr}, \mathrm{P}_{j,\Delta t})$, where t_k is the angle that the k-th ray forms with the optical axis. Then, using the de Moivre-Laplace theorem, we conclude that the variable Y_j is approximated by a normal distribution with mean value $E[Y_j] = \mathrm{Nr}\mathrm{P}_{j,\Delta t}$ and variance $\sigma^2[Y_j] = \mathrm{Nr}\mathrm{P}_{j,\Delta t}(1 - \mathrm{P}_{j,\Delta t})$ when a large number of rays is considered, see [17, 18]. Thus, the normalized intensity along the direction $t_{j-1/2}$ is

$$I_{\mathrm{MC}}(t_{j-1/2}) = \sum_{k=1}^{\mathrm{Nr}} X_j(t_k)/\mathrm{Nr}. \tag{3.2.18}$$

The mean value $E[I_{\mathrm{MC}}(t_{j-1/2})] = \mathrm{P}_{j,\Delta t}$ and the variance $\sigma^2[I_{\mathrm{MC}}(t_{j-1/2})] = \mathrm{P}_{j,\Delta t}(1 - \mathrm{P}_{j,\Delta t})/\mathrm{Nr}$. Note that the standard deviation $\sigma_j := \sigma[I_{\mathrm{MC}}(t_{j-1/2})]$ is approximated by

$$\sigma_j = \sqrt{\mathrm{P}_{j,\Delta t}(1 - \mathrm{P}_{j,\Delta t})/\mathrm{Nr}} \approx \frac{\mathrm{C}_2}{\sqrt{\mathrm{Nb}\mathrm{Nr}}}\,, \tag{3.2.19}$$

for some $\mathrm{C}_2 > 0$. σ_j can be used to give an estimate of the difference between the intensity $I_{\mathrm{MC}}(t_{j-1/2})$ and its mean value $\mathrm{P}_{j,\Delta t}$. Therefore, the second term of the right hand side of relation (3.2.15) becomes

$$\begin{aligned}\frac{1}{\Delta t}\Big|\int_{t_{j-1}}^{t_j} I(t)\mathrm{d}t - \Phi\, I_{\mathrm{MC}}(t_{j-1/2})\Big| &= \\ \frac{\Phi}{\Delta t}\Big|\mathrm{P}_{j,\Delta t} - I_{\mathrm{MC}}(t_{j-1/2})\Big| &\approx \\ \frac{\Phi}{\Delta t}\sigma_j[I_{\mathrm{MC}}(t_{j-1/2})] \approx \mathrm{C}_3\frac{\mathrm{Nb}}{\sqrt{\mathrm{NbNr}}} &= \mathrm{C}_3\sqrt{\frac{\mathrm{Nb}}{\mathrm{Nr}}}\,,\end{aligned} \tag{3.2.20}$$

for some $\mathrm{C}_3 > 0$, where the approximation holds because σ_j gives a measure for the error between $I_{\mathrm{MC}}(t_{j-1/2})$ and the probability $\mathrm{P}_{j,\Delta t}$, [19]. The second approximation follows from (3.2.19). The MC error over the j-th bin is estimated by

$$\Big|I(t_{j-1/2}) - \frac{\Phi}{\Delta t}I_{\mathrm{MC}}(t_{j-1/2})\Big| = \frac{\mathrm{C}_1}{\mathrm{Nb}^2} + \mathrm{C}_4\sqrt{\frac{\mathrm{Nb}}{\mathrm{Nr}}}, \tag{3.2.21}$$

for $\mathrm{C}_4 > 0$. Considering a fixed number of bins, we obtain that the minimal error is reached when $\mathrm{Nr} \approx \mathrm{Nb}^5$. Hence, if we double the number of bins we need to trace 2^5 times more rays.

We conclude this chapter implementing MC ray tracing for the two-faceted cup the profile of which is depicted in Fig. 3.1. Considering a set of $\mathrm{Nr} = 10^3$ random rays at the source, we obtain an example of the rays distribution on the (x,t)-plane shown in Fig. 4.9a. Since the rays are chosen randomly, the distribution at the source could be different from the one shown in that figure.

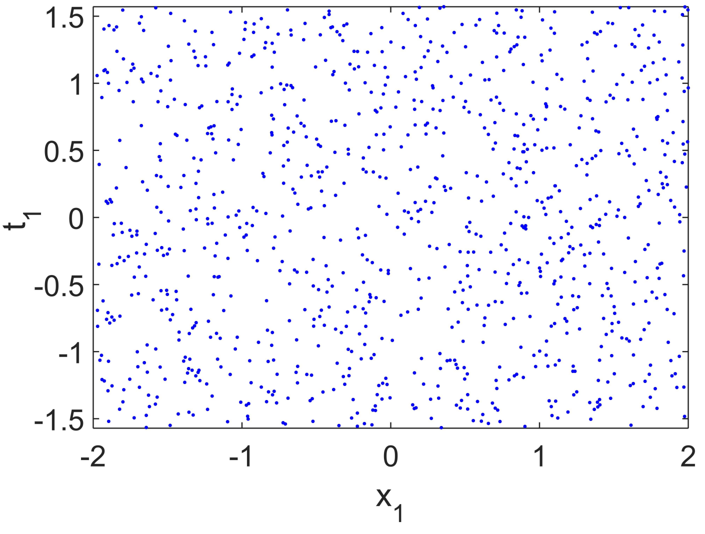

Figure 3.2: Rays at the source of the two-faceted cup with random position coordinate x and random angular coordinates t. 10^3 rays are depicted in this figure.

Then, every sample ray is traced inside the system using the ray tracing procedure.

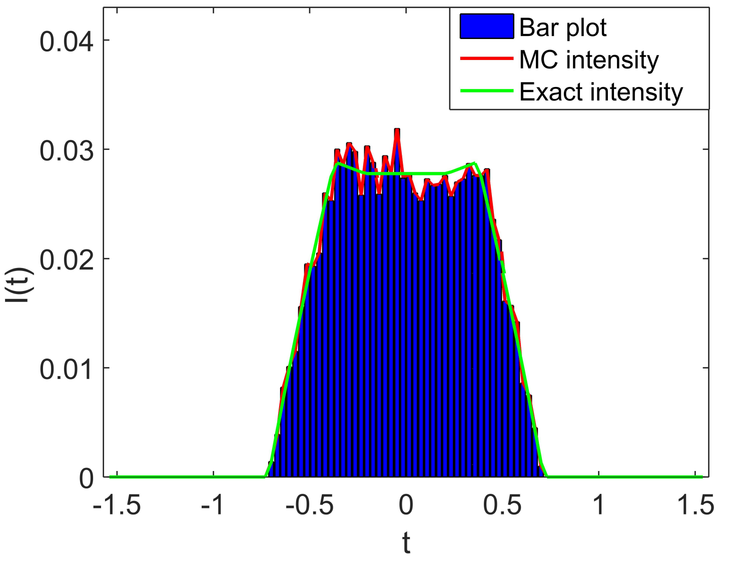

Figure 3.3: Comparison between the averaged normalized MC intensity and the normalized exact intensity.

The target $\mathsf{T} = [-b, b]$ is divided into $\mathrm{Nb} = 100$ bins. Using Eq. (3.2.12), the normalized intensity I_{MC} is computed. I_{MC} is a piecewise constant function, therefore the averaged normalized intensity $\hat{I}_{\mathrm{MC}}(t_{j-1/2})$ is given considering the values that the intensity I_{MC} assumes on the middle point $(t_{j-1/2})_{j=0,\cdots,\mathrm{Nb}}$ of every bin of the partitioning P_1. The profile of $\hat{I}_{\mathrm{MC}}$ is depicted in Fig. 3.3 with the red line. The exact intensity (analytic intensity) is shown with the green line in the same figure. MC ray tracing has the advantages of being very easy to implement and it does not require too much regularity of the function that has to be approximate. Furthermore, the error convergence does not depend on the dimension of the domain in which the function is defined. On the other hand, MC method is time consuming as the error, for a fixed number of bins, has a speed of convergence of order $O(1/\sqrt{\mathrm{Nr}})$. Thus, to decrease the error of a factor 10 we need to increase the number of rays of a factor 100. As, MC ray tracing is a binning procedure, the error depends also on the number of bins in which the target is divided. It is a statistical procedure and the error bound is only a *probabilistic* error as shown in Eq. (3.2.10). This means that, to calculate the value of the error, several simulations have to be repeated and the average of the errors obtained in every simulation has to be calculated.

Instead of considering random variables, the sample of rays can be defined in such a way that they have a regular distribution on the domain $D \subseteq \mathbb{R}^d$ of the function f of which we want to compute the integral. Methods based on this deterministic approach are called Quasi Monte Carlo (QMC) methods. They can be seen as an improvement of MC method.

3.3 Quasi-Monte Carlo ray tracing

Quasi-Monte Carlo (QMC) methods were proposed for the first time in the 1950s in order to speed up MC. Likewise MC methods, QMC procedures can be used to approximate the integral of a function.

This chapter provides basic notions about uniform distributed theory, it follows Chapter 2 of [16]. It is useful to restrict ourselves to intervals of the form $[\boldsymbol{a}, \boldsymbol{b}) \subseteq [0,1)^d$ and introduce the concept of sequences uniformly distributed modulo one.

Definition 3.3.1. An infinite sequence $\{y_n\}_{n\in\mathbb{N}_0} \in [0,1)^d$ is said to be *uniformly distributed modulo one* (or equidistributed), if for every interval $[\boldsymbol{a}, \boldsymbol{b}) \subseteq [0,1)^d$ it holds

$$\lim_{\mathrm{N}\to\infty} \frac{\mathrm{card}(A([\boldsymbol{a}, \boldsymbol{b}), \mathrm{N}))}{\mathrm{N}} = \lambda_d([\boldsymbol{a}, \boldsymbol{b})) \tag{3.3.1}$$

where $\mathrm{card}(A([\boldsymbol{a}, \boldsymbol{b}), \mathrm{N}))$ is the cardinality of the following set

$$A([\boldsymbol{a}, \boldsymbol{b}), N) = \{n \in \mathbb{N}_0 : 0 \leq n \leq \mathrm{N} - 1 \text{ and } y_n \in [\boldsymbol{a}, \boldsymbol{b})\}, \tag{3.3.2}$$

and $\lambda_d([\boldsymbol{a}, \boldsymbol{b})) = \prod_{j=1}^{d}(b_j - a_j)$ is the d-dimensional Lesbegue measure of the interval $[\boldsymbol{a}, \boldsymbol{b})$.

Given a sequence $\{\boldsymbol{y}_i\}_{i=1,\cdots,\mathrm{N}} \in [0,1)^d$ uniformly distributed modulo one and a Riemann integrable function $f : [0,1]^d \mapsto \mathbb{R}$, the integral of f can be approximate as the average of the values that f assumes on $\{\boldsymbol{y}_i\}$ for every $j = \{1, \cdots, \mathrm{N}\}$, that is:

$$\lim_{\mathrm{N}\to\infty} \frac{1}{\mathrm{N}} \sum_{i=1}^{\mathrm{N}} f(y_i) = \int_{[0,1]^d} f(\boldsymbol{y}) \mathrm{d}\boldsymbol{y}. \tag{3.3.3}$$

The idea of QMC methods is to generate the set of points in $[\boldsymbol{a}, \boldsymbol{b}]$ such that they are not randomly distributed but also not exactly uniformly distributed. To measure how much the distribution of these points differs from a uniform distribution, the concept of discrepancy was introduced. Intuitively, discrepancy measures how much the samples differ from a uniform distribution. Therefore, random sequences have a very high discrepancy, while uniform distributed sequences have zero discrepancy. The definition of discrepancy in more mathematical terms is provided below.

Definition 3.3.2. Given a set $\mathcal{S} = \{\boldsymbol{y}_1, \cdots, \boldsymbol{y}_\mathrm{N}\}$ of N points in $[0,1)^d$. The discrepancy $D_\mathrm{N}(\mathcal{S})$ of $\mathcal{S}$ is defined as

$$D_\mathrm{N}(\mathcal{S}) = \sup_{\boldsymbol{a},\boldsymbol{b}\in[0,1)^d} \left| \frac{\mathrm{card}(A([\boldsymbol{a}, \boldsymbol{b}), \mathrm{N}))}{\mathrm{N}} - \lambda_d([\boldsymbol{a}, \boldsymbol{b})) \right| \tag{3.3.4}$$

where $\lambda_d([\boldsymbol{a}, \boldsymbol{b})) = \prod_{j=1}^{d}(b_j - a_j)$ is the d-dimensional Lesbegue measure of the interval $[\boldsymbol{a}, \boldsymbol{b})$.

Often, it is enough to consider the discrepancy in the intervals $[0, \boldsymbol{a}) \subseteq [0,1)^d$, in that case we talk about star discrepancy.

Definition 3.3.3. Let $\mathcal{S} = \{\boldsymbol{y}_1, \cdots, \boldsymbol{y}_\mathrm{N}\}$ be a set of N points in $[0,1)^d$. The star discrepancy $D^*_\mathrm{N}(\mathcal{S})$ of $\mathcal{S}$ is defined as:

$$D^*_\mathrm{N}(\mathcal{S}) = \sup_{\boldsymbol{a}\in[0,1)^d} \left|\frac{\mathrm{card}(A([0,\boldsymbol{b}),\mathrm{N}))}{\mathrm{N}} - \lambda_d([0,\boldsymbol{a}))\right| \tag{3.3.5}$$

Sequences constructed such that the corresponding star discrepancy has an order of $O(\log(\mathrm{N})^d/\mathrm{N})$ are called *low-discrepancy sequences*, [14]. An important results shows that, using a low-discrepancy sequence $\{\boldsymbol{y}_i\}_{i=1,\cdots,\mathrm{N}}$, the absolute error of a QMC algorithm:

$$\mathrm{err}(f, S_\mathrm{N}) = \left|\int_{[0,1)^d} f(\boldsymbol{y})\mathrm{d}\boldsymbol{y} - \frac{1}{\mathrm{N}}\sum_{i=1}^{\mathrm{N}} f(\boldsymbol{y}_i)\right| \tag{3.3.6}$$

can be bounded by the product of a term that depends on f and another term that depends on the discrepancy of the set $\{\boldsymbol{y}_i\}_{i=1,\cdots,\mathrm{N}}$. This is the result provided by the Koksma-Hlawka inequality which gives the following estimation of the error:

$$\left|\int_{[0,1)^d} f(\boldsymbol{y})\mathrm{d}\boldsymbol{y} - \frac{1}{\mathrm{N}}\sum_{i=1}^{\mathrm{N}} f(\boldsymbol{y}_i)\right| \leq V(f)D^*_\mathrm{N}(\mathcal{S}) \tag{3.3.7}$$

where $V(f)$ is the so-called variation function of f in the sense of Hardy-Krause (see [20, 21] for details). From the definition of low-discrepancy sequences and from the Koksma-Hlawka inequality we can state that:

$$\mathrm{err}(f, S_\mathrm{N}) < C\frac{\log(\mathrm{N})^d}{\mathrm{N}}. \tag{3.3.8}$$

For small dimensions d, QMC performs much better than MC methods, while for large dimension d the factor log(N) could be very big. The convergence of QMC method depends on the of low-discrepancy sequence that is used.

There are many ways to generate low-discrepancy sequences. The most common QMC approach uses the so-called Sobol' sequence. The algorithm for generating Sobol' sequences is widely explained in the literature, (see for instance , [22]). In appendix A we give an overview of how these kind of sequences can be constructed.

Based on QMC methods, QMC ray tracing considers as position and angular coordinates of the rays at the source, the coordinates of the corresponding points of a low-discrepancy sequence. Therefore, to implement QMC ray tracing in two-dimensions we need to construct a low-discrepancy sequence in two-dimensions. Given, for instance, a Sobol' sequence $\{\boldsymbol{y}_i\}_{i=1,\cdots,\mathrm{N}}$ with $\boldsymbol{y}_i \in [0,1)^2$ for every $i = 1, \cdots, \mathrm{N}$, the two dimensional QMC ray tracing consider the position coordinate of the i-th ray at the source equal to the first component of the i-th point $\boldsymbol{y}_i$ of the Sobol' sequence $\{\boldsymbol{y}_i\}_{i=1,\cdots,\mathrm{N}}$ and, the direction coordinate of the i-th ray at the source equal to the second component of the i-th point $\boldsymbol{y}_i$ of the same sequence. A set of $\mathrm{Nr} = \mathrm{N}$ rays with these initial coordinates is traced within the system and, once the target coordinates of all the rays traced are computed, the output intensity is calculated using the same approach used for MC ray tracing, see Eqs 3.2.12 and 3.2.15. The difference between MC and QMC ray tracing consists only on the choice of the initial ray set.

In Fig. 4.9b we show the distribution of the position and direction coordinates of the rays at the source of the two-faceted cup in Fig. 3.1. A set of 10^3 rays generated from a $2D$ Sobol sequence is considered, the coordinates (x_1, t_1) of every ray at the source are depicted with blue dots. We note that the rays have a regular distribution on the (x, t)-plane. We need to remark that, for the system in Fig. 3.1, $x_1 \in [-2, 2]$ and the angular coordinates $t_1 \in [-\pi/2, \pi/2]$. Since Sobol' sequences are defined inside intervals of the $[\boldsymbol{a}, \boldsymbol{b}) \subseteq [0, 1)^2$, we scaled the points of the sequence $\boldsymbol{y}_i$ in order to take all the possible positions and directions that the rays tan assume at the source.

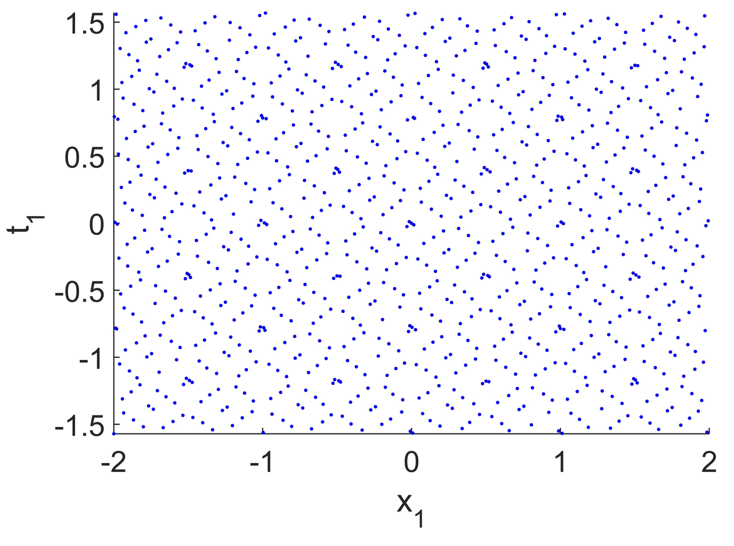

Figure 3.4: 10^3 rays at the source of the two-faceted cup with position x_1 and angular t_1 coordinates with a regular distributions. They are distributed as the points of a Sobol' sequence in two-dimensions.

Dividing the target into Nb $= 100$ bins, we computed the target intensity. In Fig. 3.5 we show the profile of the output intensity at the target of the two-faceted cup computed using QMC ray tracing with 10^4 rays. The QMC intensity is depicted with the red line. It is compared to the analytic intensity shown in the same figure with the green dotted line. A comparison between Fig. 3.3 and 3.5 gives the insight that for the two-faceted cup and for a set of Nr $= 10^4$ rays, QMC ray tracing performs better than MC ray tracing. In order to show the accuracy obtained using MC and QMC methods, we calculate the target intensity gradually increasing the number of rays traced inside the two-faceted cup. The error between the approximates intensity and the analytic intensity is calculated for every sample of rays. The speed of convergence for MC is shown in Fig. 3.6 with the red, while the behavior of QMC ray tracing is depicted in the same picture with the blue line. The results shown for a simple optical system are indeed consistent with what we expected from the theoretical analysis. Although QMC ray tracing is an improvement of MC ray tracing for small dimensions, it has two main disadvantages. First, its convergence is strongly related with the dimension in which it is implemented. Second, likewise MC ray tracing, QMC ray tracing is a binning procedure, therefore the error still depends on the number of bins in which the target is divided and only the averaged value of the intensity over every bin is provided.

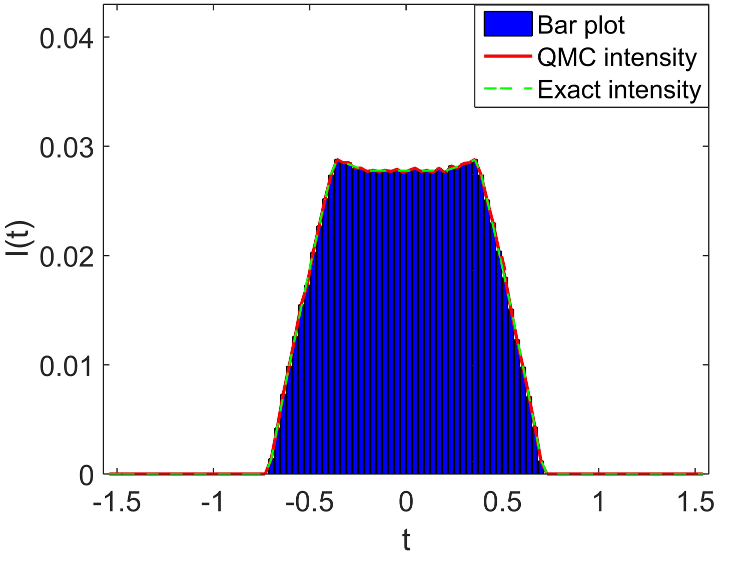

Figure 3.5: QMC intensity for the two-faceted cup obtained tracing $\mathrm{Nr} = 10^4$ rays and dividing the target into $\mathrm{Nb} = 100$ bins.

From the results provided in this chapter we can conclude that the choice of the initial ray set can make a big impact on the performance of the ray tracing procedure. Based on the idea of taking a smart choice of the initial ray set, we develop a new ray tracing method which is based on phase space. The phase space (PS) concept will be introduced in the next chapter. The new ray tracing method employs the PS of the source and the target of the optical systems. We will show in this thesis that phase space ray tracing allows to trace only few rays inside the system to obtain the desired accuracy of the target intensity.

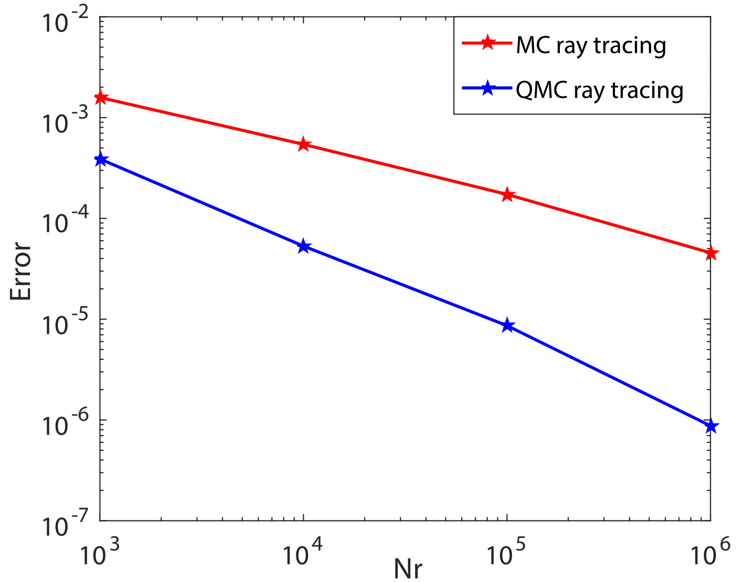

Figure 3.6: Error as function of the number of rays traced in a logarithmic scale for fixed number of bins Nb = 100. MC ray tracing convergence is of the order $O(1/\sqrt{\mathrm{Nr}})$ and it is shown with the red line. QMC ray tracing convergence is of the order $O(1/\mathrm{Nr})$ and it is depicted with the blue line.

32

Chapter 4

Ray tracing on phase space

Ray tracing on phase space is a method which employs the phase space (PS) of the source and the target of the optical system. Moreover, it takes into account the trajectory that every ray follows during its propagation. Before explaining the method, we introduce the PS concept.

4.1 Phase space

The PS of a three-dimensional systems is a four-dimensional space, indeed every ray is described by two position coordinates and two direction coordinates. The two position coordinates are given by two of the coordinates of the intersection point of the ray with the surface, while the two direction coordinates are the momentum coordinates of the vector tangent to the ray projected on the optical surface, [23].

For two-dimensional systems every ray in PS is given by a point in a two-dimensional space. Given an optical line j, the ray position coordinate on PS is the x-coordinate of the intersection point between the ray and the line j. The direction coordinate is the sine of the angle that the ray forms with respect to the normal $\boldsymbol{\nu}$ of line j which is always directed inside the same medium in which the incident ray travels, multiplied by the index of refraction n. We indicate the PS with $S{=}Q{\times}P$, where Q is the set of the position coordinates q and P is the set of the direction coordinates $p = n \sin\theta$, with $\theta \in [-\pi/2, \pi/2]$ the angle between the ray segment inside the system and the normal measured counterclockwise. In the following, the phase space is considered only for the source S and the target T and for no other line of the optical system. The coordinates of every ray on S and T are indicated with (q_1, p_1) and (q, p), respectively.

As an example, in Figures 5.5 and 5.7 we show the source and target PS of the two-faceted cup (in Figure 3.1), respectively, sampled with 10^4 randomly traced rays. The coordinates of every point in Figure 5.5 correspond to the position and direction coordinates of a ray at the source, while the coordinates of every point in Figure 5.7 correspond to the position and direction coordinates of a ray at the target, which are calculated using the ray tracing procedure. Furthermore, we store the path that every ray follows, where we refer to a path as the sequence of the lines encountered by the ray. In Figures 5.5 and 5.7 a color is associated to every path, hence all the rays that follow the same path are depicted with the same color. We note that the

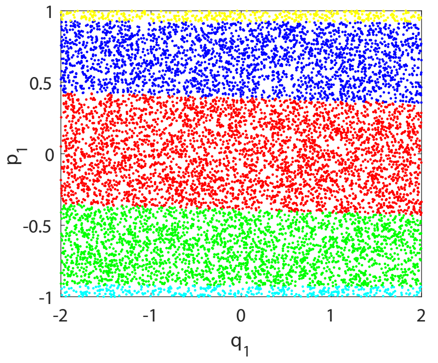

Figure 4.1: Source PS of the two-faceted cup. Five different paths can occur.

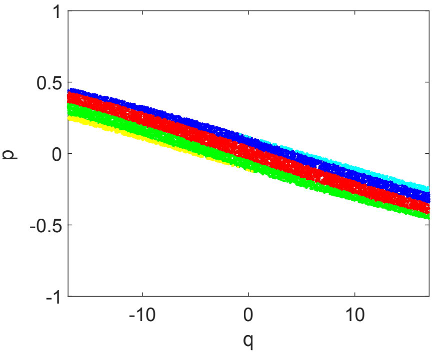

Figure 4.2: Target PS of the two-faceted cup. Five different paths can occur

source and target phase spaces are partitioned into different regions according to the path Π followed by the rays. Given a path Π, the corresponding regions are indicated with $R_1(\Pi)$ and $R(\Pi)$ at the source and the target PS, respectively. Rays that propagate through the two-faceted cup can follow 5 different paths. Some rays are emitted from the source and arrive at the target without hitting any other line, they follow path $\Pi_1 = (1, 4)$. These rays are depicted in red in the PS pictures. Some other rays can hit the left or the right reflector (line 2 and 3, respectively) once, their corresponding paths are $\Pi_2 = (1, 2, 4)$ and $\Pi_3 = (1, 3, 4)$, respectively. These rays are the blue and green dots in PS. Finally, there is the possibility that the rays have two reflections before hitting the target. They follow either path $\Pi_4 = (1, 2, 3, 4)$ or path $\Pi_5 = (1, 3, 2, 4)$ and they are depicted with the yellow and cyan points.

For the two-faceted cup all light emitted by the source arrives at the target. In order to derive the photometric variables at the target we need to understand where light ends up, i.e. which parts of the target PS are illuminated by the source. Indeed, while the source PS is completely covered by rays, some parts of the target PS are not reached by any ray at all, that is

$$\begin{aligned} S &= \bigcup_{\Pi} R_1(\Pi), \\ T &\supset \bigcup_{\Pi} R(\Pi), \end{aligned} \tag{4.1.1}$$

where the union is over all the possible paths. This means that, while the luminance at the source PS is positive for any possible position and direction, the luminance at the target PS is positive only inside the regions $R(\Pi)$, for every path Π, and it is equal to 0 outside those regions. For this reason, from now on we will refer to $R(\Pi)$ as the regions with positive luminance.

It is very important to remark that, although S and T have a different ray distribution, the area covered by the rays is conserved. This follows from étendue conservation. From (2.1.19), using $\mathrm{d}p = n\cos(\theta)\mathrm{d}\theta$, we rewrite the two-dimensional étendue in source PS as:

$$U = \int_Q \int_P \mathrm{d}q\,\mathrm{d}p. \tag{4.1.2}$$

Therefore, in two dimensions, étendue can be seen as an area in PS. Etendue conservation leads to the conservation of the areas of regions with positive luminance.

For the two-faceted cup in Figure 3.1 we have that the étendue at the source is $U = 8$ (see Figure 5.5). Computing the total area covered by the regions with positive luminance at the target using the tétendue trapezoidal rule, we proved that it is equal to $U = 8$. From this follows a fundamental principle in non-imaging optics which is referred to as "the edge-ray principle". A literature overview of this principle is given in the next paragraph.

4.2 The edge-ray principle

The goal in non-imaging optics is to transfer all light from the source aperture to the output aperture. Systems that satisfy this property are referred to *ideal optical systems*. Several methods to design ideal optical systems are based on the edge-ray principle, [24, 25]. Basically it states that all the light rays exiting the edges of the source will end at the edges of the target. This guarantees that all light emitted from the source will arrive at the receiver, see Figure 4.3.

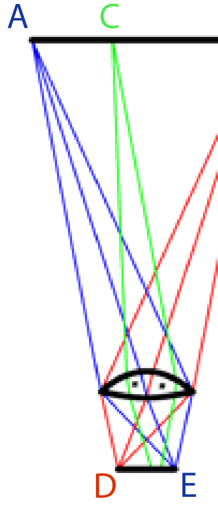

Figure 4.3: A lens that receives light from a source AB and redirects it to the receiver DE. Rays that leave the edges of the source hit the edges of the target (blue and red rays). Rays coming from the interior of the source will end at the interior of the target (green rays), [26].

In 1985 Miñano proved the principle by using the PS of the source and the target of an optical system, [27, 28]. He proved the principle for systems in inhomogeneous media, where the index of refraction is a continuous function, so the map that connects the source and target phase spaces is a continuous map. Indicating with $\mathrm{M}(P)$ the optical map of a point P, Miñano showed that if $\mathrm{M}(\partial S) = \mathrm{M}(\partial T)$ then $\mathrm{M}(S) = \mathrm{M}(T)$ and vice versa. Note that the trajectory of two rays in PS cannot cross. The first version of the edge-ray principle [28] can be enunciated in two-dimensions as follows:

Lemma 4.2.1. *Edge-ray principle (version1)*
Suppose that:

a) There are two regions R_1 *and* R *in PS with the same area such that*

$$\mathrm{M}(\partial \mathrm{R}_1) = \mathrm{M}(\partial \mathrm{R});$$

b) The refractive-index distribution n *is a continuous function;*

Then, the following relation holds:

$$\mathrm{M}(\mathrm{R}_1) = \mathrm{M}(\mathrm{R}).$$

The second assumption in the previous lemma implies that the optical map is continuous in PS. However, for some optical systems, as for instance the compound parabolic concentrator (CPC), the ray mapping in phase space is not continuous. This is due to multiple reflections that rays can encounter with the reflectors. This implies that some rays at the edge of the source could not be mapped into rays at the edges of the target [29].

In 1994 Ries and Rabl reformulated the edge-ray principle such that it is valid for all systems even if the ray map in PS is not continuous [30]. Suppose that $R_1(\Pi)$ and $R(\Pi)$ are the regions, corresponding to path Π, at the source and the target PS, respectively. They showed that, for a given path Π, if the boundaries $\partial R_1(\Pi)$ are mapped into the boundaries $\partial R(\Pi)$, then also the regions $R_1(\Pi)$ are mapped into the regions $R(\Pi)$. Then, to map S to T it is necessary and sufficient that the first version of the edge ray principle is observed for all part of S and T defined by the number of reflections [30].

Lemma 4.2.2. *Edge-ray principle (generalized version)*
Let indicate every possible path with $(\Pi_j)_{j=1,\cdots,Np}$*, where* Np *is the number of all possible paths. Every possible path correspond to a certain number of reflections. Let denote with* $\mathrm{R}_1(\Pi_j)$ *and* $\mathrm{R}(\Pi_j)$ *the regions at* S *and associated to path* Π_i *such that they are a partition of* S *and* T*, that is:*

$$\mathrm{S} = \bigcup_{j=1}^{Np} \mathrm{R}_1(\Pi_i), \;\; \textit{with } \mathrm{R}_1(\Pi_j) \cap \mathrm{R}_1(\Pi_i) = \emptyset \textit{ for } i \neq j$$

$$\mathrm{T} = \bigcup_{j=1}^{Np} \mathrm{R}(\Pi_i), \;\; \textit{with } \mathrm{R}(\Pi_j) \cap \mathrm{R}(\Pi_i) = \emptyset \textit{ for } j \neq i.$$

Then, to map a source region into a target, it is necessary and sufficient that the first version of the edge ray principle is observed for all parts of S *and* T *defined by the number of reflections:*

$$\mathrm{M}\big(\partial \mathrm{R}_1(\Pi_j)\big) = \partial \mathrm{R}(\Pi_j), \quad \forall j \in \{1, \cdots, Np\}.$$

Hence, the edge-ray principle constitutes a tool for designing ideal systems and, to this purpose, it is sufficient that the rays of $\partial R_1(\Pi)$ are transformed to the rays of $\partial R(\Pi)$ for every path Π [31].

Using the PS concept and the edge-ray principle we develop a new ray tracing method. A non-uniform distribution of the rays is provided by developing a triangulation refinement at the source PS which is explained in the next section. The triangulation refinement provides more rays close to the boundaries of the regions $R_1(\Pi)$ each of them is formed by the rays that follow the same path Π. Next, the boundaries $\partial R_1(\Pi)$ are approximated by using two different approaches explained in Chapter 5. For every path Π, the boundaries at the target $\partial R(\Pi)$ are obtained by mapping their corresponding boundaries ∂R_1 at the source.

4.3 Phase space ray tracing

PS ray tracing takes advantage of the fact that there exists an optical map $\mathrm{M} : S \mapsto T$ such that

$$\mathrm{M}(q_1, p_1) = (q, p), \tag{4.3.1}$$

for every $(q_1, p_1) \in S$. For very simple systems, like the two-faceted cup, it is possible to determine an analytic expression for M (as explained in Appendix B). This is not the case for most of the optical systems we deal with. In these cases it is necessary to implement ray tracing to calculate how light is distributed at the target. As mentioned in the previous paragraph, for some optical systems M is not even continuous. Nevertheless, given a path Π, the restriction of M to R_1 $\mathrm{M}(\Pi)$: $R_1(\Pi) \mapsto R(\Pi)$ which maps the region $R_1(\Pi)$ in S into the region $R(\Pi)$ in T is a continuous and bijective map. The edge ray principle guarantees that $\mathrm{M}(\Pi)$ maps $R_1(\Pi)$ onto $R(\Pi)$ preserving topological features. In particular, the boundary $\partial R_1(\Pi)$ is mapped onto the boundary $\partial R(\Pi)$. Employing the maps $\mathrm{M}(\Pi)$ for all the possible paths Π, the output light distribution is determined. Therefore, the photometric variables at the target can be calculated.

The luminance $L(q, p)$ at the target PS is given by:

$$\begin{aligned} &L(q,p) > 0 \text{ for } (q,p) \in R(\Pi) \text{ for some path } \Pi, \\ &L(q,p) = 0 \text{ otherwise.} \end{aligned} \tag{4.3.2}$$

Since the luminance is conserved along a ray and a Lambertian source is considered, it is constant inside the regions $R(\Pi)$. The target intensity along a given direction $p = \text{const}$ is computed through an integration of the target luminance $L(q, p)$ and it is defined in T by:

$$I_{\mathrm{PS}}(p) = \int_Q L(q,p)\mathrm{d}q. \tag{4.3.3}$$

Note that, while in the real space the intensity is defined as a function of the angular coordinate θ (see Chapter 2), in PS the intensity is defined as a function of the direction coordinate $p = n\sin(\theta)$. The previous equation implies that, assuming a Lambertian source, the problem of computing the target intensity is reduced to the problem of calculating the boundaries $\partial R(\Pi)$ for all possible paths Π. Hence, the intensity along the direction $p = const.$ is given by the sum of the lengths intervals formed by the support of the luminance and line $p = const.$. For example, if two intersection points between line $p = const.$ and the boundary $\partial R(\Pi)$ are found, indicating their position coordinates with $q^{\min}(\Pi, p)$ and $q^{\max}(\Pi, p)$, where $q^{\min}(\Pi, p) < q^{\max}(\Pi, p)$, and using Eq. (4.3.2), we obtain that Eq. (4.3.3) reduces to:

$$I_{\mathrm{PS}}(p) = \sum_{\Pi} \int_{q^{\min}(\Pi,p)}^{q^{\max}(\Pi,p)} L(q,p)\mathrm{d}q = \sum_{\Pi} \left(q^{\max}(\Pi,p) - q^{\min}(\Pi,p)\right), \tag{4.3.4}$$

where the sum is over all the possible paths and the second equation holds as we assume $L = 1$ in $R(\Pi)$. In case more then two intersection points occur, a generalized equation needs to be used for calculating the intensity. Note that for every single ray only one path is possible as we are assuming that all the lines are reflective lines. Because of this, the regions $R(\Pi)$ do not overlap, i.e.

$$\bigcap_{\Pi} R(\Pi) = \emptyset, \tag{4.3.5}$$

where the intersection is over all possible paths.

From Eq. (4.3.4) we note that, using the PS structure, we could trace less rays inside the system to obtain the target intensity profile. The aim is to construct a ray tracing procedure that allows us tracing less rays overall and more rays close to the discontinuity of the luminance, i.e. close to the boundaries $\partial R(\Pi)$. To this purpose, we start from a triangulation made by only two triangle, then a triangulation refinement at S is defined as explained in the following.

The regions $R(\Pi)$ can be determined only when some rays are traced. The procedure starts with coordinates $(q_1^k, p_1^k)_{k=1,\cdots,4}$ of the four corner points of S. For each of them, the corresponding path $(\Pi^k)_{k=1,\cdots,4}$ is calculated. Next, the grid is divided into two equal triangles joining two opposite vertices (in our simulation we always trace the diagonal north-west to define the new triangles). For each triangle the rays located at its corners are traced. If not all the paths corresponding to those rays are the same, one or more boundaries $\partial R(\Pi)$ are expected to cross the triangle. In that case, the middle points $(q_1^k, p_1^k)_{k=5,6,7}$ of each side of the triangle are added and the three corresponding rays are traced (unless they were already traced in the previous steps). Each refinement step leads to four new triangles (see Figure 4.4).

When all the rays corresponding to the corners of each triangle have the same path, it is not necessary to refine the triangles anymore. The triangles very close to the boundaries have always two vertices whose corresponding rays follow the same path and one vertex whose corresponding ray follows another path. Since they are crossed by a boundaries, two different paths are found for the rays at the vertices of those triangles. Because of this, the procedure could continue infinitely, therefore, two parameters $\varepsilon_q^{\min}$ and $\varepsilon_p^{\min}$ are introduced to defined a stopping criterion. The algorithm stops when the length of the sides of the triangles is smaller than $\varepsilon_q^{\min}$ and $\varepsilon_p^{\min}$ in q and p direction. We indicate all the possible paths with $(\Pi_j)_{j=1,\cdots,\mathrm{Np}}$ where Np is the maximum number of paths[1] (Np= 5 for the two-faceted cup). If the size of the triangles is too big, it can happen that a region formed by rays that follow a path

[1] We indicate with $\Pi^k = \Pi(q_1^k, p_1^k)$ the path followed by rays with coordinates (q_1^k, p_1^k) in Source PS, can happen $\Pi^k = \Pi^h$ for $k \neq h$. With $(\Pi_j)_{j=1,\cdots,\mathrm{Np}}$ we indicate all the possible Np paths that can occur, therefore $\Pi_i \neq \Pi_j$ if $i \neq j$.

Π_j is located completely inside a triangle whose vertices are related to another path Π_i with $j \neq i$, see Figure 4.5. To avoid this, two parameters $\varepsilon_q^{\max}$ and $\varepsilon_p^{\max}$ are defined for the q_1-axis and the p_1-axis, respectively. When the length of the sides of the triangle are greater than these parameters, a new triangle is defined even if its vertices correspond to the same path. The values of the parameters $\varepsilon_q^{\min}$, $\varepsilon_p^{\min}$, $\varepsilon_q^{\max}$ and $\varepsilon_p^{\max}$ determine the number of rays traced. Thus, on the one hand, decreasing $\varepsilon_q^{\min}$ and $\varepsilon_p^{\min}$ more rays close to the boundaries are traced; on the other hand, decreasing the values of $\varepsilon_q^{\max}$ and $\varepsilon_p^{\max}$ more rays in the interior of the regions are traced.

The triangulation refinement is provided by Algorithm 1 which uses the two recursive functions Left Triangle and Right Triangle. The function Left Triangle is defined in Algorithm 2 (see Figure 4.6). A similar procedure gives the function Right Triangle (see Figure 4.7).

Algorithm 1 Triangulation refinement algorithm

Initialize $\varepsilon_q^{\min}, \varepsilon_q^{\max}, \varepsilon_p^{\min}$, and $\varepsilon_p^{\max}$, Ray = [empty];
▷ $\varepsilon_q^{\min}, \varepsilon_q^{\max}, \varepsilon_p^{\min}$, and $\varepsilon_p^{\max}$ are fixed parameters needed to stop the procedure
▷ Ray: structure that contains all the information about the rays traced[2].

$(q_1^1, p_1^1) \leftarrow$ left bottom corner of source PS: (-a, -1)
$(q_1^2, p_1^2) \leftarrow$ right bottom corner of source PS: (a, -1)
$(q_1^3, p_1^3) \leftarrow$ right upper corner of source PS: (a, 1)
$(q_1^4, p_1^4) \leftarrow$ left upper corner of source PS: (-a, 1)
for $k = 1 \rightarrow 4$ **do**
    Trace the ray with initial coordinates (q_1^k, p_1^k) in S;
    Calculate the corresponding path Π^k;
  ▷ Store the information found in the structure Ray;
    Ray.$q \leftarrow$ [Ray.q, q_1^k];
    Ray.$p \leftarrow$ [Ray.p, p_1^k];
    Ray.$\Pi \leftarrow$ [Ray.Π, Π^k];
end for
VL $\leftarrow [1, 2, 4]$ ▷ VL vertices of the left triangle
VR $\leftarrow [2, 3, 4]$ ▷ VR vertices of the right triangle
Left Triangle(VL, Ray, $\varepsilon_{q_1}^{\min}, \varepsilon_{q_1}^{\max}, \varepsilon_{p_1}^{\min}, \varepsilon_{p_1}^{\max}$) ▷ Refine the left triangle
Right Triangle(VR, Ray, $\varepsilon_{q_1}^{\min}, \varepsilon_{q_1}^{\max}, \varepsilon_{p_1}^{\min}, \varepsilon_{p_1}^{\max}$) ▷ Refine the right triangle
return Ray;

Figure 4.8 shows an example of a triangulation refinement at the source PS of the two-faceted cup in Figure 3.1. For this optical system, the width of the q_1-axis in source phase space is two times the width of the p_1-axis. Thus, our choice is $\varepsilon_p^{\min} = \frac{1}{2}\varepsilon_q^{\min}$ and $\varepsilon_p^{\max} = \frac{1}{2}\varepsilon_q^{\max}$ with $\varepsilon_q^{\min} = 0.1$ and $\varepsilon_q^{\max} = 1$. Using the triangulation refinement, all the possible paths $(\Pi_j)_{j=1,\cdots,\mathrm{N_p}}$ are found and their corresponding regions $R_1(\Pi_j)_{j=1,\cdots,\mathrm{N_p}}$ are determined. Using the edge-ray principle, we conclude that also the regions $R(\Pi_j)_{j=1,\cdots,\mathrm{N_p}}$ at the target are determined and only the rays close to the boundaries ∂R_1 need to be considered to obtain the target ray distribution.

4.4 Conclusions

In this chapter we introduced the phase space concept. We explained a new ray tracing method based on the source and the target PS representation. In PS every point corresponds to a unique ray. The coordinates of every point correspond to the initial ray position q_1 and the initial ray direction $p_1 = \sin(\theta_1)$ (expressed with respect to the normal of the source). The method also takes into account the paths followed by every ray traced. Considering only reflection, every single ray follows only one path and, therefore, the PS regions do not overlap.

As an example, we provided the source and the target PS representation of the two-faceted cup. The edge-ray principle guarantees that all the rays that follow the same path are located in the same regions in PS. If we know these regions at the source we can determine the corresponding regions at the target. It is sufficient to map the boundaries at the source $\partial R_1(\Pi)$ to obtain their corresponding target boundaries $\partial R(\Pi)$.

The boundaries $\partial R(\Pi)$ are particularly relevant because there the luminance jumps from 0 to a positive value. Assuming a Lambertian source, only the rays at the boundaries are needed to compute the target intensity. Based on this idea, a triangulation in S is constructed such that the rays closest to $\partial R_1(\Pi)$ are selected and more rays in their vicinity are created to get progressively better estimates of the boundaries.

In Figures 4.9 we show three different ray distributions on the source PS of the two-faceted cup. In Figure 4.9a, 10^3 random points are shown. MC ray tracing is based on this random distribution of the initial rays set. In Figure 4.9b, 10^3 points of a two-dimensional Sobol sequence are shown. Since Sobol sequences are defined in a unit square, we scaled it such that all the source PS $S= [-2, 2] \times [-1, 1]$ is covered by rays. QMC ray tracing considers as initial set, rays distributed as the points of a Sobol sequence. Such regular distribution can lead to several advantages for the computation of the target intensity, see Section 3.3. Finally, Figure 4.9c shows a non-uniform distribution of rays at the source PS. Such distribution is obtained from the triangulation refinement explained in the previous section. The procedure requires tracing more rays close to the boundaries $\partial R_1(\Pi)$ and only few rays in their interior.of the regions in source PS. From the edge ray-principle, we obtain that these rays will be located close to the boundaries $\partial R(\Pi)$ of the regions at the target PS. PS ray tracing is based on this kind of initial ray distribution at the source.

The target PS intensity is calculated using only the rays that are located at the boundaries $\partial R(\Pi)$. Thus, in order to obtain the intensity profile at the target, the boundaries $\partial R(\Pi)$ need to be determined.

In the next chapter we provide two different approaches to find the boundaries $\partial R(\Pi)$ using a set of rays given by the triangulation refinement.

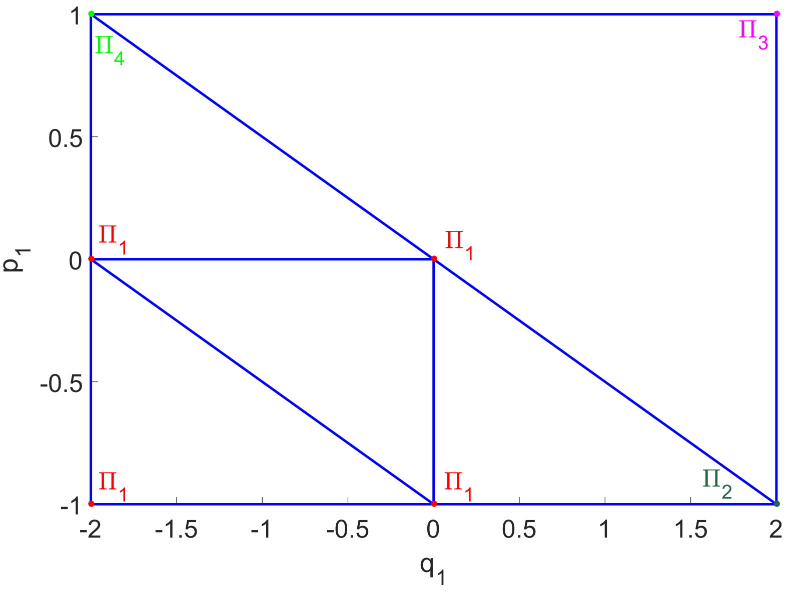

Figure 4.4: Triangulation refinement: when the rays related to the vertices of the triangles follow a different path a new refinement step is required. Each refinement step leads to four new triangles.

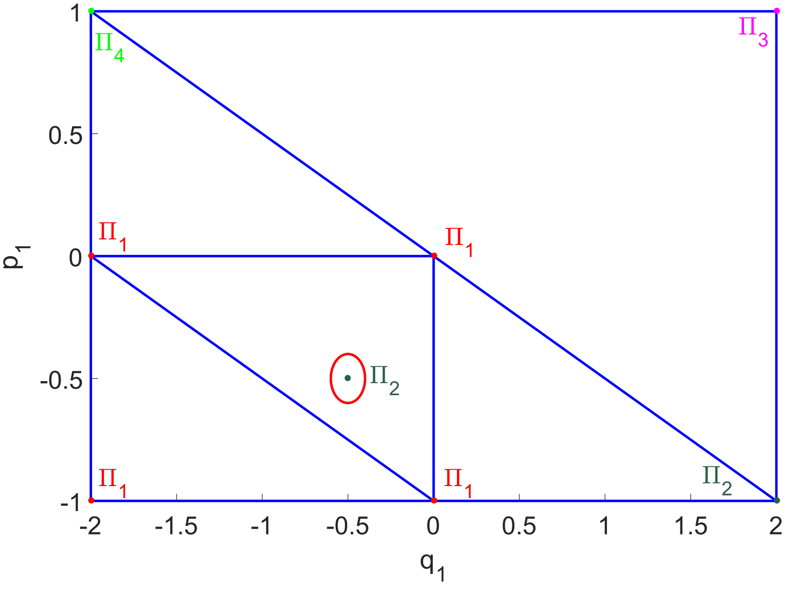

Figure 4.5: The red line encloses a region of rays that follow the path Π_2 and is completely located inside a triangle. The algorithm is not able to detect that region and, a further refinement is required.

Algorithm 2 Algorithm for the refinement of the left triangles

procedure LEFT TRIANGLE(VL, Ray, $\varepsilon_q^{\min}, \varepsilon_q^{\max}, \varepsilon_p^{\min}, \varepsilon_p^{\max}$)
  VL $\leftarrow [1, 2, 4]$
  $q_1^1 \leftarrow$ Ray.q(VL(1)), $p_1^1 \leftarrow$ *Ray*.p(VL(1))
  $q_1^2 \leftarrow$ Ray.q(VL(2)), $p_1^2 \leftarrow$ *Ray*.p(VL(2))
  $q_1^3 \leftarrow$ Ray.q(VL(3)), $p_1^3 \leftarrow$ *Ray*.p(VL(4))
  $\text{dist}_q \leftarrow |q_1^2 - q_1^1|$
  $\text{dist}_p \leftarrow |p_1^3 - p_1^1|$
  RefineTriangle $\leftarrow$ false;
  DifferentPath $\leftarrow$ false;
  if $\text{dist}_q > \varepsilon_q^{\max}$ or $\text{dist}_p > \varepsilon_p^{\max}$ **then**
    RefineTriangle $\leftarrow$ true;
  end if
  for $k = 1 \to 2$ **do**
    if $\Pi^k \neq \Pi^{k+1}$ **then**
      DifferentPath $\leftarrow$ true;
    end if
  end for
  if $\text{dist}_q > \varepsilon_q^{\min}$ or $\text{dist}_p > \varepsilon_p^{\min}$ **then**
    RefineTriangle $\leftarrow$ DifferentPath;
  else
    if (DifferentPath is true) **then**
      Ray(VL).boundary $\leftarrow$ true; ▷ A boundary crosses the triangle
    end if
  end if
  if (RefineTriangle is true) **then**
    Define the points at the middle of each side of the triangle
    $(q_1^5, p_1^5) = ((q_1^1 + q_1^2)/2, p_1^1)$
    $(q_1^6, p_1^6) = (q_1^5, (p_1^1 + p_1^2)/2)$
    $(q_1^7, p_1^7) = (q_1^1, p_1^6)$
    for $k = 5 \to 7$ **do**
      if The ray with coordinates (q_1^k, p_1^k) is not traced yet **then**
        Trace the ray with initial coordinates: (q_1^k, p_1^k) in PS;
        Compute the corresponding path Π^k;
        Store the ray's coordinates Ray.$q \leftarrow$ [Ray.q, q_1^k];
        Store the ray path Ray.$\Pi \leftarrow$ [Ray.Π, Π^k];
      end if
    end for
    return LEFT TRIANGLE([VL(1), 5, 7], Ray, $\varepsilon_q^{\min}, \varepsilon_q^{\max}, \varepsilon_p^{\min}, \varepsilon_p^{\max}$);
    return LEFT TRIANGLE([5, VL(2), 6], Ray, $\varepsilon_q^{\min}, \varepsilon_q^{\max}, \varepsilon_p^{\min}, \varepsilon_p^{\max}$);
    return LEFT TRIANGLE([7, 6, VL(3)], Ray, $\varepsilon_q^{\min}, \varepsilon_q^{\max}, \varepsilon_p^{\min}, \varepsilon_p^{\max}$);
    return RIGHT TRIANGLE([5, 6, 7], Ray, $\varepsilon_q^{\min}, \varepsilon_q^{\max}, \varepsilon_p^{\min}, \varepsilon_p^{\max}$);
  end if
return Ray;
end procedure

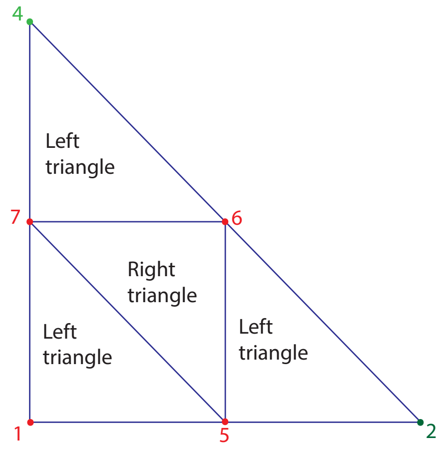

Figure 4.6: Left triangulation refinement algorithm (recursive function LEFT TRIANGLE).

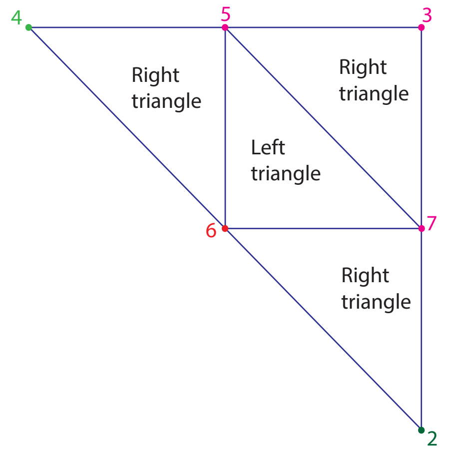

Figure 4.7: Right triangulation refinement algorithm (recursive function RIGHT TRIANGLE).

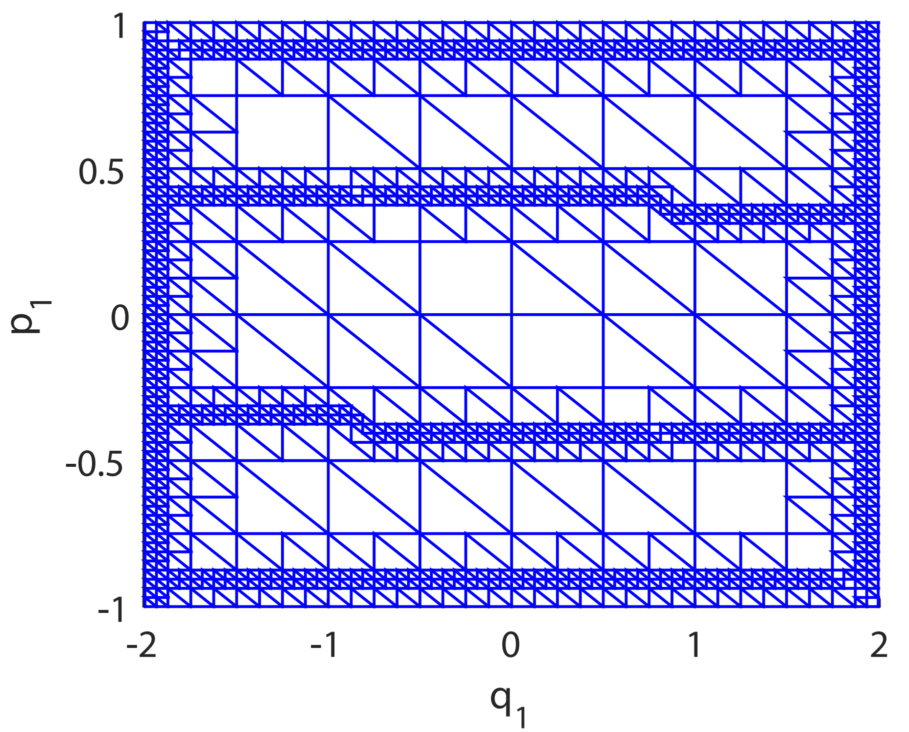

Figure 4.8: Triangulation refinement of source phase space: near the boundaries more rays are traced. The values of the parameters are $\varepsilon_{q_1^{\min}} = 0.1$ and $\varepsilon_{q_1^{\max}} = 1$.

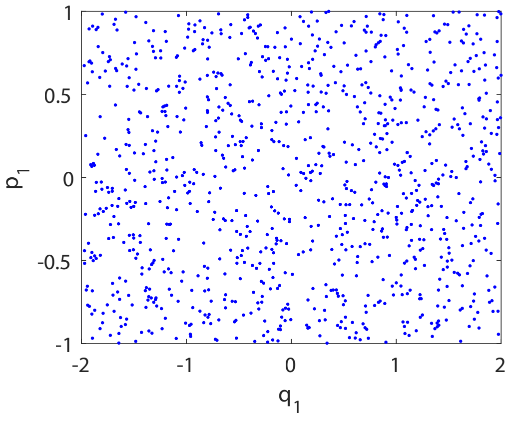

(a) 10^3 random rays at the source PS (MC ray tracing).

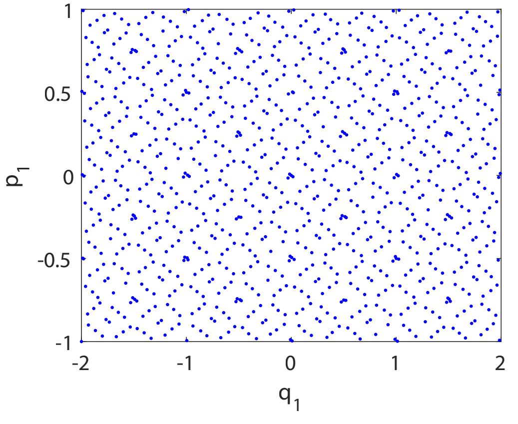

(b) 10^3 rays at the source PS distributed as the point of a Sobol sequence (QMC ray tracing).

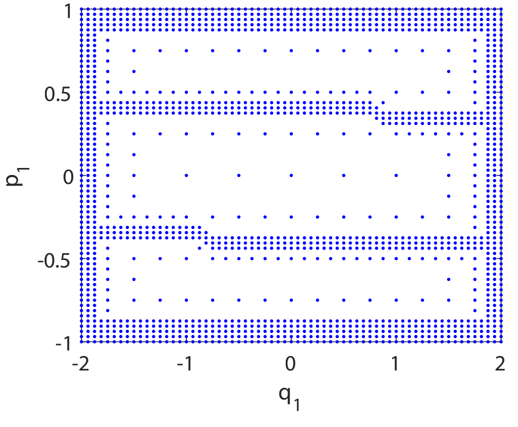

(c) $1.5 \cdot 10^3$ rays distributed using the triangulation refinement (PS ray tracing).

Figure 4.9: Three different ray distributions at the source of the two-faceted cup.

Chapter 5

The α-shapes approach

In the previous chapter we presented a new ray tracing approach based on PS. We explained that, in order to compute the target intensity, it is necessary to know the boundaries of the regions in target PS with positive luminance. Ray tracing in PS requires tracing only the rays close to these boundaries. The rays traced can be seen as a point cloud in PS. To detect the shape formed by those rays, the α-shapes approach is employed [32].

Methods based on α-shapes are widely used to reconstruct an unknown shape formed by a set of finite data points [33]. α-shapes are a very powerful tool to construct the shape of a point cloud. As α varies, we can obtain different α-shapes from the point set itself to the convex hull [34]. The disadvantage of such methods is that it can be very hard to choose the appropriate value of the parameter α and, in most cases it can be selected only by numerical simulations.

We develop a technique based on α-shape that gives a criterion to determine the value of the parameter α, for which the boundaries are approximated well [35].

This chapter is organized as follows. An overview of the-state-of-the-art about α-shape methods is provided in Section 5.1; the technique used for computing the α value is explained in Section 5.2; the results for two different kind of total internal reflection (TIR)-collimators are given in Section 5.3. Discussions are conclusions are provided in the last paragraph of this chapter.

5.1 α-shapes theory

Given a finite set $V = \{v_1, \cdots, v_N\} \subset \mathbb{R}^2$ of points, α-shapes are geometrical objects that give us an approximation of the shape formed by the point cloud. For now we do not further specify the notion of shape. A more precise definition will be provided later.

Before giving a formal definition, we explain an intuitive and nice interpretation of α-shapes [36]. Let us think of a stracciatella ice-cream[1]. If we desire to know the shape formed by the chocolate pieces we can start eating the ice cream using a spoon with a spherical scoop and try not to remove any piece of chocolate. We will

[1]Stracciatella ice cream is made with milk-based ice-cream and fine pieces of chocolate, [37].

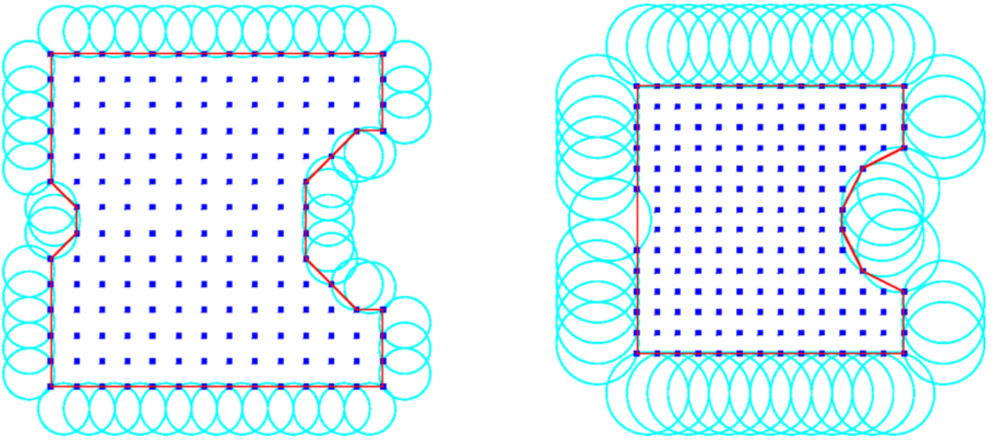

Figure 5.1: **Construction of α-shapes.** The boundary of the shape (red line) formed by a set of points (blue dots) in $\mathbb{R}^2$ is detected for $\alpha = 1$ (left) and for $\alpha = 2$ (right) [38].

obtain a shape formed by arcs and points (see Figure 5.1 for the two-dimensional case). Straightening the arcs to line segments we obtain broken lines which constitute the boundary of the so-called α-shape of the point set V. A very small spoon will allow us to eat the entire ice cream without eating any piece of chocolate, while with a larger spoon we are not able to eat any chunk of the ice cream without chocolate pieces. In this example, the chocolates peaces are the points of V and, the parameter α determines the radius of the carving spoon (the spherical spoon in two-dimension is simply a circle).

The formal definition of α-shape was first given by Edelsbrunner, Kirkpatrick and Seidel in 1983, [39]. They describe α-shape as a generalization of the convex hull of a finite set of points in the plane. Let α be a non negative number $0 \leq \alpha < \infty$. If $\alpha = 0$ the shape degenerates to the point set V. On the other hand, when $\alpha \to \infty$ the α-shape is simply the convex hull of V. If $0 < \alpha < \infty$ the α-shape is a polytope of V [40]. The construction of the α-shape is closely related to the Delaunay triangulation of V [41]. Therefore, a formal definition of triangulation and Delanauy triangulation is now required.

Given a set V of not all aligned points, let us consider the set E of all the straight-line segments whose endpoints are in V. A triangulation T of V is the subset of E with the maximum number of segments such that all the line segments of T intersect only at their endpoints [42]. A more formal definition of triangulation is provided in the following

Let $\Omega \subset \mathbb{R}^2$ be the convex hull of V and $T_h = \{K_1, \cdots, K_h\}$ be a partition of Ω into closed triangles, that is triangles that included their boundary. Suppose that the following properties are verified:

(a) $\Omega = \bigcup_{i=1}^{h} K_i$;

b) For $K_i, K_j \in T_h$, $K_i \neq K_j$, and

$$\mathrm{int}(K_i) \cap \mathrm{int}(K_j) = \emptyset,$$

where $\mathrm{int}(K) = K - \partial K$.

Then T_h is called a *triangulation* of Ω [43].

The Delaunay triangulation T' of the points set V has the property that the circle circumcircle of any triangle of T does not contain any point of V. This is called the Delaunay property. A very commonly used algorithm to construct such triangulation is explained in the following. T' is constructed by modifying a general triangulation T such that every point satisfies the Delaunay property. Therefore, every triangle (or tetrahedron in three dimensions) that does not satisfy such property is flipped such that the new edge is part of the triangulation (see Figure 5.2). Given, for example, an arbitrary triangulation T in two-dimensions, for each edge $\overline{\mathrm{ab}}$ in T which is not on the boundary of the convex hull the two triangles Δ_{abc} and Δ_{abd} with the common edge $\overline{\mathrm{ab}}$ are found. Then, if either the circumcircle of triangle Δ_{abc} contains point d or the circumcircle of triangle Δ_{abd} contains point c the edge $\overline{ab}$ cannot be included in the Delaunay triangulation and, therefore, it is flipped such that the other two possible triangles Δ_{acd} and Δ_{bcd} are found. The new edge $\overline{\mathrm{cd}}$ locally satisfies the Delaunay property and the triangles Δ_{acd} and Δ_{bcd} are added to the Delaunay triangulation T', see Figure 5.2.

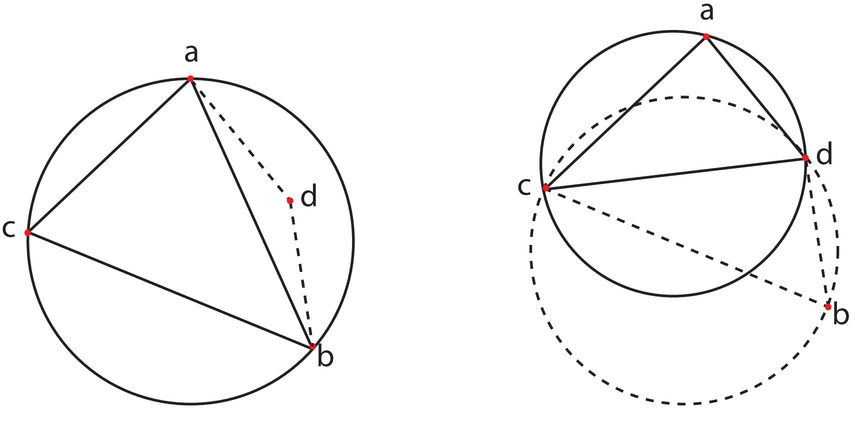

(a) The point d is inside the circle circumscribing the triangle Δ_{abc}, therefore the edge $\overline{\mathrm{ab}}$ cannot be included in the Delaunay triangulation.

(b) The flipped triangle Δ_{acd} satisfies the Delaunay property, thus it is included in the Delaunay triangulation.

Figure 5.2: Construction of the Delaunay triangulation in 2D.

Several other algorithms have been developed to construct a Delaunay triangulation, see for example [44, 45]. Given a point set V and a triangulation T, it can be proved that the corresponding Delaunay triangulation T' is unique. Moreover, it has the property to have the largest minimum angle among all possible triangulations of a point set V [46].

Alternatively the Delaunay triangulation can be constructed as the dual of the Voronoi diagram [47].

For *almost*[2] every point $x \in \mathbb{R}^2$, there is a point which is the closest point to x. The Voronoi cell of a point $v_i \in V$ contains all points in $\mathbb{R}^2$ which are closer to v_i, see Figure 5.3. The Voronoi diagram of $V \subset \mathbb{R}^2$ is defined as the set of all Voronoi cells, [48]. A more formal definition of the Voronoi diagram is given in the following.

Definition 5.1.1. Let $V = \{v_1, \cdots, v_N\}$ be a set of point in $\mathbb{R}^2$. The Voronoi cell V_i associated to point v_i is defined as:

$$V_i = \{x \in \mathbb{R}^2 \mid |x - v_i| < |x - v_j| \quad \forall j \neq i\}, \tag{5.1.1}$$

The Voronoi diagram U is defined as

$$U = \bigcup_{i=1}^{N} V_i \tag{5.1.2}$$

where $V_i \cap V_j = \emptyset$ for $i \neq j$.

For the definition of Voronoi diagram in higher dimensions see [49].

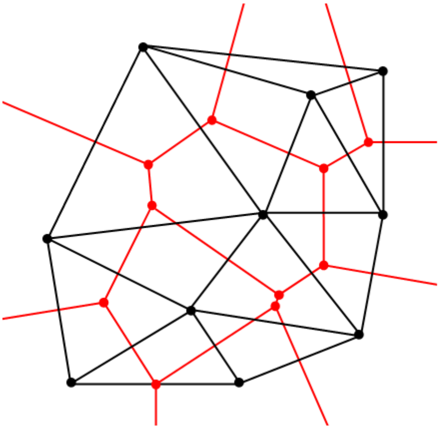

Figure 5.3: Relationship between the Delaunay triangulation (in black) and the Voronoi Diagram (in red), [50]

The Delaunay triangulation triangulates the convex hull of V and, therefore it does not constitute a suitable method for reconstructing the contour formed by a point cloud. Therefore, α-shape methods were developed to solve such problem [51, 33]. Starting from the Delaunay triangulation T' of a point set V, the corresponding α-shape of V is formed by the only triangles of T' that satisfy the so-called "α-test" which is now briefly explained. For each triangle we calculate the circumradius, i.e. the radius of the circumcircle. If the radius is larger than α the triangle is removed from the shape. The choice of the parameter α is highly significant in the α-shapes

[2] It is needed to specify the word *almost* because some points can have the same distance with two or more points of V.

procedure and, it has to be selected such that the desired approximation of the shape formed by the points of V is obtained. Therefore, α is closely related to the radius of the circumcircles. A possible strategy is to find the radius of the greater empty circumcircle. Thus α can be selected according to the density δ of the point sets V with C a constant and δ:

$$\delta = \frac{N}{A} \ , \tag{5.1.3}$$

where N is the number of points in V and A is the area of the convex hull of V. The value of α can be chosen, for instance, inversely proportional to $\sqrt{\delta}$:

$$\alpha = C\frac{1}{\sqrt{\delta}} \ , \tag{5.1.4}$$

Note that, while δ is given for a fixed point set V, the value of C needs to be determined by numerical simulations.

To summarize, the α-shape construction can be outlined as follows:

1. Construct a Delaunay triangulation[3] T' of the point cloud V;
2. For every triangle $T'(i) \in T'$ calculate its circumradius $r(i)$;
3. If $r(i) \leq \alpha$ keep the triangle $T'(i)$ in the triangulation;
4. If $r(i) > \alpha$ remove the triangle from the triangulation;
5. For every triangle return the edges belong to only one triangle of T', the so-called *free boundary* edges[4]. By definition, the free boundary edges are not a common edge of two triangles.

α-shapes provide a nice mathematical definition of the *shape* of a set of points. In two dimensions, α-shapes gives the contour of the point cloud which is approximated by a family of broken curved lines. Although they are a powerful tool for determining the shape of a point cloud, there exist shapes that are not described well by classical α-shapes. Indeed for some surfaces there is no value of α that includes all desired triangles and deletes all undesired triangles. If the parameter α is determined according to the density of the point cloud, it can be difficult to obtain a good approximation of a shape formed by a non-uniform points set. Furthermore, the α-shape method does not work well when the shape we need to approximate has a sharp turn or a joint. To overcome these issues, Teichmann and Capps presented alternatives approaches to establish the value of α, [52]. Their anisotropic density-scaled α-shapes method constitutes an improvement of classical α-shapes.

There are several ways to determine the value of α [53]; in the next section we provide a technique that exploits the conservation of étendue in PS.

5.2 Determination of α using étendue conservation

As mentioned in Section 4.1, in two-dimensions étendue can be seen as an area in PS. Therefore, given an optical system with a line segment source $\mathsf{S} = [-a, a]$, the

[3] In the simulations we present in this chapter the Matlab function *Delaunay* is used.

[4] In the simulations we present in this chapter the Matlab function *freeBoundary* is used.

étendue at the source coincides with the area of source PS S, and it is given by:

$$U = 4n_1\, a \sin(\theta_1^{\max}), \tag{5.2.1}$$

where a is the half length of the source, n_1 the index of refraction of the medium in which the S is located and $\theta_1^{\max}$ is the maximum value of the angle that the rays make with the normal $\boldsymbol{\nu}_1$ of the source.

For some optical systems, all the rays emitted by the source arrive at the target, for some others there are also rays that can end at other detectors which are located outside the system. Indicating with $R_1(\Pi)$ the regions in source PS formed by the rays that reach the target following path Π and with $R(\Pi)$ the corresponding regions at the target, the étendue U_1 at source related to the only rays that arrive to the target is given by:

$$U_1 = \sum_{\Pi} U\big(R_1(\Pi)\big), \tag{5.2.2}$$

where the sum is over all possible paths Π and $U\big(R_1(\Pi)\big)$ is the contribution to the étendue given by the rays inside $R_1(\Pi)$ in source PS, obtained by:

$$U_1\big(R_1(\Pi)\big) = \iint_{R_1(\Pi)} \mathrm{d}q\,\mathrm{d}p. \tag{5.2.3}$$

Similarly the étendue at the target of the rays emitted by the source is:

$$U_{\mathrm{t}} = \sum_{\Pi} U\big(R(\Pi)\big), \tag{5.2.4}$$

with

$$U\big(R(\Pi)\big) = \iint_{R(\Pi)} \mathrm{d}q\,\mathrm{d}p. \tag{5.2.5}$$

In order to determine the value of α in the α-shape procedure that approximates the boundaries $\partial R(\Pi)$ accurately, we use étendue conservation ($U_{\mathrm{t}} = U_1$). The α-shapes method is applied to every region $R(\Pi)$ for a range of values of α; for each value an approximation of the boundaries $\partial R(\Pi)$ is obtained and the intersection points $q^{\max}(\Pi, p)$ and $q^{\min}(\Pi, p)$ between $\partial R(\Pi)$ and the horizontal lines $p = \mathit{const}$, with $p \in [-1, 1]$, are computed for every path Π. Therefore Equation (5.2.5) becomes:

$$U_{\mathrm{t}}\big(R(\Pi)\big) = \int_{-1}^{1} \Big(q^{\max}(\Pi, p) - q^{\min}(\Pi, p)\Big)\mathrm{d}q\,\mathrm{d}p. \tag{5.2.6}$$

In case more than two intersection points between line $p = \mathit{const}$ and $\partial R(\Pi)$ occur, the previous equation needs to be generalized. Suppose that r intersection points $\big(q^i(\Pi, p), p\big)_{i=1,\cdots,r}$ are found. Ordering their q coordinates in ascending order, the target étendue is calculated by:

$$U_{\mathrm{t}}\big(R(\Pi)\big) = \sum_{i=1}^{m} \int_{-1}^{1} (q^{2i}(\Pi, p) - q^{2i-1}(\Pi, p))\mathrm{d}q\,\mathrm{d}p\,, \tag{5.2.7}$$

where m is the integer part of $r/2$. The integrals in Equations (5.2.6) and (5.2.7) are calculated discretizing the interval $[-1, 1]$ into $\mathrm{Nb} = 100$ sub-intervals of equal length, the so-called bins, and using the trapezoidal rule.

Matching the value of the étendue at the source U_1 with the value of the étendue at the target U_t, a unique value α_c of α is determined. Implementing the α-shapes procedure with $\alpha = \alpha_c$, the best approximation of the boundaries $\partial R(\Pi)$ is found and the intensity at the target can be calculated.

If two intersection points between $p = const$ and $\partial R(\Pi)$ are found the target intensity is calculated using Equation (4.3.4). If more than two-intersection points are found we use the generalized equation:

$$I_{\mathrm{PS}}(p) = \sum_{\Pi,i} \int_{q^{2i-1}(\Pi,p)}^{q^{2i}(\Pi,p)} L(q,p)\mathrm{d}q = \sum_{\Pi,i} \left(q^{2i}(\Pi,p) - q^{2i-1}(\Pi,p) \right), \tag{5.2.8}$$

where $q^{2i}(\Pi,p) > q^{2i-1}(\Pi,p)$, the summation over Π is for all the paths Π for which the intersection $p = const$ and $R(\Pi)$ is not empty, and the summation over i is for $i = 1, 2, \cdots, m$. The second equation holds as we assume $L(q,p) = 1$.

To clarify our idea we apply the method to two different optical systems, the results are presented next.

5.3 Results for a TIR-collimator

We apply the α-shapes method to the set of points in target PS obtained by using PS ray tracing. In this chapter the procedure is applied to two different kinds of total internal reflection (TIR)-collimators.

Let us first describe the TIR-collimator depicted in Figure 5.4. It is an optical system symmetric with respect to the z-axis, it consists of a lens (central curve), two broken lines adjacent to the lens, two curved lines on each side and a top formed by a horizontal segment. The lens (line 2) and the broken lines, formed by a collection of three segments (lines $3, 4,$ and 5 and $9, 10$ and 11), are refractive line segments while the curved lines (labeled with 6 and 8) are designed in such a way that light is totally internal reflected (which explains the name TIR). The light source $\mathcal{S}$ (line 1) and the target $\mathcal{T}$ (line 12) are two straight line segments normal to the optical axis. The source $\mathsf{S} = [-2, 2]$ is located at a height $z_1 = 0.3$ from the x-axis. The target $\mathsf{T} = [-9.7, 9.7]$ is parallel to the source and is located at a height $z = 8.2$. Both S and T are located in air ($n_1 = 1$). The volume inside the collimator is filled with a material with index of refraction $n_2 = 1.5$ (e.g. glass). The collimator is surrounded by two vertical lines (lines 13 and 15) and two horizontal lines (12 and 14) that receive the light emitted from the source that do not arrive at the target; among these the one at the top (line 12) is assumed to be the target, and it is located at a small distance from the top (line 7).

Using PS ray tracing explained in Section 4.3 with parameters $\varepsilon_{q_1}^{\max} = 0.1$, $\varepsilon_{p_1}^{\max} = 5 \cdot 10^{-2}$, $\varepsilon_{q_1}^{\min} = 9 \cdot 10^{-3}$ and $\varepsilon_{p_1}^{\min} = 4.5 \cdot 10^{-3}$, around $1.9 \cdot 10^4$ rays are traced. We discard rays with direction parallel to the source, therefore $p_1 \in [-0.99, 0.99]$. The ray distribution at the source PS S is shown in Figure 5.5, where we depicted the rays that follow the same path with the same color. Seven different paths are found. The yellow rays follow path $\Pi_1 = (1, 2, 7, 12)$; the red rays follow path $\Pi_2 = (1, 4, 6, 7, 12)$; the green rays follow path $\Pi_3 = (1, 10, 8, 7, 12)$; the blue rays follow path $\Pi_4 = (1, 3, 7, 12)$ and the magenta rays follow path $\Pi_5 = (1, 11, 7, 12)$. The rays located inside the

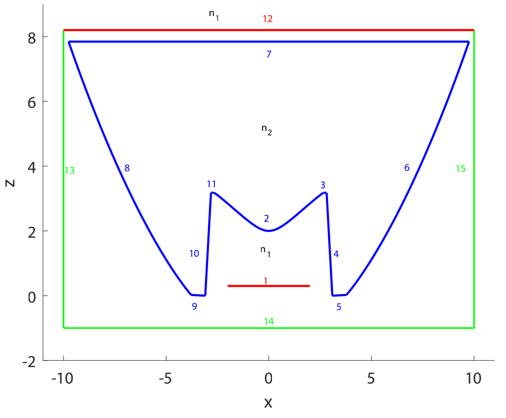

Figure 5.4: **Shape of the TIR-collimator.** Each surface of the system is labeled with a number. The shape of the collimator is shown with a blue line. Three detectors depicted with green lines (surfaces 13, 14, and 15) are located at the left, the right and the bottom of the optical system. The source (line1) and the target (line 12) are depicted in red. The sagitta of the lens is approximately 1.17.

white areas correspond to rays that do not reach the target, they follow either path $\Pi_6 = (1, 4, 7, 6, 13)$ or path $\Pi_7 = (1, 10, 7, 8, 15)$ and they do not give any contribution to the target intensity. Note that, given two adjacent paths the regions $R_1(\Pi)$ in S have usually a common boundary. Since for this system not all the rays emitted by the source arrive at the target, U_t needs to be compared with the étendue U_1 at the source given by only those rays that reach the target (the rays that follow paths $\Pi_6 = (1, 10, 8, 7, 12)$ and $\Pi_7 = (1, 4, 7, 6, 15)$ are discarded). To this purpose U_1 is calculated by removing from the total area U of S those areas occupied by the regions formed by the rays that hit the left or the right detector (white regions in Figure 5.4). For the TIR collimator in Figure 5.4, the total source étendue obtained from Equation (5.2.1) is

$$U = 4 \cdot 1 \cdot 2 \cdot 0.99 = 7.92. \tag{5.3.1}$$

Indicating with A_T the area of each white region in Figure 5.4, U_1 can be approximated by:

$$U_1 = 7.92 - 2A_T \approx 7.77, \tag{5.3.2}$$

where A_T is the approximated area of the triangles shown in Fig. 5.5 with black lines.

U_t is calculated several times from Equation (5.2.6) where every time the boundaries $\partial R(\Pi)$ are obtained by using α-shapes for a different value of α. An accurate approximation of $\partial R(\Pi)$ gives a value of U_t close to the exact étendue. Matching U_1 with all the approximations of U_t we find the best value α_c of α that approximates $\partial R(\Pi)$ and, therefore, U_t.

In Figure 5.6 we represent the approximated value of the source étendue $U_1 \approx 7.77$ with the red line. Different approximations of the target étendue U_t are calculated using Equation (5.2.7) where every time the boundaries $\partial R(\Pi)$ are found using α-shapes

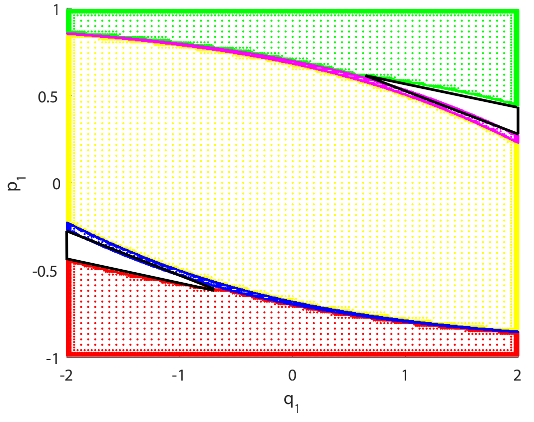

Figure 5.5: **Distribution of the rays on S**. Around $1.67 \cdot 10^4$ rays are traced using the triangulation refinement with parameters: $\varepsilon_q^{\max} = 0.1$, $\varepsilon_p^{\max} = 5 \cdot 10^{-2}$, $\varepsilon_q^{\min} = 9 \cdot 10^{-3}, \varepsilon_p^{\min} = 4.5 \cdot 10^{-3}$. Rays that belong to the same region are depicted with the same color. The rays located inside the white areas do not reach the target. The boundaries of the two white regions are approximated by triangles depicted with black lines.

for a different value of α. In Figure 5.6, we show how the étendue changes by increasing the value of α. This graph shows that using PS ray tracing with $1.67 \cdot 10^4$ rays, the best approximation of the boundaries $\partial R(\Pi)$ is given considering $\alpha = \alpha_c = 0.139$ in the α-shapes procedure. Applying α-shapes with $\alpha = \alpha_c$, a good approximation of $\partial R(\Pi)$ is found. In Figure 5.7 we show the boundaries $\partial R(\Pi)$ in target PS T with $\alpha_c = 0.139$ and tracing $1.67 \cdot 10^4$ rays. Once the boundaries are computed, the target intensity $I_{\mathrm{PS}}(p)$ for every $p \in [-1, 1]$ is obtained from Equation (4.3.4).

To validate our method we compare the PS intensity with the MC intensity. To this purpose a partitioning $P_2 : -1 = p_0 < p_1 < \cdots < p_{\mathrm{Nb}} = 1$ of the interval $[-1, 1]$ into $\mathrm{Nb} = 100$ bins is considered. The averaged and normalized PS intensity $\hat{I}_{\mathrm{PS}}$ is calculated for every $\left(p^{h+1/2} = \frac{1}{2}(p^{h+1} + p^h)\right)_{h=0,\cdots,\mathrm{Nb}-1}$ dividing the PS averaged intensity by the total étendue:

$$\hat{I}_{\mathrm{PS}}(p^{h+1/2}) = \frac{1}{U_{\mathrm{t}}} \int_{p_h}^{p_{h+1}} I_{\mathrm{PS}}(p)\mathrm{d}p. \tag{5.3.3}$$

The averaged and normalized MC intensity $\left(\hat{I}_{\mathrm{MC}}(p^{h+1/2})\right)_{h=0,\cdots,\mathrm{Nb}-1}$ intensity is given by

$$\hat{I}_{\mathrm{MC}}(p^{h+1/2}) = \frac{\mathrm{Nr}[p^h, p^{h+1})}{\mathrm{Nr}[-1, 1)} \qquad \text{for } p \in [p^h, p^{h+1}). \tag{5.3.4}$$

Both approximate intensities $\hat{I}_{\mathrm{A}}(\mathrm{A} = \mathrm{PS}, \mathrm{MC})$ are compared with an intensity $\hat{I}_{\mathrm{ref}}$ taken as a reference. For some optical systems, there is an explicit solution for the target intensity but this is not the case of the TIR-collimator. Therefore, a MC simulation with $1.7 \cdot 10^8$ rays is run to obtain the averaged normalized intensity

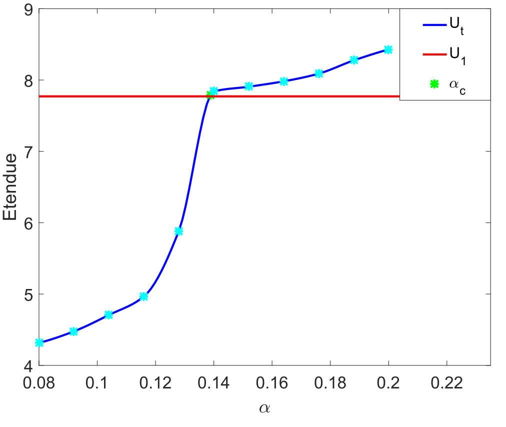

Figure 5.6: **Etendue for the TIR-.collimator** U_{t} is computed for a range of values for α. $U_1 \approx 7.77$ The green dot indicates the value of $\alpha_c = 0.139$ which gives the best approximation of the boundaries $\partial R(\Pi)$ at the target. Around $1.67 \cdot 10^4$ rays have been traced using PS ray tracing.

$\hat{I}_{\mathrm{ref}}$. The intensity profile $\hat{I}_{\mathrm{PS}}$ obtained using PS ray tracing with 66 855 rays and $\alpha = \alpha_c = 0.02$ is depicted in Fig. 5.8 with a red line. $\hat{I}_{\mathrm{PS}}$ is hardly distinguishable from $\hat{I}_{\mathrm{ref}}$ (dashed and blue line in Figure 5.8).

Finally, we calculate the error between $\hat{I}_{\mathrm{A}}$ and $\hat{I}_{\mathrm{ref}}$, defined as:

$$\text{error} = \frac{\sum_{h=1}^{\mathrm{Nb}} |\hat{I}_A(p^{h+1/2}) - \hat{I}_{\mathrm{ref}}(p^{h+1/2})|}{\mathrm{Nb}}. \tag{5.3.5}$$

The MC and PS intensities are calculated several times increasing the number of rays to improve the accuracy. Table 5.1 and 5.2 describe how the number of rays traced affects the error. In Table 5.1 the correlation between α_c and the number of rays is evident. Note that increasing the number of rays the value of α_c and the corresponding error decrease.

Table 5.1: **Errors of the PS intensity**

Number of rays	$\varepsilon_q^{\max}$	$\varepsilon_q^{\min}$	$\varepsilon_p^{\max}$	$\varepsilon_p^{\min}$	α_c	PS error
3 363	0.9	0.1	0.50	0.025	0.119	$1.20 \cdot 10^{-3}$
6 949	0.5	0.050	0.25	0.020	0.098	$2.50 \cdot 10^{-4}$
15 870	0.4	0.025	0.02	0.001	0.050	$5.49 \cdot 10^{-5}$
37 455	0.2	0.020	0.10	0.005	0.037	$2.00 \cdot 10^{-5}$
66 855	0.1	0.009	0.05	0.004	0.020	$1.00 \cdot 10^{-5}$

In Table 5.2 the numerical results of MC ray tracing are reported. Increasing the number of rays traced in MC ray tracing, the error gradually decreases. In Figure 5.9, the results listed in Table 5.1 and Table 5.2 are shown. The red line depicts the con-

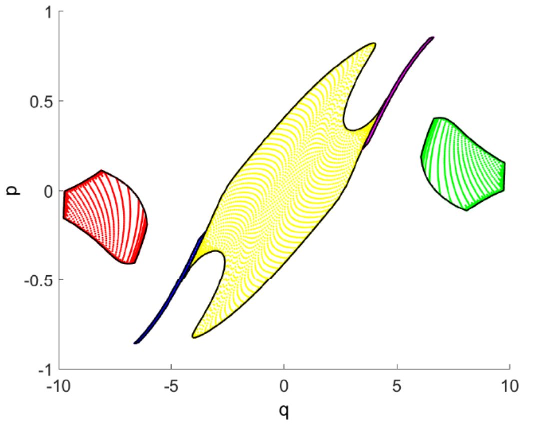

Figure 5.7: **Target PS representation.** A set of $1.67 \cdot 10^4$ rays are traced. Rays that follow the same path are depicted with the same color. The choice of the colors is constistent with Figure 5.5. The boundaries $\partial R(\Pi)$ are computed through the α-shapes method with $\alpha = \alpha_c = 0.139$.

Table 5.2: **Error values of the MC intensity**

Number of rays	MC error
972	$2.10 \cdot 10^{-3}$
9 714	$6.69 \cdot 10^{-4}$
97 103	$2.08 \cdot 10^{-4}$
971 627	$7.00 \cdot 10^{-5}$
9 716 519	$2.00 \cdot 10^{-5}$

vergence of the PS error and the blue line indicates the MC error. Note from Figure 5.9 that the error for the MC method decreases as $\frac{1}{\sqrt{\mathrm{Nr}}}$, while for the PS simulation the speed of convergence is much higher.

We need to emphasize that the PS ray tracing convergence may change according to the design of the optical system. This is because the approximation of the boundaries in PS depends on the accuracy of the α-shapes method. The α-shapes procedure is unable to properly detect the boundaries of regions with a sharp turn if not enough points are given [52]. Indeed, on the one hand a low density requires a large value of α to accept the triangles in a region, on the other hand, choosing α large, the shape of the region could be destroyed (some triangles inside the regions could be taken into account). Figure 5.10 clarifies this concept showing that the region formed by rays that hit the lens is hard to approximate when there is a small number of rays inside the region. Consequently either a region bigger than the area covered by the rays is considered or some triangles which are not part of the boundaries are considered in the triangulation. This results in an inaccurate calculation of the intensity (either too high or to low). To obtain a good approximation of the boundaries of these kind of patches more rays have to be traced. The PS error decreases very fast increasing the

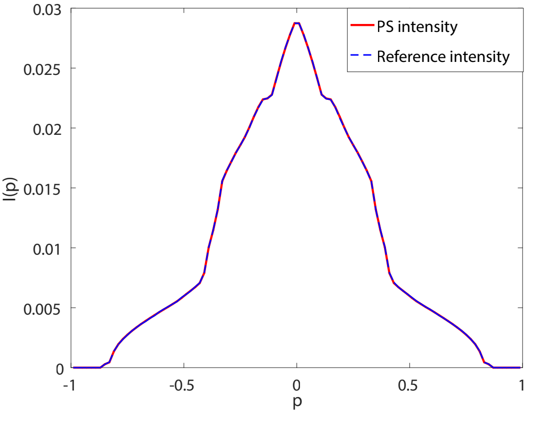

Figure 5.8: **Target intensity profile.** The exact intensity is computed using the MC method for a set of $1.7 \cdot 10^8$ rays. For the PS intensity a set of $6.6 \cdot 10^4$ rays is considered and $\alpha_c = 0.02$ is chosen to compute the boundaries $\partial R(\Pi)$.

number of rays (see Table 5.1 and Figure 5.9).

To show how the error plot changes according to the regularity of the shape of the regions $\partial R(\Pi)$, we consider another example of a TIR-collimator. Figure 5.10 shows that the hardest region to approximate is given by those rays that follow path $\Pi_1 = (1, 2, 7, 12)$. We therefore consider a TIR-collimator with a flatter lens and with the target located at a closer distance from the top (see Figure 5.11). The source $\mathcal{S} = [-2, 2]$ (surface number 1) is located in air at a height $z_1 = 0.3$ from the x-axis. The target $\mathcal{T} = [-9.7, 9.7]$ (surface 12) is parallel to the source and is located in air at a height $z = 7.85$. The shape of the collimator is shown as a blue line. Three detectors depicted with green lines (surfaces 13, 14, and 15) are located at the left, the right and the bottom of the optical system.

Tracing 3281 rays using PS ray tracing, we obtain the target rays distribution shown in Figure 5.12. Compared it with the distribution in Figure **??**, we note that a flatter lens removes one of the two spikes of the region formed by the rays that hit the lens. Moreover a target located very close to the top makes the shape of that region less stretched along the q-axis. Therefore, it is expected that α-shapes method performs well, even for a small number of rays.

PS and MC ray tracing are implemented for the TIR-collimator in Figure 5.12. The approximated intensities $\hat{I}_{\mathrm{A}}$ ($\mathrm{A} = \mathrm{PS}, \mathrm{MC}$) are compared with the reference intensity $\hat{I}_{\mathrm{ref}}$ (MC ray tracing with 10^7 rays). PS error is depicted with the red line and, MC error is depicted with the blue line.

For the TIR-collimator in Figure 5.11 we obtained a speed of convergence of the order of $O\left(\frac{1}{\mathrm{Nr}}\right)$ for PS ray tracing versus an order of convergence of $O\left(\frac{1}{\sqrt{\mathrm{Nr}}}\right)$ for MC ray tracing.

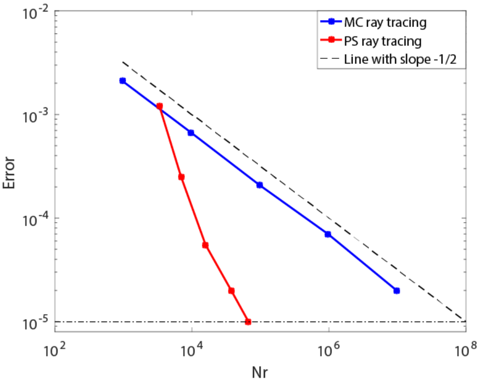

Figure 5.9: **PS and MC errors as a function of the number of rays** The horizontal dotted line shows that an error equal to $2.00 \cdot 10^{-5}$ can be obtained tracing at least 10^2 times fewer rays in phase space.

5.4 Conclusion

The aim of this chapter was using α-shapes to detect the boundaries of the regions formed by the rays traced.

First, we reported some theory about α-shapes which are commonly used to approximate the shape formed by a point cloud. These methods depend on a parameter α that in most cases can be determined only by several simulations.

Using étendue conservation, we developed a new approach to detect the value of α that better approximates the boundaries in target PS. We applied α-shapes to two different kinds of TIR-collimators. The target PS intensity was computed for both systems several times increasing every time the number of rays traced. Finally, the corresponding errors between the intensities found and a reference intensity was calculated. We observed that PS ray tracing leads to trace far less rays compared to MC ray tracing. Numerical results show that using PS ray tracing the desired accuracy can be achieved reducing significantly the number of rays traced..

However, we observed that the error convergence for PS ray tracing strongly depends on the design of the optical system (shapes of the region in target PS). Indeed, the intensity accuracy is related to the precision of the α-shape, that is, to the choice of the parameter value of α. For more complicated shapes in PS, more rays need to be traced for a good boundaries reconstruction.

In order to remove the dependence of PS ray tracing on the parameter α, we will construct another procedure to detect the boundaries of the regions in target PS. The new technique is based on the triangulation refinement explained in Section 4.3. The details are explained in the next chapter and numerical results are reported for several optical systems.

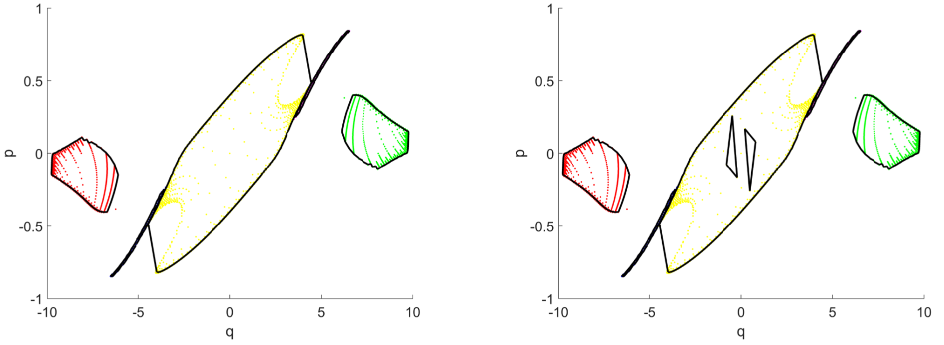

(a) Boundaries approximation obtained using the α-shapes method with $\alpha_c = 0.3$ (black lines).

(b) Boundaries approximation obtained using the α-shapes method with $\alpha_c = 0.31$ (black lines).

Figure 5.10: **Approximated boundaries at the target PS.** Tracing 3339 rays and using α-shapes, the boundaries cannot be approximated well. A small change of the parameter α leads to a completely different approximation of the boundaries.

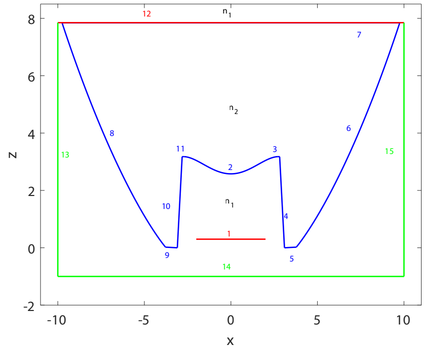

Figure 5.11: **Shape of the TIR-collimator.** Each surface of the system is labeled with a number. $n_1 = 1$ is the refraction index of the medium (air) where the source and the target are located, and $n_2 = 1.5$ the refraction index of the medium (glass) inside the optical system. The sagitta of the lens is equal to 0.6.

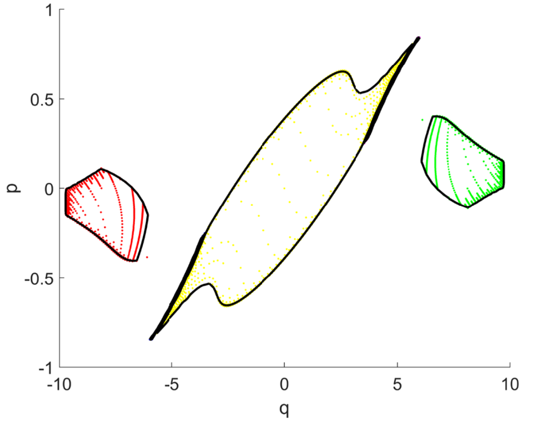

Figure 5.12: **Target phase space for the TIR-collimator depicted in Figure 5.11.** The black line depicts the best approximation of $\partial R(\Pi)$ for 3281 rays. The α-shapes method gives an accurate approximation of the boundaries for $\alpha_c = 0.9$.

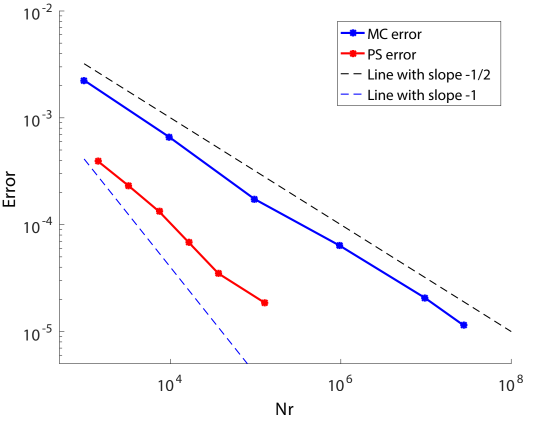

Figure 5.13: **PS and MC errors.** The errors are in a logarithmic scale.

Chapter 6

The triangulation refinement

The purpose of this chapter is to provide an alternative approach to the α-shapes methods for determining the boundaries $\partial R(\Pi)$ in target PS. Our method is based on the triangulation refinement of the source PS explained in Section 4. We have seen that, using the triangulation refinement, more rays close to the boundaries are traced selecting increasingly smaller values for the parameters $\varepsilon_{q_1}^{\min}$ and $\varepsilon_{p_1}^{\min}$. Once the algorithm stops, only the triangles that are expected to be crossed by a boundary are taken into account. By construction, each of these triangles has two vertices that follow the same path and one vertex that follows another path. The triangles are ordered in such a way that two of them are neighbors if they have a side in common. Given a path Π the corresponding boundary $\partial R_1(\Pi)$ is approximated by those vertices of the triangles which corresponding rays follow path Π. The boundaries $\partial R(\Pi)$ at the target are given by

$$\mathrm{M}(\partial R(\Pi)) : \partial R_1(\Pi) \rightarrow \partial \mathrm{R}(\Pi), \tag{6.0.1}$$

where $\mathrm{M}(\partial R(\Pi))$ is the restriction of M, defined in Equation (4.3.1), to $\partial R(\Pi)$ for every path Π.

In this chapter we develop a criterion to establish the value of the parameters $\varepsilon_{q_1}^{\min}$, $\varepsilon_{q_1}^{\max}$, $\varepsilon_{p_1}^{\min}$ and $\varepsilon_{p_1}^{\max}$ that gives a good approximation of $\partial R(\Pi)$. Similar to what it was done for selecting α in the α-shapes procedure, the triangulation parameters are selected using the étendue conservation in PS. The core of our approach is the following.

The étendue U_1 at the source PS S related to all the rays that arrive at the target is calculated. If all the rays emitted by the source are received by the target, U_1 can be easily determined by using Equation (5.2.1), otherwise Equation (5.2.2) needs to be computed.

The étendue U_t at the target PS T is computed using Equations (5.2.5) and (5.2.7). To calculate the integral in Equation (5.2.7), the triangulation refinement method is applied to the regions $R(\Pi)$ for a range of values of $\varepsilon_{q_1}^{\max}$ and for a fixed value of $\varepsilon_{q_1}^{\min}$. The parameters along the q-axis are scaled as $\varepsilon_{p_1}^{\max} = \varepsilon_{q_1}^{\max}/w$ and $\varepsilon_{p_1}^{\min} = \varepsilon_{q_1}^{\min}/w$ with $w = (p_1^{\max} - p_1^{\min})/(q_1^{\max} - q_1^{\min})$ where $p_1^{\min}$ and $p_1^{\max}$ are the minimum and the maximum p-coordinate in S, respectively, and $q_1^{\min}$ and $q_1^{\max}$ are the minimum and the maximum q-coordinate in S, respectively. An approximation of the boundaries

$\partial R(\Pi)$ is obtained for each of those parameters values. Then, the intersection points $(q^i(\Pi, p), \Pi)_{i=1,\cdots,r}$ between $\partial R(\Pi)$ and the horizontal line $p = const$ are calculated for each path Π, and for $p \in [-1, 1]$. Ordering their q-coordinates in ascending order, the integral in Equation (5.2.7) is computed. Changing the values of the parameters, different approximations of $\partial R(\Pi)$ are found and, consequently, different values of U_{t}

In order to use the parameters that give a good accuracy of the target photometric variables, the difference $\Delta U = U_1 - U_{\mathrm{t}}$ is calculated for every value of U_{t} found. The values of the parameters that give the smaller distance Δ define the more accurate triangulation at source PS S. Hence, these values are chosen for the computation of the target photometric variables.

The method explained above is tested for several optical systems. The results are presented next.

6.1 The two-faceted cup

In this paragraph we apply the triangulation refinement in PS to the two-faceted cup described in Chapter 3 and depicted in Figure 3.1. We start tracing rays inside the system using PS ray tracing as explained in Chapter 4. To avoid rays parallet to the source and that leave the endpoints, we consider rays with initial direction $p_1 \in [-1 + 10^{-6}, 1 - 10^{-6}]$ and initial position $q \in [-2 + 10^{-12}, 2 - 10^{-12}]$. In order to define a stopping criterion for the triangulation, we apply étendue conservation. Since the two-faceted cup is formed by only reflective lines and its target is adjacent to the left and the right reflector (it is located exactly at the top of the system), all the rays emitted by the source arrive to the target. Thus,

$$U_1 = U \approx 8, \tag{6.1.1}$$

where the second equality follows from Equation (5.2.1) with $n_1 \sin(\theta_1^{\max}) = p_1^{\max} = 1 - 10^{-6}$ and $a = 2 + 10^{-12}$.

To define a stopping criterion for the triangulation at the source PS and determine how many rays are needed to acieve a good accuracy of the target intensity, we compute the target étendue U_{t} and we compare the approximated value with the exact value at the source U_1. To this purpose, ray tracing in PS is implemented for a range of values of $\varepsilon_{q_1}^{\min}$, $\varepsilon_{q_1}^{\max} = 1$, $\varepsilon_{p_1}^{\max} = \varepsilon_{q_1}^{\max}/w$, and $\varepsilon_{p_1}^{\min} = \varepsilon_{q_1}^{\min}/w$ where $w = (p_1^{\max} - p_1^{\min})/(q_1^{\max} - q_1^{\min}) \approx 2$. The approximated boundaries are computed for each of these values joining the vertices of those triangles crossed by a boundary that follow the same path Π. In Figure 6.1 we show, with the black lines, the boundaries of $R_1(\Pi)$ and $R(\Pi)$ found for two different values of $\varepsilon_{q_1}^{\min}$. Note that, decreasing $\varepsilon_{q_1}^{\min}$, the number of rays increases. In order to understand which value of $\varepsilon_{q_1}^{\min}$ gives the best approximation of the boundaries and, consequently, of the target photometric variable, we calculate U_{t} for the every set of rays traced using Equation (5.2.7). Then the difference

$$\Delta U = U_1 - U_{\mathrm{t}} \tag{6.1.2}$$

is found. An accurate approximation of U_{t} gives a small value of ΔU. For instance, for the two set of rays depicted Figures 6.1 we found $\Delta U \approx 0.53$ for $\varepsilon_{q_1}^{\min} = 0.1$ and $\Delta U \approx 0.13$ for $\varepsilon_{q_1}^{\min} = 0.05/2$. This give the insight that the boundaries computation

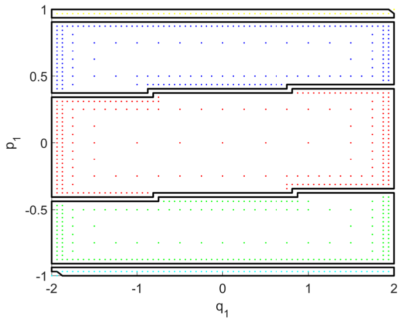

(a) The black lines are the boundaries at S. 1500 rays are traced using the triangulation refinement with $\varepsilon_{q_1}^{\min} = 0.1$.

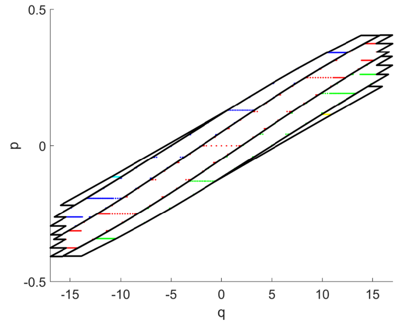

(b) The black lines are the boundaries at T. 1500 rays are traced using the triangulation refinement with $\varepsilon_{q_1}^{\min} = 0.1$.

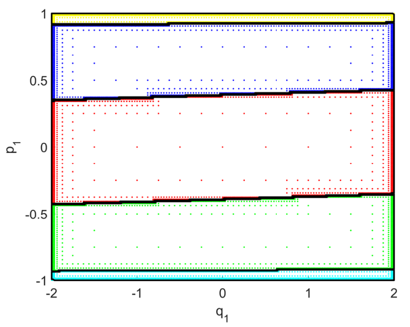

(c) The black lines are the boundaries at S. 7500 rays are traced using the triangulation refinement with $\varepsilon_{q_1}^{\min} = 0.05/2$.

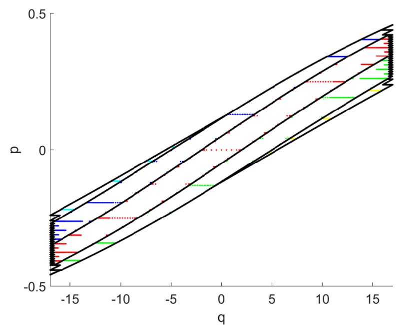

(d) The black lines are the boundaries at T. 7500 rays are traced using the triangulation refinement with $\varepsilon_{q_1}^{\min} = 0.05/2$.

Figure 6.1: **Boundaries at $\boldsymbol{S}$ and $\boldsymbol{T}$ of the two-faceted cup.** The approximated boundaries are computed using the triangulation refinement with two different values of $\varepsilon_{q_1}^{\max}$.

obtained using $\varepsilon_{q_1}^{\min} = 0.05/2$ is more accurate.

In Figure 6.2 we show with the blue line how the target étendue varies as a function of the parameter $\varepsilon_{q_1}^{\min}$ where the other parameter have always a fixed value. The exact étendue $U = 8$ is depicted with the red line and it is computed using Equation (5.2.7). By decreasing $\varepsilon_{q_1}^{\min}$ an increase of U_{t} is observed. Furthermore, by construction, U_{t} is always underestimated because the approximated boundaries are found joining the vertices of the *boundaries triangles* which are *inside* the regions $R(\Pi)$. Where the *boundary triangles* are those crossed by a boundary. Referring as Figure 6.2, the best approximation of U_{t} is obtained tracing around $1.2 \cdot 10^5$ rays using PS ray tracing with parameters $\varepsilon_{q_1}^{\min} = 0.8 \cdot 10^{-4}$, $\varepsilon_{q_1}^{\max} = 1$, $\varepsilon_{p_1}^{\min} = \varepsilon_{q_1}^{\min}/2$ and $\varepsilon_{q_1}^{\max} = \varepsilon_{q_1}^{\max}/2$.

The PS intensity $\hat{I}_{PS}$ with $1.2 \cdot 10^5$ rays is calculated using Equation (4.3.4). The intensity profile is shown in Figure 6.3 with the red line. In the same graph we show the reference intensity $\hat{I}_{\mathrm{ref}}$ with the dotted blue line. For the two-faceted cup the reference intensity is actually the exact intensity ($\hat{I}_{\mathrm{ref}} = \hat{I}_{\mathrm{exact}}$).

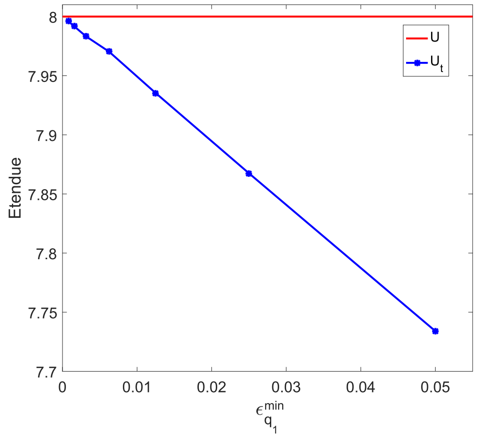

Figure 6.2: **Etendue for the two faceted cup.** The total étendue as an area in PS is depicted with the red line. The approximated étendue for a range of values of $\varepsilon^{\min}_{q_1}$ is shown with the blue line.

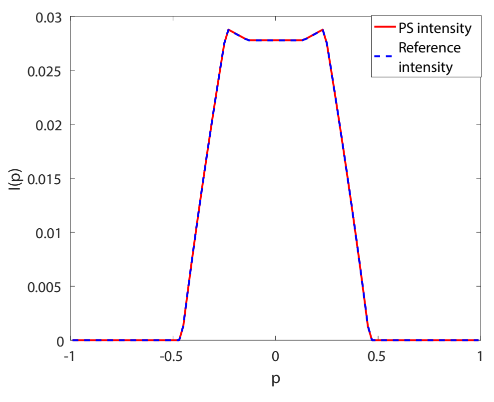

Figure 6.3: **Intensity profile at the target of the two faceted cup.** The reference intensity is an analytic intensity. The PS intensity is computed using the triangulation refinement with $\varepsilon^{\min}_{q_1} = 0.8 \cdot 10^{-4}$, $\varepsilon^{\max}_{q_1} = 1$, $\varepsilon^{\min}_{p_1} = \varepsilon^{\min}_{q_1}/2$ and $\varepsilon^{\max}_{p_1} = \varepsilon^{\max}_{q_1}/2$. Around $1.2 \cdot 10^5$ rays are traced.

Finally, we compare PS ray tracing with both MC and QMC ray tracing by computing the error between the approximated intensities $\hat{I}_{\mathrm{A}}(\mathrm{A} = \mathrm{MC}, \mathrm{QMC}, \mathrm{PS})$ and the exact intensity $\hat{I}_{\mathrm{ref}}$ defined in Equation (5.3.5) with $\mathrm{Nb} = 100$. The results are shown in Figure 6.4 where MC, QMC and PS intensity are depicted with the green, blue and red line, respectively. The results for the two-faceted cup show that using PS and the triangulation refinement for the boundaries computation requires tracing far less rays compared to MC ray tracing. An error comparison between QMC ray tracing and PS ray tracing shows that more rays are needed in PS. This can be due to the

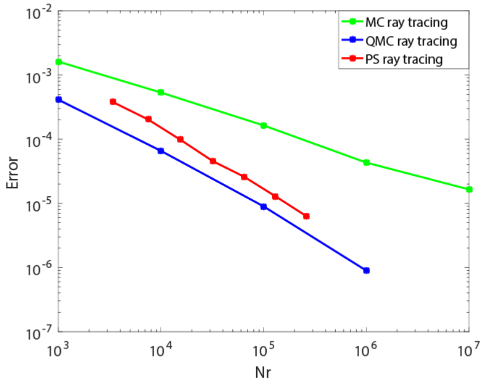

Figure 6.4: **Error plot for the two faceted cup.** The errors between the approximated intensities $\hat{I}_{\mathrm{A}}(\mathrm{A} = \mathrm{MC}, \mathrm{QMC}, \mathrm{PS})$ and the exact intensity $\hat{I}_{\mathrm{exact}}$ are shown in a logarithmic scale. Using PS ray tracing far less rays need to be traced compared to MC ray tracing but still more rays than QMC ray tracing are needed.

fact that with the triangulation refinement we always underestimate the value of the étendue at the target. Although, the shape of all the regions $R(\Pi)$ are very smooth, their boundaries are difficult at the edge of the target phase space T to approximate by triangles. With the triangulation refinement, as far as is fine the triangulation, the vertical and straight lines at the edge of T are always approximate by a broken line. On the contrary, since the two-faceted cup is a very simple system, QMC ray tracing does not requires a huge number of rays to obtain the desired accuracy. Nevertheless, PS ray tracing has a big advantage compared to QMC ray tracing. Indeed, as we have seen in Chapter 3, MC and QMC ray tracing are binning procedure. Therefore, the MC and QMC intensities are given by the average over every bin and the error also depends on the number of bins. This part of the error is not included in the results provided in Figure 6.4 as there we have fixed the number of bins Nb = 100. PS ray tracing gives a pointwise intensity along all the possible directions. In the simulations shown in this thesis we always compute the average PS intensity. This is needed to give a fair comparison of PS ray tracing with MC and QMC ray tracing. Note that no error related to the number of bins is included in the PS method.

In order to investigate in more details the PS ray tracing performances, we test the procedure for more complicated systems. In the next paragraph we present the results for a TIR-collimator.

6.2 A TIR-collimator

In this section we provide the results of PS ray tracing for a TIR-collimator, using the triangulation refinement to compute the boundaries $\partial R(\Pi)$ in target PS. In particular, we consider the TIR-collimator depicted in Figure 5.11. Since this system is located in two different media (air and glass), also refraction law plays a role in the ray tracing procedure. We implement PS ray tracing for the TIR-collimator gradually increasing the number of rays, i.e. gradually decreasing the values of the parameters $\varepsilon_{q_1}^{\min}, \varepsilon_{q_1}^{\max}, \varepsilon_{p_1}^{\min}$ and $\varepsilon_{p_1}^{\max}$ in the triangulation. In order to trace more rays close to the boundaries, we decide to vary only the value of $\varepsilon_{q_1}^{\min}$ and $\varepsilon_{p_1}^{\min}$ which determine the number of triangles close to the boundaries and we hold fixed the values of $\varepsilon_{q_1}^{\max}$ and $\varepsilon_{p_1}^{\max}$ as they are responsible of the number of rays inside the regions $R(\Pi)$. Every ray traced has initial position coordinate $q_1 \in [-a, a]$ with $a = 2$ and the initial direction coordinate $p_1 = [-1.1]$. Therefore, the source PS of the TIR-collimator is the rectangular $S = [-2, 2] \times [-1, 1]$. The parameters $\varepsilon_{p_1}^{\min}$ and $\varepsilon_{p_1}^{\max}$ are scaled as follows:

$$\begin{aligned} w &= \frac{p_1^{\max} - p_1^{\min}}{q_1^{\max} - q_1^{\min}} = 2, \\ \varepsilon_{p_1}^{\min} &= \frac{\varepsilon_{q_1}^{\min}}{w}, \\ \varepsilon_{p_1}^{\max} &= \frac{\varepsilon_{q_1}^{\max}}{w}. \end{aligned} \tag{6.2.1}$$

To determine the triangulation refinement that gives a good approximation of the target intensity we compare U_1 (source étendue) to U_t (target étendue) and use étendue conservation property. Now, not all light emitted by the source of the TIR-collimator arrives at its target. Indeed, using PS ray tracing Np = 7 different paths $(\Pi_j)_{j=1,\cdots,\mathrm{Np}}$ are found but only five of them are paths from the source (line 1) to the target (line 12), see Section 5.3. Thus, we need to remove from the total area of S those parts occupied by the rays that arrive at some others detectors and not at the target. The source PS is given by:

$$U_1 = 8 - 2A_T \approx 7.77. \tag{6.2.2}$$

The target étendue U_t is obtained from Equation (5.2.6) for a range of values of $\varepsilon_{q_1}^{\min}$ and with $\varepsilon_{q_1}^{\max} = 1$ fixed. Likewise, the two-faceted cup, the boundaries $\partial R(\Pi)$ are found for every value of $\varepsilon_{q_1}^{\min}$, and U_t is calculated for each of these boundaries. The results shown in Figure 6.5 give the étendue plot a function of $\varepsilon_{q_1^{\min}}$.

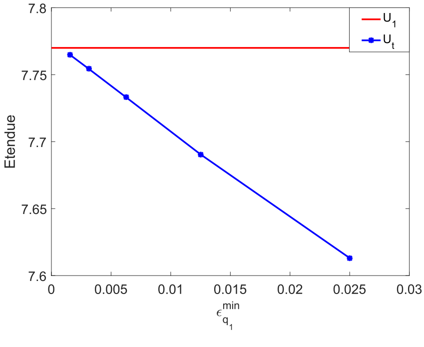

Figure 6.5: **Etendue of the TIR-collimator.** A comparison between U_1 and U_t shows that by decreasing the value of $\varepsilon_{q_1^{\min}}$, $\Delta U = U_1 - U_\mathrm{t}$ decreases.

The boundaries $\partial R_1(\Pi_j)$ and $\partial R(\Pi_j)$ with $j = \{1, \cdots, 5\}$ computed using the triangulation refinement with $\varepsilon_{q_1}^{\min} = 1.6 \cdot 10^{-3}$ are shown in Figure 6.6 with the black lines. Around $1.62 \cdot 10^5$ rays are traced using the triangulation refinement in PS with $\varepsilon_{q_1}^{\min} = 1.6 \cdot 10^{-3}, \varepsilon_{q_1}^{\max} = 1, \varepsilon_{p_1}^{\min} = \varepsilon_{q_1}^{\min}/2$ and $\varepsilon_{p_1}^{\max} = \varepsilon_{q_1}^{\max}/2$.

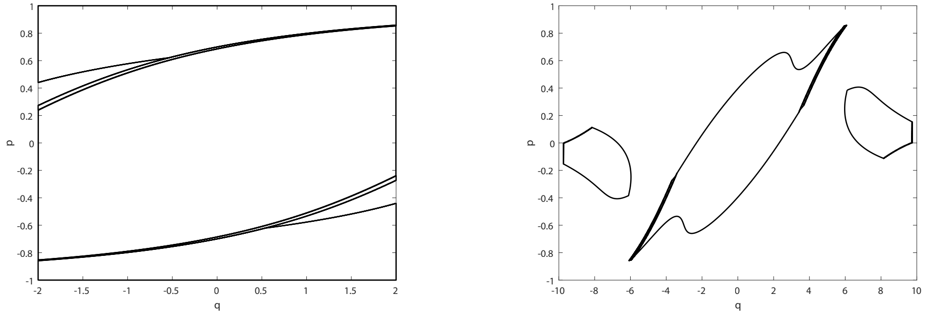

(a) Boundaries at the source PS.

(b) Boundaries at the target PS.

Figure 6.6: **Boundaries at $\boldsymbol{S}$ and $\boldsymbol{T}$ of the TIR-collimator** The black lines show the boundaries found using $\varepsilon_{q_1}^{\min} = 1.6 \cdot 10^{-3}$ in the triangulation refinement of the source PS.

The target PS intensity $\hat{I}_{\mathrm{PS}}$ is found for those parameters and it is compared with a reference intensity $\hat{I}_{\mathrm{ref}}$ which is given by QMC ray tracing with 10^7 rays (as the exact intensity for the TIR-collimator is unknown). The profile of the two intensities is given in Figure 6.7. The difference between the two intensity profiles is not discernible by eye.

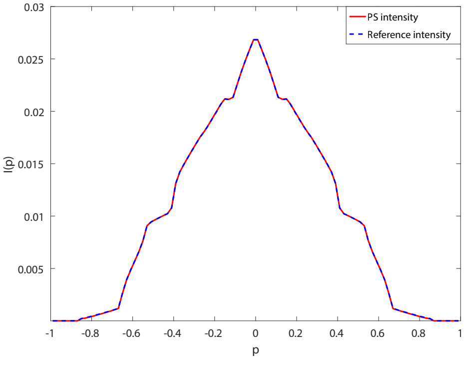

Figure 6.7: **Target intensity for the TIR-collimator.** The PS intensity $\hat{I}_{\mathrm{PS}}$ is computed using PS ray tracing with around $1.62 \cdot 10^5$ rays. The reference intensity $\hat{I}_{\mathrm{ref}}$ is obtained by QMC ray tracing with 10^7 rays.

To validate our method, PS ray tracing is compared to both MC and QMC ray tracing. The error between the approximated intensities $\hat{I}_{\mathrm{A}}(\mathrm{A} = \mathrm{QMC}, \mathrm{MC}, \mathrm{PS})$ and the reference intensity $\hat{I}_{\mathrm{ref}}$ as a function of the number of rays traced is calculated.

The error plot is shown in Figure 6.8 where the green line shows the MC, QMC and PS convergences are shown with the green, the blue and the red line, respectively.

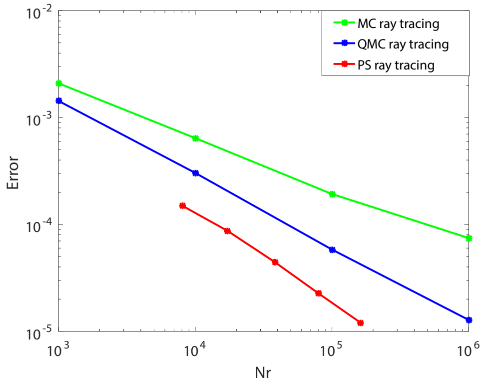

Figure 6.8: **Error as a function of the number of rays** The PS intensity $\hat{I}_{\text{PS}}$ is computed using PS ray tracing with around $1.62 \cdot 10^5$ rays. The reference intensity $\hat{I}_{\text{ref}}$ is obtained by QMC ray tracing with 10^7 rays.

Finally, in order to show the advantages of PS ray tracing in terms of the computational time, in Figure 6.9 we provide an error convergence as a function of the CPU-time for MC, QMC and PS raytracing. The choice of the colours is consistent with Figure 6.7.

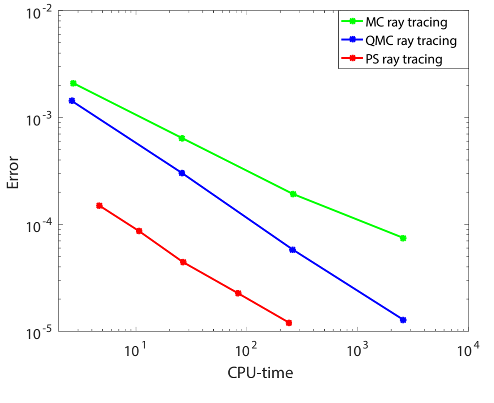

Figure 6.9: **Error as a function of the CPU-time** The PS intensity $\hat{I}_{\text{PS}}$ is computed using PS ray tracing with around $1.62 \cdot 10^5$ rays. The reference intensity $\hat{I}_{\text{ref}}$ is obtained by QMC ray tracing with 10^7 rays.

The results shown in Figures 6.8 and 6.9 are reported in Tables 6.1 and 6.2.

Table 6.1: **Errors of the PS intensity**

$\varepsilon_q^{\max}$	Nr	Etendue	PS error	CPU-time (sec.)
0.05	3 547	7.50	$1.75 \cdot 10^{-4}$	1.98
0.025	8 055	7.61	$1.49 \cdot 10^{-4}$	4.69
0.125	17 300	7.69	$8.68 \cdot 10^{-5}$	10.61
$6.3 \cdot 10^{-3}$	38 300	7.73	$4.43 \cdot 10^{-5}$	26.56
$3.1 \cdot 10^{-3}$	79 600	7.75	$2.27 \cdot 10^{-5}$	83, 21
$1.6 \cdot 10^{-3}$	162 300	7.76	$1.20 \cdot 10^{-5}$	240.53

Table 6.2: **Errors of the MC intensity and QMC intensity**

Nr	MC error	QMC error	CPU-(MC)time (sec.)	CPU-(QMC)time (sec.)
10^3	$2.09 \cdot 10^{-3}$	$1.43 \cdot 10^{-3}$	2.73	2.63
10^4	$6.42 \cdot 10^{-4}$	$3.03 \cdot 10^{-4}$	25.98	25.84
10^5	$1.92 \cdot 10^{-4}$	$5.82 \cdot 10^{-5}$	259.92	258.28
10^6	$7.45 \cdot 10^{-5}$	$1.28 \cdot 10^{-5}$	2585.83	2482.67

6.3 A Parabolic reflector

Given a Cartesian coordinate system (x, z), the two-dimensional system in Figure 6.10 is defined in the (x, z)-plane. It consists of a source S (line 1), a target T (line 4) parallel to S and two reflectors (lines 2 and 3) which are arcs of the same parabola. The minimum of the parabola is located at the point with x-coordinate equal to 0. $\mathsf{S} = [\text{-a}, \text{a}]$ (with $\text{a} = 2$) and $\mathsf{T} = [-\text{b}, \text{b}]$ (with $\text{b} = 17$) are lines perpendicular to the optical axis and are located at $z = 0$ and $z = 40$, respectively. All the optical lines are located in air, therefore the index of refraction $n_i = 1$ for every line $i = 1, \cdots, 4$. The optical axis of the system in Figure 6.10 corresponds to the z-axis.

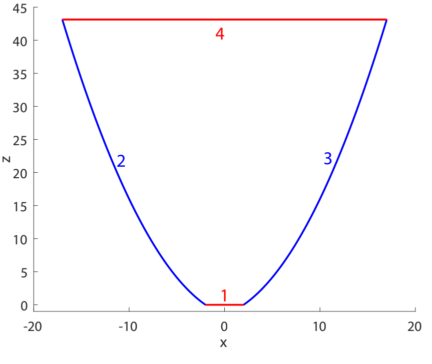

Figure 6.10: The two-dimensional optical system with parabolic mirrors. Each line of the system is labeled with a number. The source S= $[2, 2]$ (line 1) is located on the x-axis. The target T= $[-17, 17]$ (line 4) is parallel to the source and is located at a height $z = 40$. The left and right reflectors (lines 2 and 3) are arcs of the same parabola.

6.4 The Compound Parabolic Concentrator (CPC)

Chapter 7

The inverse ray mapping method: analytic approach

PS ray tracing based on the source and the target PS constitutes an improvement of MC and QMC ray tracing. Now, a method that employs not only the source and the target PS but also the PS of *all* the other lines that constitute the optical system is introduced. All lines can be modeled as detectors of the incident light and emitters of the reflected light. Moreover, we assume that the source can only emit light and the target can only receive light. Therefore, one PS is taken into account for the source and one for the target while both the source and target phase spaces are considered for the other lines. Every line of the system (except for the source S and the target T) constitutes the target for incident rays and the source for reflected rays. Therefore, two different phase spaces are considered for the reflectors and one PS for S and T. All these phase spaces are connected through a map which relates the rays coordinates on every PS. In order to compute the target photometric variables an inverse ray mapping reconstruction from the target to the source is involved.

In this chapter two different optical systems are investigated. First, the method is explained for the two-faceted cup. Then, it is extended to a more complicated system, the so-called multi-faceted cup, which is formed by only straight lines segments.

7.1 Explanation of the method

Using the PS of *all* the lines that form the system, a map from the source to the target of the system is constructed. This map can be written as the concatenation of many maps which can be classified as two different kinds of maps, i.e. the map that connects the source and the target PS of two *different* lines and the map that connects the target and the source PS of the *same* line. Employing the inverses of these maps we are able to detect the parts on target PS illuminated by the source. All the PS considered are divided into regions, the boundaries of which can be determined exactly for systems formed by straight lines. We make the assumption of a Lambertian source; hence, the luminance is a positive constant when different from 0. As a consequence, the output intensity along a given direction is given by the total width of all the patches with positive luminance, measured along that direction.

Next, the details of the procedure are explained for a very simple optical system: the two-faceted-cup.

7.2 The two-faceted cup

A two-faceted cup is formed by a source S, a target T and two reflectors which are straight lines segments. As an example, we consider the two-faceted cup introduced in Chapter 3 and depicted in Figure 3.1. We use the same notations of Chapter 4 to indicate the PS $S = Q \times P$ and the rays coordinates (q, p) in S.

Let's now introduce some new notation. The source and the target PS of a line j are indicated with S_j and T_j, respectively. The coordinates of every ray that reaches the line $j \in \{1, 2, 3\}$ are indicated with $(q_{\mathrm{t},j}, p_{\mathrm{t},j})$ on T_j. After reflection, the ray leaves line $j \in \{1, 2, 3\}$ at the same position and with a new direction, the new coordinates are indicated with $(q_{\mathrm{s},j}, p_{\mathrm{s},j})$ on S_j. Note that $q_{\mathrm{s},j} = q_{\mathrm{t},j}$ while $p_{\mathrm{s},j}$ is obtained applying the reflection law to the direction coordinate $p_{\mathrm{t},j}$ of the incident ray. The phase spaces S_j and T_j of each line j are partitioned into different regions, $(S_{j,k})_{k=2,3,4}$ and $(T_{j,l})_{l=1,2,3}$, respectively, where $k \neq j$ is the index of the line that is illuminated by j and $l \neq j$ is the index of the line that illuminates j. Hence, we indicate with $S_{j,k} \subset S_j$ the part of S_j corresponding to rays that illuminate line k and with $T_{j,l} \subset T_j$ the part of T_j corresponding to rays originating from the line l. Note that, due to the fact that the source only emits light, we do not define its target phase space T_1. Similarly, since the target only receives light, its source phase space S_4 is not defined. For the two-faceted cup, six different phase spaces need to be considered which are given by the following expressions:

$$
\begin{aligned}
S_1 &= S_{1,2} \cup S_{1,3} \cup S_{1,4}, \\
S_2 &= S_{2,3} \cup S_{2,4}, \\
S_3 &= S_{3,2} \cup S_{3,4}, \\
T_2 &= T_{2,1} \cup T_{2,3}, \\
T_3 &= T_{3,1} \cup T_{3,2}, \\
T_4 &= T_{4,1} \cup T_{4,2} \cup T_{4,3}.
\end{aligned}
\tag{7.2.1}
$$

We need to note that, as the source cannot receive light and the target cannot emit light, the regions $(S_{j,1})_{j=2,3}$ and $(T_{j,4})_{j=2,3}$ are not considered. The boundaries $\partial S_{j,k}$ are mapped into the boundaries $\partial T_{k,j}$ for every $j = \{1, 2, 3\}$ and $k = \{2, 3, 4\}$ with $k \neq j$ (edge-ray principle [**?**]). For the two-faceted cup and for all systems that are formed by straight lines, they are determined analytically as explained in the following. Given two lines j and l with $j \neq l$, we show how to compute the boundaries of the region formed by the rays that leave line j and hit line l. We do that both on S_j and on T_l. We indicate with $(\operatorname{var} x_{j,\ell}, \operatorname{var} z_{j,\ell})$ and with $(\operatorname{var} x_{j,\mathrm{r}}, \operatorname{var} z_{j,\mathrm{r}})$ the coordinates of the points located at the left and the right extreme of line j, respectively. Similarly, $(\operatorname{var} x_{l,\ell}, \operatorname{var} z_{l,\ell})$ and $(\operatorname{var} x_{l,\mathrm{r}}, \operatorname{var} z_{l,\mathrm{r}})$ are the coordinates of the points located at the left and the right extreme of line l, respectively. The boundaries $\partial S_{j,l}$ and $\partial T_{l,j}$ are obtained considering all the rays that leave the extremes of line j and all the rays that reach the extremes of the target. Given two lines j and l with $j \neq l$, $\partial S_{j,l}$ and $\partial T_{l,j}$

are formed by four different curves, two of them are given by all the rays that leave the end points of line j and hit line l and, the others two are given by the rays that leave the extremes of line j and hit the extremes of line l. The boundaries $\partial S_{j,l}$ and $\partial T_{l,j}$ are given by:

$$\begin{aligned} \partial S_{i,k} &= \partial S^1_{i,k} \cup \partial S^2_{i,k} \cup \partial S^3_{i,k} \cup \partial S^4_{i,k}, \\ \partial T_{k,i} &= \partial T^1_{k,i} \cup \partial T^2_{k,i} \cup \partial T^3_{k,i} \cup \partial T^4_{k,i}. \end{aligned} \tag{7.2.2}$$

In the following we explain in more details the case of $j = 1$ and $l = 4$; see Fig. 7.1.

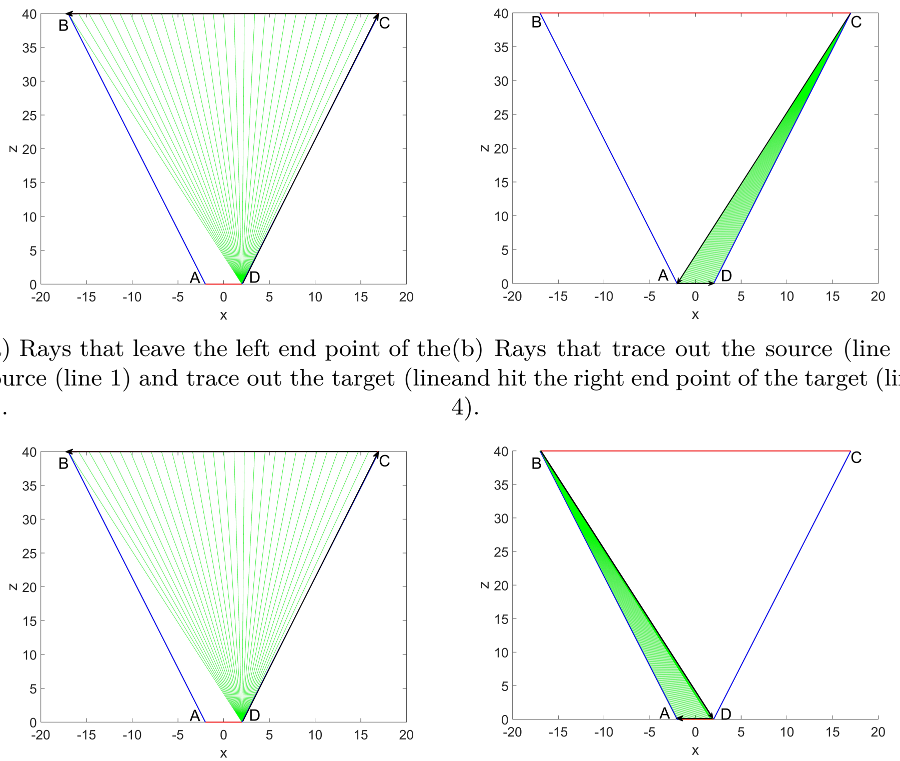

(a) Rays that leave the left end point of the source (line 1) and trace out the target (line 4).

(b) Rays that trace out the source (line 1) and hit the right end point of the target (line 4).

(c) Rays that leave the right end point of the source (line 1) and trace out the target (line 4).

(d) Rays that trace out the source (line 1) and hit the left end point of the target (line 4).

Figure 7.1: Rays located on the boundaries of the regions $\partial S_{1,4}$ and $\partial T_{4,1}$. $A = (x_{1\ell}, z_{1,\ell}) = (-2, 0)$ and $D = (x_{1,\mathrm{r}}, z_{1,\mathrm{r}}) = (2, 0)$ are the left and right corner points (or end points) of S (line 1), respectively. $B = (x_{4,\ell}, z_{4,\ell}) = (-17, 40)$ and $C = (x_{4,\mathrm{r}}, z_{4,\mathrm{r}}) = (17, 40)$, are the left and right corner points (or end points) of T (line 4), respectively.

The boundaries $\partial S_{1,4}$ and $\partial T_{4,1}$ are given in Figs. 7.2 and 7.3, respectively. $\partial S^1_{1,4}$ and $\partial T^1_{4,1}$ are obtained tracing out line 4 from $q_{4,\mathrm{min}} = -b$ to $q_{4,\mathrm{max}} = b$ by rays leaving $q_{1,\mathrm{min}} = -a$ with varying p_1, these rays are shown in Fig. 7.1a, and the boundary segments $\partial S^1_{1,4}$ and $\partial T^1_{4,1}$ are the orange line segments labeled with c. $\partial S^2_{1,4}$ and $\partial T^2_{4,1}$ are given tracing out line 1 from $q_{1,\min} = -a$ to $q_{1,\max} = a$ with varying p_1, such that all rays hit $q_{4,\max} = b$, these rays are shown in Fig. 7.1b, the boundary segments $\partial S^2_{1,4}$ and $\partial T^2_{4,1}$ are depicted in blue (lines segments labeled with d). Likewise, $\partial S^3_{1,4}$ and $\partial T^3_{4,1}$ are obtained tracing out line 4 from $q_{4,\max} = b$ to $q_{4,\min} = -b$ by rays leaving $q_{1,\max} = x_{1,\mathrm{r}} = a$ with varying p_1. These rays are shown in Fig. 7.1c, $\partial S^3_{1,4}$ and $\partial T^3_{4,1}$ are the red line segments labeled with e. Finally, $\partial S^4_{1,4}$ and $\partial T^4_{4,1}$ are given tracing out line 1 from $q_{1,\max} = a$ to $q_{1,\min} = -a$ with varying p_1, such that all rays hit $q_{4,\min} = -b$, these rays are shown in Fig. 7.1d, $\partial S^4_{1,4}$ and $\partial T^4_{4,1}$ are the green lines segments labeled with f. We remind that we use the notation (x, z) for the Cartesian coordinates system of real space, while phase space has (q, p) coordinates. It is worth noting that $q_{1,\min} = x_{1,\ell}$, $q_{1,\max} = x_{1,\mathrm{r}}$, $q_{4,\min} = x_{4,\ell}$ and $q_{4,\max} = x_{4,\mathrm{r}}$.

For the two-faceted cup there is an analytic expression for every line segment $\partial S^j_{j,l}$ and $\partial T^j_{l,j}$ in Eq. (7.2.2) with $k \in \{1, \cdots, 4\}$. For instance, the rays on the boundaries $\partial S^1_{j,l}$ and $\partial T^1_{l,j}$ are parameterized in the $(x,\, z)$-plane by

$$\boldsymbol{r}_{j,l}(t) = \begin{pmatrix} x_{l,\ell} - x_{j,\ell} + t(x_{l,\mathrm{r}} - x_{l,\ell}) \\ z_{l,\ell} - z_{j,\ell} + t(z_{l,\mathrm{r}} - z_{l,\ell}) \end{pmatrix} \qquad 0 \le t \le 1\,. \tag{7.2.3}$$

These rays are located on a vertical line segment in S_j as only the p_j-coordinate changes and on a curved line in T_l as both the target position and direction vary. The analytic expressions for $\partial S^1_{j,l}$ and $\partial T^1_{l,j}$ are

$$\partial S^1_{j,l}(t) = \Big\{(q_j, p_j) = \Big(q_{j,\min}, |\boldsymbol{\nu}_j \times \hat{\boldsymbol{r}}_{j,l}(t)|\Big), \Big\} \tag{7.2.4}$$

$$\partial T^1_{l,j}(t) = \Big\{(q_l, p_l) = \Big(q_{l,\max} - q_{j,\min} + t(q_{l,\max} - q_{l,\min}), |\boldsymbol{\nu}_l \times \hat{\boldsymbol{r}}_{j,l}(t)|\Big)\Big\}\,, \tag{7.2.5}$$

where we have indicated with $\hat{\boldsymbol{r}}_{j,l}(t)$ the normalization of the ray in Eq. (7.2.3) and, $\boldsymbol{\nu}_j$ and $\boldsymbol{\nu}_l$ are the normalized inward normals to lines j and l, respectively. Note that, $\sin\tau_j = |\nu_j \times \hat{\boldsymbol{r}}_{j,l}(t)|$ and $\sin\tau_l = |\nu_l \times \hat{\boldsymbol{r}}_{j,l}(t)|$. Likewise, the boundaries $\partial S^k_{j,l}$ and $\partial T^k_{l,j}$ are calculated for every $k \in \{2, 3, 4\}$ and $\partial S_{j,l}$ and $\partial T_{l,j}$ are found using Eq. (7.2.2).

In Figs. 7.4 – 7.9, $(\partial S_{j,k})_{j\neq k=2,3,4}$ and $(\partial T_{j,l})_{j\neq l=1,2,3}$ are depicted in blue and red, respectively. The source and target PS of lines 2 and 3 have some empty regions. These parts correspond to the regions formed by the rays that either go back to the source or are emitted from the target. These regions are not taken into account, see Eq. (7.2.2). We observe that, because of the symmetry of the optical system, S_3 is the mirror image of S_2 after reflection in the central point $(q, p) = (-9.5, 0)$ and translation from $(q, p) \to (q + 19, p)$. Likewise T_3 is the mirror image of S_2 after the same reflection and translation.

7.2.1 The structure of the algorithm

In this section we explain how to compute the target photometric variables in PS. In the following, to simplify the notation, we indicate the target coordinates of the rays on T_4 with $(q,\, p)$ instead of $(q_{\mathrm{t},4}, p_{\mathrm{t},4})$. The intensity I along a given direction

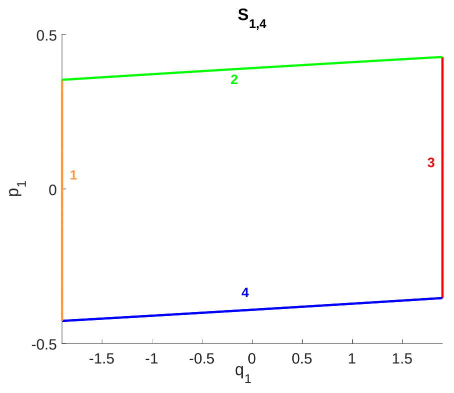

Figure 7.2: Source phase space of line 1. Boundary of the region $S_{1,4}$.

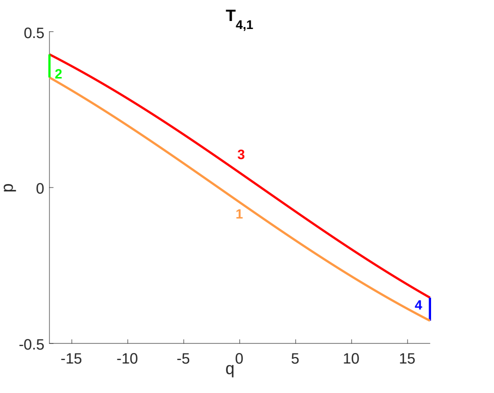

Figure 7.3: Target phase space of line 4. Boundary of the region $T_{4,1}$.

$p \in [-1, 1]$ in target phase space T_4 is a function of the luminance $L(q, p)$ defined as in Equation (4.3.3). For the two-faceted cup, it becomes:

$$I_{\mathrm{PS}}(p) = \int_{-b}^{b} L(q, p)\mathrm{d}q. \tag{7.2.6}$$

The parts of T_4 that are illuminated by S_1 correspond to parts with positive luminance, for the other parts the luminance is equal to zero. Assuming positive luminance on S, the following relations hold:

$$L(q, p) > 0 \qquad \forall (q, p) \in T_{4,1}, \tag{7.2.7a}$$

$$L(q, p) \geq 0 \qquad \forall (q, p) \in (T_{4,j})_{j=2,3}. \tag{7.2.7b}$$

Once a ray leaves the source S it can hit the reflectors several times before hitting the target T. To relate S and T, a map $\mathrm{M}_{1,4}$: $S_1 \rightarrow T_4$ is introduced such that $\mathrm{M}_{1,4}(q_{\mathrm{s},1}, p_{\mathrm{s},1}) = (q, p)$. As not all parts of T_4 are illuminated by the source S, the map $\mathrm{M}_{1,4}$ is not surjective. Therefore, we need to determine the subsets of T_4 illuminated by S corresponding to the regions where the luminance is positive. To this purpose, we consider two different kinds of maps. The first map relates the coordinates of the source and the target PS of two *different* lines, we call it the propagation map. The second map relates the coordinates of the target and the source PS of the *same* line, we call it the reflection map. In particular, given two lines j and k with $j \neq k$, the propagation map $\mathrm{P}_{j,k} : S_{j,k} \mapsto T_{k,j}$ relates $S_{j,k}$ with $T_{k,j}$ and, it is defined as follows:

$$\mathrm{P}_{j,k}(q_{\mathrm{s},j}, p_{\mathrm{s},j}) = (q_{\mathrm{t},k}, p_{\mathrm{t},k}), \tag{7.2.8}$$

where $q_{\mathrm{t},k}$ is given by the x-coordinate of the intersection point between the ray and line k, and $p_{\mathrm{t},k}$ is computed considering the direction of the incident ray with respect to the normal of line k. For one single line k, the reflection map $\mathrm{R}_{k,l,h}$: $T_{k,l} \mapsto S_{k,h}$ relates the regions $T_{k,l} \subset T_k$ and $S_{k,h} \subset S_k$. To simplify the notation, from now on we omit the dependence of $\mathrm{R}_{k,l,h}$ from l and h, i.e. $\mathrm{R}_{k,l,h} = \mathrm{R}_k$. The reflection map is defined as follows:

$$\mathrm{R}_k(q_{\mathrm{t},k}, p_{\mathrm{t},k}) = (q_{\mathrm{s},k}, p_{\mathrm{s},k}), \tag{7.2.9}$$

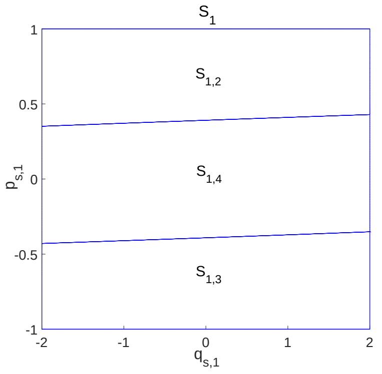

Figure 7.4: The PS S_1 of line 1 is partitioned into regions $(S_{1,k})_{k=2,3,4}$ formed by rays that leave line 1 and hit line k.

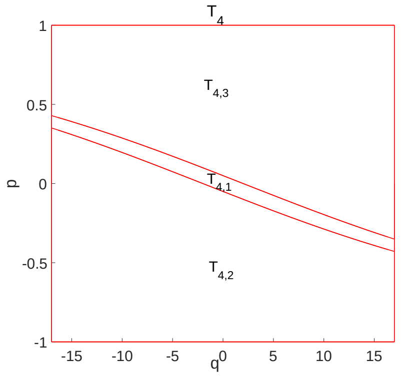

Figure 7.5: The PS T_4 of line 4 is partitioned into regions $(T_{4,l})_{l=1,2,3}$ formed by rays that leave line l and hit line 4.

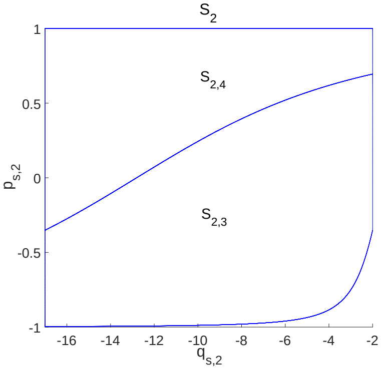

Figure 7.6: The PS S_2 of line 2 is partitioned into regions $(S_{2,k})_{k=3,4}$ formed by rays that leave line 2 and hit line k.

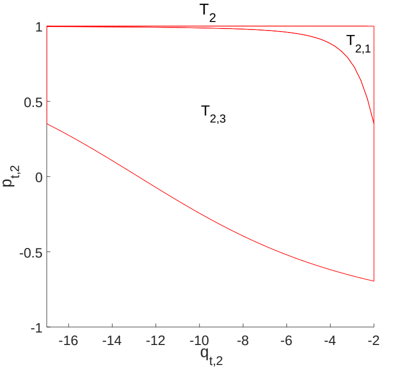

Figure 7.7: The PS T_2 of line 2 is partitioned into regions $(T_{2,l})_{l=1,3}$ formed by rays that leave line l and hit line 2.

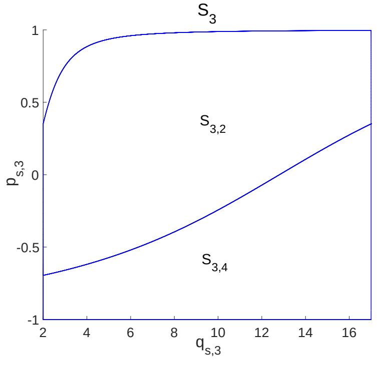

Figure 7.8: The PS S_3 of line 3 is partitioned into regions $(S_{3,k})_{k=2,4}$ formed by rays that leave line 3 and hit line k.

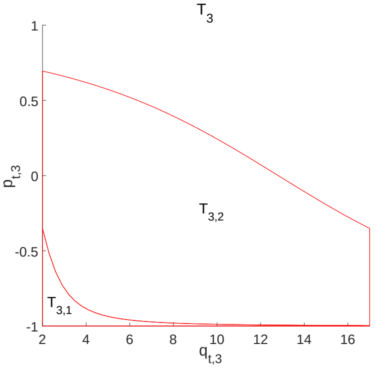

Figure 7.9: The PS T_3 of line 3 is partitioned into regions $(T_{3,l})_{l=1,2}$ formed by rays that leave line l and hit line 3.

where $p_{\mathrm{t},k}$ changes according to the reflection law and $q_{\mathrm{t},k} = q_{\mathrm{s},k}$ as R_k maps the target PS into the source PS of the same line k. Using a procedure similar to the ray transport matrices approach (see [9], Chapter 6), the map $\mathrm{M}_{1,4}$ is described by the composition of mappings $\mathrm{P}_{j,k}$ and R_k defined in Eqs. (7.2.8) and (7.2.9), respectively. This composition depends on the path Π followed by the rays where we refer to a path as the sequence of lines that a ray hits during its propagation from S to T. We indicate with $\mathrm{M}_{1,4}(\Pi)$ the map $\mathrm{M}_{1,4}$ restricted to path Π and with $R(\Pi) \subset T_4$ the regions on T_4 formed by the rays that follow path Π. Considering all the possible paths Π from S to T, all the regions $R(\Pi)$ with positive luminance on T_4 can be determined.

To clarify this concept, we provide the following example. Consider a ray that is emitted from the source (line 1), first hits the left reflector (line 2) and finally reaches the target (line 4). The path Π followed by this ray is defined as $\Pi = (1, 2, 4)$ and the corresponding map $\mathrm{M}_{1,4}(\Pi) : S_1 \mapsto R(\Pi)$ that describes the propagation of all rays that follow the path Π is defined by:

$$\mathrm{M}_{1,4}(\Pi) : S_{1,2} \mapsto T_{2,1} \mapsto S_{2,4} \mapsto T_{4,2}, \tag{7.2.10}$$

which can be written as:

$$\mathrm{M}_{1,4}(\Pi) = \mathrm{P}_{2,4} \circ \mathrm{R}_2 \circ \mathrm{P}_{1,2}\,. \tag{7.2.11}$$

In general, to construct the map $\mathrm{M}_{1,4}(\Pi)$ we need to know its corresponding path Π. To determine all possible paths Π, instead of tracing the rays from S to T, we start considering the rays in T_4. In particular, along a given direction $p \in [-1, 1]$ we consider the intersection points between the line $p = \text{const}$ and $(\partial T_{4,j})_{j=1,2,3}$. These points are traced back to line j from which they are emitted and their corresponding coordinates on S_j and T_j are computed. This is done applying sequentially the maps $\mathrm{P}_{j,4}^{-1} : T_{4,j} \mapsto S_{j,4}$ and $\mathrm{R}_j^{-1} : S_j \mapsto T_j$. Then the same procedure is repeated considering these new coordinates on T_j. The computation stops either when the points found are emitted from the source, that is when they are located on S_1, or when they reach again the target, that is when they are located on T_4. If a ray reaches S_1, then a path Π from S to T is found. If a ray reaches again the target T_4, then we conclude that it is not emitted by S and therefore, it is located inside the parts of T_4 with luminance equal to zero.

Finally, the inverse $\mathrm{M}_{1,4}^{-1}(\Pi)$ of the map $\mathrm{M}_{1,4}(\Pi)$ is constructed for every possible path Π. The map $\mathrm{M}_{1,4}^{-1}(\Pi)$ is the composition of the inverses of the propagation and the reflection maps in reverse order according to the path Π. For instance, for path $\Pi = (1, 2, 4)$, $\mathrm{M}_{1,4}^{-1}(\Pi)$ is given by:

$$\mathrm{M}_{1,4}^{-1}(\Pi) = \mathrm{P}_{1,2}^{-1} \circ \mathrm{R}_2^{-1} \circ \mathrm{P}_{2,4}^{-1}. \tag{7.2.12}$$

The steps of the procedure are shown in the graph in Fig. 7.10 where the map in Eq. (7.2.12) is written in red.

Using the procedure explained above, given a ray with coordinates $(q, p) \in T_4$ we can establish whether it is located inside one of the regions $R(\Pi)$ with positive luminance or not. In case the ray is inside a region $R(\Pi)$, its corresponding coordinates

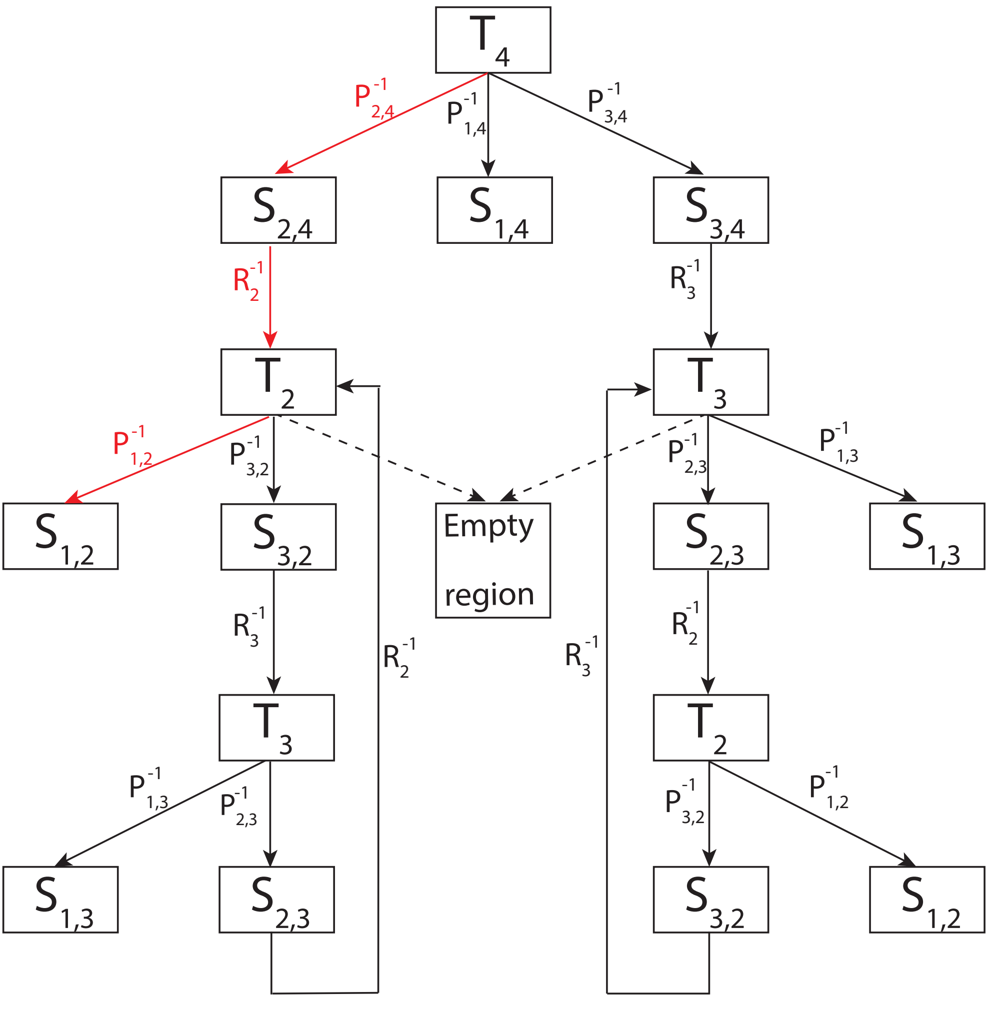

Figure 7.10: Tree that describes how to detect all the possible paths from S to T.

$(q_{\mathrm{s},1}, p_{\mathrm{s},1}) \in S_1$ are obtained using $\mathrm{M}_{1,4}^{-1}(\Pi)$, where Π is the path followed by this ray. The luminance in Equation (7.2.7) is, therefore, defined as in Equation (4.3.2), for some path Π connecting S and T. Assuming a Lambertian source and employing conservation of luminance along a ray (see [2], Chapter 16), we have that L is a positive constant inside $R(\Pi)$ and it has no contribution on the other parts of T_4. Indicating with $q^{\min}(\Pi, p)$ and $q^{\max}(\Pi, p)$ the minimum and maximum position coordinates of the intersection points between the boundaries $\partial R(\Pi)$ and line $p = \text{const}$, Eq. (7.2.6) reduces to Equation (4.3.4), if only two intersection points are found, and to Equation (5.2.8) in case more than two intersection points occur. For the two-faceted cup there are only two intersection points between line $p = const$ and $\partial R(\Pi)$, hence, in this chapter we use Equation (4.3.4) for the intensity calculation. We remark that, for a given ray with corresponding coordinates (q, p) on T_4, only one path is possible as we are assuming that all lines are reflective lines. Because of this, the regions $R(\Pi)$ do not overlap. where the intersection is over all the possible paths. Next, the details of the procedure to compute the coordinates $q^{\min}(\Pi, p)$ and $q^{\max}(\Pi, p)$ are explained.

The goal is to determine the intensity of the light that reaches the target with a given direction $p = \text{const}$. Since we assume a Lambertian source, this is equal to the sum of the lengths of the line segments given by the intersection of the line $p = \text{const}$ and the support of L (see Eq. (4.3.4)). To determine these line segments, a recursive procedure is developed. The procedure starts on T_4 with a given direction $p = \text{const}$. and with the parallel rays corresponding to the end points $(q^{\min}, p) = (-b, p)$ and $(q^{\max}, p) = (b, p)$. We set the initial intensity $I(p) = 0$ along direction $p = \text{const}$.. Considering the intersection between the line $p = \text{const}$ and the boundaries $(\partial T_{4,i})_{j=1,2,3}$ three intervals are found. Each interval corresponds to rays emitted by line i ($i = \{1, 2, 3\}$). The rays corresponding to the end points of these intervals are traced back from T_4 to T_j where j is the line from which the rays are emitted. Then, another interval of parallel rays along the corresponding direction in T_j has to be considered and the intersection points between the line $p = p_{\mathrm{t},j}$ and $\partial T_{j,k}$ (with $j \neq j, 4$) are calculated, where $p_{\mathrm{t},j}$ is the new direction of the rays traced back. The procedure continues recursively until the source is found.

Before explaining the details, let us introduce some notation. The role of the variables we introduce will become clear later on in this chapter. The coordinates in T_k of the rays traced back from line $j \neq k$ to line k are indicated with $(q^1_{\mathrm{t},k}, p_{\mathrm{t},k})$ and $(q^2_{\mathrm{t},k}, p_{\mathrm{t},k})$. The minimum and the maximum position coordinates are $q^{\min}_{\mathrm{t},k} = \min\{q^1_{\mathrm{t},k}, q^2_{\mathrm{t},k}\}$ and $q^{\max}_{\mathrm{t},k} = \max\{q^1_{\mathrm{t},k}, q^2_{\mathrm{t},k}\}$, respectively. The coordinates of the intersection points of $p = p_{\mathrm{t},k}$ with boundaries $\partial T_{k,j}$ need to be determined for every $j = \{1, 2, 3\}$ and $k = \{2, 3, 4\}$ with $k \neq j$. They are indicated with $(u^{\min}_{k,j}, p_{\mathrm{t},k})$ and $(u^{\max}_{k,j}, p_{\mathrm{t},k})$ where $u^{\min}_{k,j} < u^{\max}_{k,j}$. Since not all the rays whose corresponding coordinates are located inside the segment $[q^{\min}_{\mathrm{t},k}, q^{\max}_{\mathrm{t},k}]$ with direction $p = p_{\mathrm{t},k}$ follow the same path, the intersection segment $[v^{\min}_{k,j}, v^{\max}_{k,j}] = [q^{\min}_{\mathrm{t},k}, q^{\max}_{\mathrm{t},k}] \cap [u^{\min}_{k,j}, u^{\max}_{k,j}]$ needs to be calculated. $(v^{\min}_{k,j}, p_{\mathrm{t},k})$ and $(v^{\max}_{k,j}, p_{\mathrm{t},k})$ are the coordinates of the rays that need to be traced back from line k to line j.

The method can be outlined as follows.

1. Calculate the intersection points $(u^{\min}_{4,j}, p)$ and $(u^{\max}_{4,j}, p)$ between line $p = \text{const}$. and $\partial T_{4,j}$ for every $j = \{1, 2, 3\}$, where $u^{\min}_{4,j} < u^{\max}_{4,j}$. This can be done analytically because the exact expression of the boundaries $\partial T_{4,k}$ is found as explained

in the previous paragraph.

2. Calculate the intersection segment

$$[v_{4,j}^{\min}, v_{4,j}^{\max}] = [u_{4,j}^{\min}, u_{4,j}^{\max}] \cap [q^{\min}, q^{\max}]$$

3. If $j = 1$, coordinates $(v_{4,1}^{\min}, p)$ and $(v_{4,1}^{\max}, p)$ equal the coordinates $(q^{\min}(\Pi, p), p)$ and $(q^{\max}(\Pi, p), p)$ of the rays located on the boundary $\partial R(\Pi)$ with $\Pi = (1, 4)$. All the parallel rays with direction coordinate p and q-position coordinate $u_{4,1}^{\min} \leq q \leq u_{4,1}^{\max}$ are emitted by the source and they directly hit the target.
Update the intensity using Eq. (4.3.4)

$$I(p) = I(p) + q^{\min}(\Pi, p) - q^{\max}(\Pi, p).$$

4. If $j \neq 1$, continue with the following steps

5. Trace back $(v_{4,j}^{\min}, p)$ and $(v_{4,j}^{\max}, p)$ from line 4 to line j to find their corresponding coordinates on T_j

$$(q_{\mathrm{t},j}^{1}, p_{\mathrm{t},j}) = \mathrm{R}_j^{-1} \circ \mathrm{P}_{j,4}^{-1}(v_{4,j}^{\min}, p)$$
$$(q_{\mathrm{t},j}^{2}, p_{\mathrm{t},j}) = \mathrm{R}_j^{-1} \circ \mathrm{P}_{j,4}^{-1}(u_{4,j}^{\max}, p)$$

6. Update the path $\Pi = (j, 4)$

7. Determine $q_{\mathrm{t},j}^{\min} = \min\{q_{\mathrm{t},j}^{1}, q_{\mathrm{t},j}^{2}\}$ and $q_{\mathrm{t},j}^{\max} = \max\{q_{\mathrm{t},j}^{1}, q_{\mathrm{t},j}^{2}\}$

8. Calculate the intersection points $(u_{j,k}^{\min}, p)$ and $(u_{j,k}^{\max}, p)$ between line $p_{\mathrm{t},j}$ and $\partial T_{j,k}$ for every $k = \{1, 2, 3\}$ with $k \neq j$.

9. Since not all rays whose corresponding coordinates are located inside the segment $[q_{\mathrm{t},j}^{\min}, q_{\mathrm{t},j}^{\max}]$ follow the same path, compute the intersection segment

$$[v_{j,k}^{\min}, v_{j,k}^{\max}] = [u_{j,k}^{\min}, u_{j,k}^{\max}] \cap [q_{\mathrm{t},j}^{\min}, q_{\mathrm{t},j}^{\max}].$$

10. For $k \neq 1$

    a) Trace back $(v_{j,k}^{\min}, p_{\mathrm{t},j})$ and $(v_{j,k}^{\max}, p_{\mathrm{t},j})$ from j to k

    $$(q_{\mathrm{t},k}^{1}, p_{\mathrm{t},k}) = \mathrm{R}_k^{-1} \circ \mathrm{P}_{k,j}^{-1}(v_{j,k}^{\min}, p_{\mathrm{t},j}),$$
    $$(q_{\mathrm{t},k}^{2}, p_{\mathrm{t},k}) = \mathrm{R}_k^{-1} \circ \mathrm{P}_{k,j}^{-1}(v_{j,k}^{\max}, p_{\mathrm{t},j}).$$

    b) Update the path $\Pi = (k, \Pi)$

    c) Put $j = k$ and repeat the procedure from point 7.

11. If $k = 1$, the rays reached the source and a possible path $\Pi = (1, \cdots, 4)$ is found.

    a) Apply

    $$(q_{\mathrm{s},1}^{1}, p_{\mathrm{s},1}) = \mathrm{P}_{1,j}^{-1}(v_{j,1}^{\min}, p_{\mathrm{t},j})$$
    $$(q_{\mathrm{s},1}^{2}, p_{\mathrm{s},1}) = \mathrm{P}_{1,j}^{-1}(v_{j,1}^{\max}, p_{\mathrm{t},j})$$

b) Apply the direct map $\mathrm{M}_{1,4}(\Pi)$ restricted to the path Π found:

$$(q^1(\Pi,p),p) = \mathrm{M}_{1,4}(\Pi)(q^1_{\mathrm{s},1}, p_{\mathrm{s},1})$$
$$(q^2(\Pi,p),p) = \mathrm{M}_{1,4}(\Pi)(q^2_{\mathrm{s},1}, p_{\mathrm{s},1})$$

c) Update intensity

$$I(p) = I(p) + q^{\min}(\Pi,p) - q^{\max}(\Pi,p)$$

where $q^{\min} = \min\{q^1(\Pi,p), q^2(\Pi,p)\}$ and $q^{\max} = \max\{q^1(\Pi,p), q^2(\Pi,p)\}$.

To clarify the technique, we make an example that describes how the target intensity along direction $p = -0.2$ is calculated. From Fig. 7.11 to Fig. 7.18 the steps used in this example are shown. A detailed description of those figures is given in the following.

The procedure starts with the rays with direction $p = 0.2$ on T_4, where $q^{\min} = -b$ and $q^{\max} = b$ are the left and the right end points of the target T, respectively. The intersection points $(u^{\min}_{4,j}, p)$ and $(u^{\max}_{4,j}, p)$ of the line $p = -0.2$ with boundaries $\partial T_{4,j}$ are computed for every $j \neq 4$.

We start from $j = 1$. Therefore the coordinates $(u^{\min}_{4,1}, p)$ and $(u^{\max}_{4,1}, p)$ of the intersection points between line $p = -0.2$ and the boundary $\partial T_{4,1}$ are computed and these points are depicted in Fig. 7.11. The source is now reached because $j = 1$ and, one possible path is found. The points $(u^{\min}_{4,1}, p)$ and $(u^{\max}_{4,1}, p)$ are located on the boundaries of the region formed by the rays that leave the source and directly hit the target, that is the rays located on $\partial R(\Pi_1)$ with $\Pi_1 = (1,4)$. Therefore, the contribution to the intensity formed by the rays that follow the path $\Pi_1 = (1,4)$ is given by $u^{\max}_{4,1} - u^{\min}_{4,1}$.

We continue with $j = 2$. The boundary $\partial T_{4,2}$ is considered in order to find other paths. The intersection points $(u^{\min}_{4,2}, p)$ and $(u^{\max}_{4,2}, p)$ of line $p = -0.2$ with the boundary $\partial T_{4,2}$ are calculated. They are depicted in Fig. 7.12 with the magenta dots. also the intersection segment

$$[v^{\min}_{4,2}, v^{\max}_{4,2}] = [u^{\min}_{4,2}, u^{\max}_{4,2}] \cap [q^{\min}, q^{\max}] \tag{7.2.13}$$

is calculated[1]. Their corresponding position coordinates $q^1_{\mathrm{s},2}$ and $q^2_{\mathrm{s},2}$ on S_2 are obtained from:

$$\begin{aligned} \mathrm{P}^{-1}_{2,4}(v^{\min}_{4,2}, p) &= (q^1_{\mathrm{s},2}, p_{\mathrm{s},2}), \\ \mathrm{P}^{-1}_{2,4}(v^{\max}_{4,2}, p) &= (q^2_{\mathrm{s},2}, p_{\mathrm{s},2}). \end{aligned} \tag{7.2.14}$$

The directions $p^{\min}_{\mathrm{s},2}$ and $p^{\max}_{\mathrm{s},2}$ on S_2 are given considering the direction $p_{\mathrm{t},2} = p$ with respect to the normal $\boldsymbol{\nu}_2$ of line 2. Note that $p^1_{\mathrm{s},2} = p^2_{\mathrm{s},2}$ because all the lines are straight, their normals do not depend on the position at which it is computed. Then, the corresponding direction $p^1_{\mathrm{t},2} = p^2_{\mathrm{t},2}$ on T_2 is calculated from:

$$\begin{aligned} \mathrm{R}^{-1}_{2}(q^1_{\mathrm{s},2}, p_{\mathrm{s},2}) &= (q^1_{\mathrm{t},2}, p_{\mathrm{t},2}), \\ \mathrm{R}^{-1}_{2}(q^2_{\mathrm{s},2}, p_{\mathrm{s},2}) &= (q^2_{\mathrm{t},2}, p_{\mathrm{t},2}). \end{aligned} \tag{7.2.15}$$

[1] In T_4 $v^{\min}_{4,2} = u^{\min}_{4,2}$ and $v^{\max}_{4,2} = u^{\max}_{4,2}$ because $q^{\min} = -b$ and $q^{\max} = b$ always coincide with the end points of T_4.

Note that $q^1_{\mathrm{s},2} = q^1_{\mathrm{t},2}$ and $q^2_{\mathrm{s},2} = q^2_{\mathrm{t},2}$ since the reflection map does not change the position coordinates. Eqs. (7.2.14) and (7.2.15) lead to:

$$\begin{aligned}\mathrm{R}_2^{-1} \circ \mathrm{P}_{2,4}^{-1}(v_{4,2}^{\min}, p) &= (q^1_{\mathrm{t},2}, p_{\mathrm{t},2}),\\ \mathrm{R}_2^{-1} \circ \mathrm{P}_{2,4}^{-1}(v_{24,}^{\max}, p) &= (q^2_{\mathrm{t},2}, p_{\mathrm{t},2}).\end{aligned} \tag{7.2.16}$$

The map $\mathrm{R}_2^{-1} \circ \mathrm{P}_{2,4}^{-1}$ is depicted in red in Fig. 7.10. The minimum $q^{\min}_{\mathrm{t},2} = \min\{q^1_{\mathrm{t},2}, q^2_{\mathrm{t},2}\}$ and the maximum $q^{\max}_{\mathrm{t},2} = \max\{q^1_{\mathrm{t},2}, q^2_{\mathrm{t},2}\}$ are calculated. The points with coordinates $(q^{\min}_{\mathrm{t},2}, p_{\mathrm{t},2})$ and $(q^{\max}_{\mathrm{t},2}, p_{\mathrm{t},2})$ are depicted in Fig. 7.13 where $p_{\mathrm{t},2} = 0.82$. To understand whether the corresponding rays are illuminated or not by the source, the preceding procedure used for T_4 is now applied to T_2 along direction $p_{\mathrm{t},2} = 0.82$.

Next, the intersection points $(u^{\min}_{2,j}, p_{\mathrm{t},2})$ and $(u^{\max}_{2,j}, p_{\mathrm{t},2})$ of line $p_{\mathrm{t},2} = 0.82$ with boundaries $\partial T_{2,j}$ are computed for every $j \in \{1, 3\}$. We start from the boundary $\partial T_{2,1}$ obtaining the points $(u^{\min}_{2,1}, p_{\mathrm{t},2})$ and $(u^{\max}_{2,1}, p_{\mathrm{t},2})$ shown in Fig. 7.13. Now, the position coordinates $v^{\min}_{2,1} = \max\{q^{\min}_{\mathrm{t},2}, u^{\min}_{2,1}\}$ and $v^{\max}_{2,1} = \min\{q^{\max}_{\mathrm{t},2}, u^{\max}_{2,1}\}$ need to be considered. All the rays located inside the segment $[v^{\min}_{2,1}, v^{\max}_{2,1}]$ in T_2 and with direction $p_{\mathrm{t},2}$ follow the path $\Pi_2 = (1, 2, 4)$. In particular, the rays corresponding to the coordinates $(v^{\min}_{2,1}, p_{\mathrm{t},2})$ and $(v^{\max}_{2,1}, p_{\mathrm{t},2})$ are located on the boundaries of the region $R(\Pi_2)$ on T_4 formed by all the rays that follow path Π_2. Their corresponding coordinates $(q^1(\Pi_2, p), p)$ and $(q^2(\Pi_2, p), p)$ on T_4 are obtained from:[2]

$$\begin{aligned}\mathrm{P}_{2,4} \circ \mathrm{R}_2(v^{\min}_{2,1}, p_{\mathrm{t},2}) &= (q^1, p),\\ \mathrm{P}_{2,4} \circ \mathrm{R}_2(v^{\max}_{2,1}, p_{\mathrm{t},2}) &= (q^2, p).\end{aligned} \tag{7.2.17}$$

The rays corresponding to the coordinates (q^1, p) and (q^1, p) are located on the boundary $\partial R(\Pi_2)$ along direction $p = -0.2$. Indicating with $q^{\min} = \min\{q^1, q^2\}$ and $q^{\max} = \max\{q^1, q^2\}$, the distance $q^{\max} - q^{\min}$ gives the contribution to the intensity $I(p)$ of the rays located in $R(\Pi_2)$ where $p = -0.2$.

T_2 can also be illuminated by line 3, therefore the intersection points $(u^{\min}_{2,3}, p_{\mathrm{t},2})$ and $(u^{\max}_{2,3}, p_{\mathrm{t},2})$ of line $p_{\mathrm{t},2} = 0.82$ and $\partial T_{2,3}$ are calculated, these points are depicted in Fig. 7.14. The coordinates $(v^{\min}_{2,3}, p_{\mathrm{t},2})$ and $(v^{\max}_{2,3}, p_{\mathrm{t},2})$ are shown in the same figure. As the source is not reached yet ($j = 3$), the rays corresponding to $(v^{\min}_{2,3}, p_{\mathrm{t},2})$ and $(v^{\max}_{2,3}, p_{\mathrm{t},2})$ are followed back using the inverses of the propagation and the reflection maps. The coordinates on T_3 are shown in Fig. 7.15 with blue circles and they obtained from:

$$\begin{aligned}\mathrm{R}_3^{-1} \circ \mathrm{P}_{2,3(}^{-1} v^{\min}_{2,3}, p_{\mathrm{t},2}) &= (q^1_{\mathrm{t},3}, p_{\mathrm{t},3}),\\ \mathrm{R}_3^{-1} \circ \mathrm{P}_{2,3(}^{-1} v^{\max}_{2,3}, p_{\mathrm{t},2}) &= (q^2_{\mathrm{t},3}, p_{\mathrm{t},3}).\end{aligned} \tag{7.2.18}$$

The minimum and the maximum position coordinates are $q^{\min}_{\mathrm{t},3} = \min\{q^1_{\mathrm{t},3}, q^2_{\mathrm{t},3}\}$ and $q^{\max}_{\mathrm{t},3} = \max\{q^1_{\mathrm{t},3}, q^2_{\mathrm{t},3}\}$, respectively. We found that $v^{\max}_{3,2} \neq u^{\max}_{3,2}$ because $[q^{\min}_{\mathrm{t},3}, q^{\max}_{\mathrm{t},3}] \subset [u^{\min}_{3,2}, u^{\max}_{3,2}]$, this means that the rays with corresponding position coordinates inside the interval $[q^{\max}_{\mathrm{t},3}, u^{\max}_{3,2}]$ will follow a different path. The procedure continues recursively. It stops either when the rays encounter the source, i.e. when $j = 1$, or when no intersection points between the direction $p = p_{\mathrm{t},k}$ and the boundaries $\partial T_{k,j}$ are found

[2] With a slight abuse of notation we indicate $q^1(\Pi, p)$ with q^1 and $q^2(\Pi, p)$ with q^2.

for any $j = 1, 2, 3$ with $j \neq k$.

If the source is reached, then a valid path $\Pi = (1, 3, 2, 4)$ is found. Using the inverse of the propagation map, we compute

$$\begin{aligned} \mathrm{P}^{-1}_{1,3}(q^{\min}_{\mathrm{t},3}, p_{\mathrm{t},3}) &= (q^{1}_{\mathrm{s},1}, p_{\mathrm{s},1}), \\ \mathrm{P}^{-1}_{1,3}(q^{\max}_{\mathrm{t},3}, p_{\mathrm{t},3}) &= (q^{2}_{\mathrm{s},1}, p_{\mathrm{s},1}). \end{aligned} \tag{7.2.19}$$

The direct map $\mathrm{M}_{1,4}(\Pi){:}S_1 \mapsto R(\Pi)$ restricted to path $\Pi = (1, 3, 2, 4)$, i.e.

$$\mathrm{M}_{1,4} = \mathrm{P}_{2,4} \circ \mathrm{R}_2 \circ \mathrm{P}_{3,2} \circ \mathrm{R}_3 \circ \mathrm{P}_{1,3} \tag{7.2.20}$$

is applied to the coordinates $(q^{1}_{\mathrm{s},1}, p_{\mathrm{s},1})$ and $(q^{1}_{\mathrm{s},1}, p_{\mathrm{s},1})$ giving:

$$\begin{aligned} \mathrm{M}_{1,4}(q^{1}_{\mathrm{s},1}, p_{\mathrm{s},1}) &= (q^{1}(\Pi, p), p), \\ \mathrm{M}_{1,4}(q^{2}_{\mathrm{s},1}, p_{\mathrm{s},1}) &= (q^{2}(\Pi, p), p). \end{aligned} \tag{7.2.21}$$

the coordinates $(q^{1}(\Pi, p), p)$ and $(q^{2}(\Pi, p), p)$ located on $\partial R(\Pi)$ in T_4 are found. Indicating with $q^{\min} = \min\{q^1, q^2\}$ and $q^{\max} = \max\{q^1, q^2\}$, Thus, the contribution to the intensity due to the rays that follow the path Π is given by

$$I(p) = I(p) + q^{\max}(\Pi, p) - q^{\min}(\Pi, p). \tag{7.2.22}$$

If no intersection points are found, then the rays traced are not emitted by the source, therefore no contribution to the intensity needs to be added. This is, for instance, the case of rays with coordinates $(v^{\min}_{2,3}, 0.82)$ and $(v^{\max}_{2,3}, 0.82)$ on T_2 in Fig. 7.14. Below we explain this case in detail.

In Fig. 7.15, the coordinates $(q^{\min}_{\mathrm{t},3}, p_{\mathrm{t},3})$ and $(q^{\max}_{\mathrm{t},3}, p_{\mathrm{t},3})$ in T_3 with $p_{\mathrm{t},3} = -0.29$ are shown. They are obtained from:

$$\begin{aligned} \mathrm{R}^{-1}_3 \circ \mathrm{P}^{-1}_{3,2}(v^{\min}_{2,3}, 0.82) &= (q^{1}_{\mathrm{t},3}, p_{\mathrm{t},3}), \\ \mathrm{R}^{-1}_3 \circ \mathrm{P}^{-1}_{3,2}(v^{\max}_{2,3}, 0.82) &= (q^{2}_{\mathrm{t},3}, p_{\mathrm{t},3}). \end{aligned} \tag{7.2.23}$$

From Fig. 7.15 we note that there are no intersection points of line $p_{\mathrm{t},3} = -0.29$ with $\partial T_{3,1}$. So, only the coordinates of the intersections $(u^{\min}_{3,2}, -0.29)$ and $(u^{\max}_{3,2}, -0.29)$ between line $p_{\mathrm{t},3} = -0.29$ and $\partial T_{3,2}$ are calculated. Next, the intersection interval

$$[v^{\min}_{3,2}, v^{\max}_{3,2}] = [u^{\min}_{3,2}, u^{\max}_{3,2}] \cap [q^{\min}_{\mathrm{t},3}, q^{\max}_{\mathrm{t},3}], \tag{7.2.24}$$

formed by parallel rays with direction $p_{\mathrm{t},3} = -0.29$, is considered. Using:

$$\begin{aligned} \mathrm{R}^{-1}_2 \circ \mathrm{P}^{-1}_{2,3}(v^{\min}_{3,2}, -0.29) &= (q^{\min}_{\mathrm{t},2}, p_{\mathrm{t},2}), \\ \mathrm{R}^{-1}_2 \circ \mathrm{P}^{-1}_{2,3}(v^{\max}_{3,2}, -0.29) &= (q^{\max}_{\mathrm{t},2}, p_{\mathrm{t},2}), \end{aligned} \tag{7.2.25}$$

the corresponding coordinates $(q^{\max}_{\mathrm{t},2}, p_{\mathrm{t},2})$ and $(q^{\min}_{\mathrm{t},2}, p_{\mathrm{t},2})$ on T_2 are found (Fig. 7.16) with $p_{\mathrm{t},2} = -0.41$. Now the procedure is repeated again for T_2 along the direction $p_{\mathrm{t},2} = -0.41$. No intersection points between line $p_{\mathrm{t},2} = -0.41$ and $\partial T_{2,1}$ occur. Only, the intersection points $(u^{\min}_{2,3}, p_{\mathrm{t},2})$ and $(u^{\max}_{2,3}, p_{\mathrm{t},2})$ of line $p_{\mathrm{t},2} = -0.41$ and $\partial T_{2,3}$ are found (see Fig. 7.16). The intersection segment

$$[v^{\min}_{2,3}, v^{\max}_{2,3}] = [q^{\min}_{\mathrm{t},2}, q^{\max}_{\mathrm{t},2}] \cap [q^{\min}_{\mathrm{t},2}, q^{\max}_{\mathrm{t},2}] \tag{7.2.26}$$

is calculated. The coordinates on T_3 corresponding to the end points of the intersection interval are found using:

$$\begin{aligned} \mathrm{R}_3^{-1} \circ \mathrm{P}_{3,2}^{-1}(v_{2,3}^{\min}, p_{\mathrm{t},2}) &= (q_{\mathrm{t},3}^{\min}, p_{\mathrm{t},3}), \\ \mathrm{R}_3^{-1} \circ \mathrm{P}_{3,2}^{-1}(v_{2,3}^{\max}, p_{\mathrm{t},2}) &= (q_{\mathrm{t},3}^{\max}, p_{\mathrm{t},3}), \end{aligned} \tag{7.2.27}$$

where $p_{\mathrm{t},3} = 0.91$ (see Fig. 7.17).

Considering the PS T_3 and the direction $p_{\mathrm{t},3} = 0.91$, we note that there are no intersection points between line $p_{\mathrm{t},3} = 0.91$ and both $\partial T_{3,1}$ and $\partial T_{3,2}$. Indeed, the whole segment $[q_{\mathrm{t},3}^{\min}, q_{\mathrm{t},3}^{\max}]$ is outside both $T_{3,2}$ and $T_{3,1}$. Because of this, all the rays with q-coordinates inside the interval $[q_{\mathrm{t},3}^{\min}, q_{\mathrm{t},3}^{\max}]$ and with direction $p = p_{t,3}$ are not illuminated by the source and no new real path is found.

Finally, the recursive procedure is applied to $T_{4,3}$. The first step is depicted in Fig. 7.18. We decided not to show all the steps for $T_{4,3}$ as they are similar to those used for $T_{4,2}$ and explained above.

Finally, to compute the intensity along another direction $p^l \in [-1, 1]$ on T_4, the procedure explained for $p = -0.2$ is repeated for $p = p^l$. In this way we find all the possible paths Π and the regions $R(\Pi)$ with positive luminance on T_4. Furthermore, considering every time the coordinates located on the boundaries of the regions $T_{j,k}$ for every k, also the boundaries $\partial R(\Pi)$ are determined for a given path Π as well as the coordinates $q^{\max}(\Pi, p)$ and $q^{\min}(\Pi, p)$ for every $p \in [-1, 1]$. In Algorithm 3 they are the main steps to calculate the intensity $I(p)$ along a given direction $p = p^l$ in T_4, where for the first step we take $k = 4$. In the next section we provide the numerical results for the two-faceted cup.

7.3 Results for the two-faceted cup

To demonstrate the accuracy of the method, a comparison with the ray tracing approach is provided. In particular, we compare our method with MC ray tracing. The MC intensity is computed tracing randomly a large number of rays from the source to the target of the system. Then, a partitioning $P : -1 = p^0 < \cdots < p^{\mathrm{Nb}} = 1$ of the interval $[-1, 1]$ is considered, where Nb indicates the number of bins in the partitioning. The MC intensity along the direction $p \in [p^h, p^{h+1}]$ is given by the ratio of the number of rays $\mathrm{Nr}[p^h, p^{h+1}]$ that arrive at the bin $[p^h, p^{h+1}]$ and the total number of rays $\mathrm{Nr}[-1, 1]$ that arrive at the target for every $p \in [p^h, p^{h+1}]$ as defined in Equation (5.3.4). Hence, the MC intensity is piecewise constant. Note that $\hat{I}_{\mathrm{MC}}$ is normalized. In order to compute the intensity distribution for all the directions, the partitioning P of the target is considered. Then, the procedure explained above is repeated for $\left(p^{h+1/2} = \frac{1}{2}(p^{h+1} + p^h)\right)_{h=0,\cdots,\mathrm{Nb}-1}$ and the MC intensity is calculated over every bin. The profile of the MC intensity is depicted in Fig. 7.20 with a blue line. There the intensity is calculated tracing 10^7 rays and taking $\mathrm{Nb} = 100$.

Next, we compute the intensity at the target employing the PS ray mapping method. Using the procedure explained in Section **??**, we are able to detect all the possible paths Π that a ray can follow during the propagation through the system. For the two-faceted cup 5 different paths are found. Given a path Π, the coordinates $(q^{\min}(\Pi, p^h), p^h)$ and $(q^{\max}(\Pi, p^h), p^h)$ of the rays located on $\partial R(\Pi)$ are determined

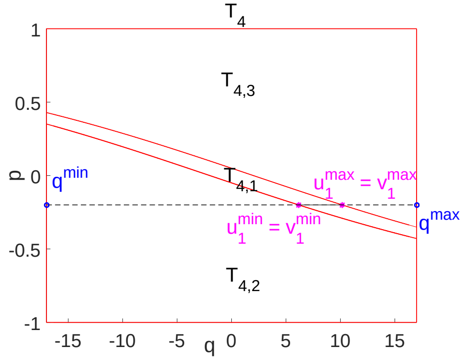

Figure 7.11: Target phase space of line 4. $q_{t,4}^{\min}$ and $q_{t,4}^{\max}$ are the x-coordinates of the end points of line 4. The intersection points between the line $p = -0.2$ and $\partial T_{4,1}$ are $(u_{4,1}^{\min}, p)$ and $(u_{4,1}^{\max}, p)$. $v_{4,1}^{\min} = \max\{q_{t,4}^{\min}, u_{4,1}^{\min}\}$ and $v_{4,1}^{\max} = \min\{q_{t,4}^{\max}, u_{4,1}^{\max}\}$.

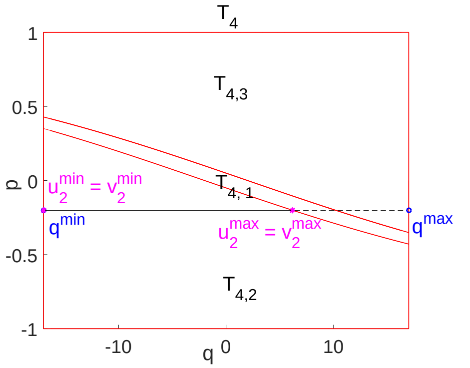

Figure 7.12: Target phase space of line 4. The intersection points between the line $p = -0.2$ and $\partial T_{4,2}$ are $(u_{4,2}^{\min}, p)$ and $(u_{4,2}^{\max}, p)$. $v_{4,2}^{\min} = \max\{q_{t,4}^{\min}, u_{4,2}^{\min}\}$ and $v_{4,2}^{\max} = \min\{q_{t,4}^{\max}, u_{4,2}^{\max}\}$.

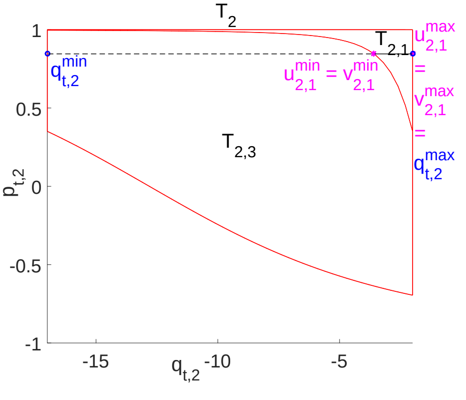

Figure 7.13: Target phase space of line 2. The coordinates of the intersection points between line $p_{t,2} = 0.82$ and $\partial T_{2,1}$ are $(u_{2,1}^{\min}, p_{t,2})$ and $(u_{2,1}^{\max}, p_{t,2})$. $v_{2,1}^{\min} = \max\{q_{t,2}^{\min}, u_{2,1}^{\min}\}$ and $v_{2,1}^{\max} = \min\{q_{t,2}^{\max}, u_{2,1}^{\max}\}$.

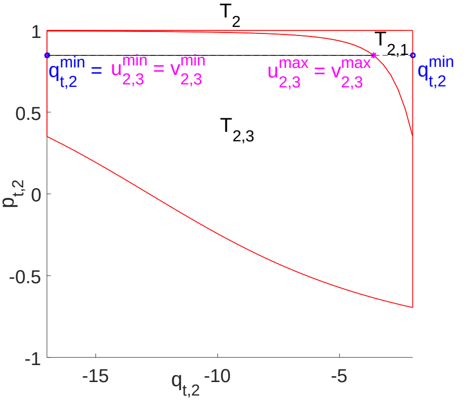

Figure 7.14: Target phase space of line 2. The coordinates of the intersection points between line $p_{t,2} = 0.82$ and $\partial T_{2,3}$ are $(u_{2,3}^{\min}, 0.82)$ and $(u_{2,3}^{\max}, 0.82)$. $v_{2,3}^{\min} = \max\{u_{2,3}^{\min}, q_{t,2}^{\min}\}$ and $v_{2,3}^{\max} = \min\{u_{2,3}^{\max}, q_{t,3}^{\max}\}$.

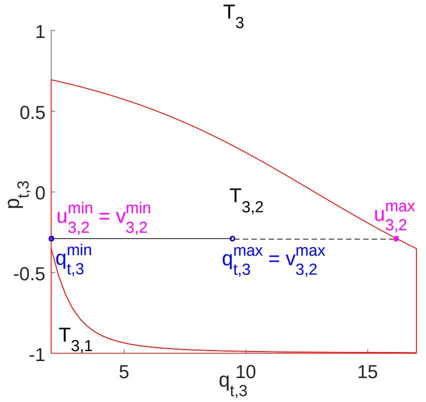

Figure 7.15: Target phase space of line 3. The position coordinates of the intersection points between line line $p_{\mathrm{t},3} = -0.29$ and $\partial T_{3,2}$ are $u_{3,2}^{\mathrm{min}}$ and $u_{3,2}^{\mathrm{max}}$. $v_{3,2}^{\mathrm{min}} = \max\{u_{3,2}^{\mathrm{min}}, q_{\mathrm{t},3}^{\mathrm{min}}\}$ and $v_{3,2}^{\mathrm{max}} = \min\{u_{3,2}^{\mathrm{max}}, q_{\mathrm{t},3}^{\mathrm{max}}\}$.

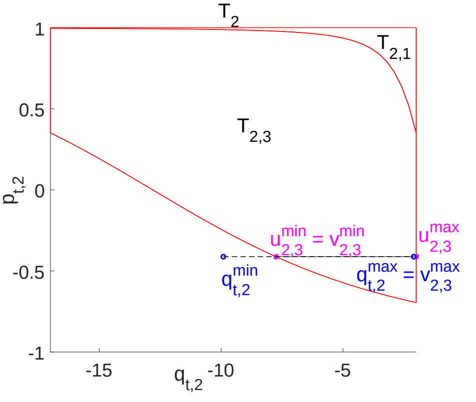

Figure 7.16: Target phase phase of line 2. The intersection points between line $p_{\mathrm{t}} = p_{\mathrm{t},2}$ and $\partial T_{2,3}$ are $(u_{2,3}^{\mathrm{min}}, p_{\mathrm{t},2})$ and $(u_{2,3}^{\mathrm{max}}, p_{\mathrm{t},2})$. $v_{2,3}^{\mathrm{min}} = \max\{u_{2,3}^{\mathrm{min}}, q_{\mathrm{t},2}^{\mathrm{min}}\}$ and $v_{2,3}^{\mathrm{max}} = \min\{u_{2,3}^{\mathrm{max}}, q_{\mathrm{t},2}^{\mathrm{max}}\}$.

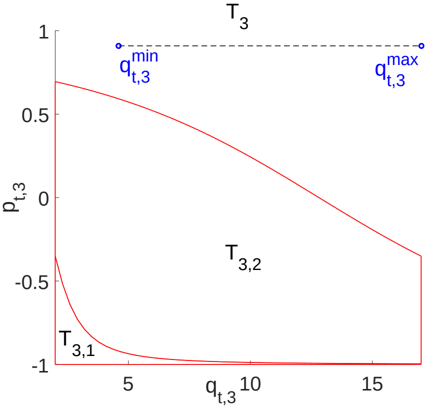

Figure 7.17: Target phase space of line 3. There are no intersection points of line $p_{3,2} = 0.91$ with the boundaries $\partial T_{3,2}$ and $\partial T_{3,1}$. The rays with coordinates inside the dotted segment hit again line 4 after some reflections and, therefore, are not emitted by the source.

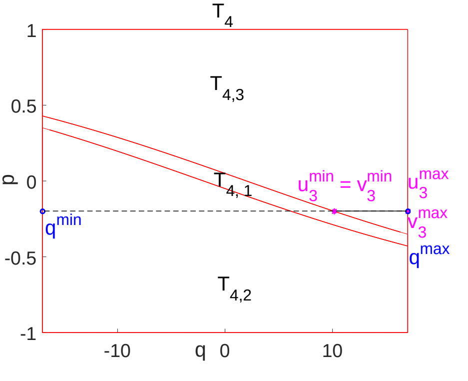

Figure 7.18: Target phase space of line 4. $q_{\mathrm{t},4}^{\mathrm{min}} = -b$ and $q_{\mathrm{t},4}^{\mathrm{max}} = b$. The intersection points between line $p = -0.2$ and $\partial T_{4,3}$ are $(u_{4,3}^{\mathrm{min}}, p)$ and $(u_{4,3}^{\mathrm{max}}, p)$. $v_{4,3}^{\mathrm{min}} = \max\{u_{4,3}^{\mathrm{min}}, q_{\mathrm{t},4}^{\mathrm{min}}\}$ and $v_{4,3}^{\mathrm{max}} = \min\{u_{4,3}^{\mathrm{max}}, q_{\mathrm{t},4}^{\mathrm{max}}\}$.

Algorithm 3 Recursive procedure for the intensity calculation

Initialize $k = 4,\ q^{\min}_{t,4} = q^{\min} = -b,\ q^{\max}_{t,4} = q^{\max} b,\ p_{t,\ 4} = p =$ constant, $\Pi = (4)$.

procedure INTENSITY COMPUTATION($k,\ q^{\min}_{t,k},\ q^{\max}_{t,k},\ p_{t,\ k},\ \Pi$)
    for $j = 1, 2, 3$ **do**
        if $j \neq k$ **then**
            Compute the intersection points $(u^{\min}_{j,i}, p_{t,k})$ and $(u^{\max}_{j,i}, p_{t,k})$
            $\Pi \leftarrow (j, \Pi)$
            Compute $[v^{\min}_{k,j}, v^{\max}_{k,j}] = [u^{\min}_{k,j}, u^{\max}_{k,j}] \cap [q^{\min}_{t,k}, q^{\min}_{t,k}]$
            if $(j \neq 1)$ & $(j \neq 4)$ **then**
                Apply

$$
\begin{aligned}
(q^{1}_{t,j}, p_{t,j}) &= \mathrm{R}_{j}^{-1} \circ \mathrm{P}_{j,k}^{-1}(v^{\min}_{j,i}, p_{t,k}) \\
(q^{2}_{t,j}, p_{t,j}) &= \mathrm{R}_{j}^{-1} \circ \mathrm{P}_{j,k}^{-1}(v^{\max}_{j,i}, p_{t,k})
\end{aligned}
$$

                Determine

$$
q^{\min}_{t,j} = \min\{q^{1}_{t,j}, q^{2}_{t,j}\} \text{ and } q^{\max}_{t,j} = \max\{q^{1}_{t,j}, q^{2}_{t,j}\}
$$

                return INTENSITY COMPUTATION($j,\ q^{\min}_{t,j},\ q^{\max}_{t,j},\ p_{t,\ j},\ \Pi$)
            else
                if j=1 **then**
                    if $k \neq 4$ **then**
                        Apply

$$
\begin{aligned}
(q^{1}_{s,1}, p_{s,1}) &= \mathrm{P}_{1,k}^{-1}(v^{\min}_{k,1}, p_{t,k}) \\
(q^{2}_{s,1}, p_{s,1}) &= \mathrm{P}_{1,k}^{-1}(v^{\max}_{k,1}, p_{t,k}) \\
(q^{1}(\Pi, p), p) &= \mathrm{M}_{1,4}(\Pi)(q^{1}_{s,1}, p_{s,1}) \\
(q^{2}(\Pi, p), p) &= \mathrm{M}_{1,4}(\Pi)(q^{2}_{s,1}, p_{s,1})
\end{aligned}
$$

                        Calculate

$$
\begin{aligned}
q^{\min}(\Pi, p) &= \min\{q^{1}, q^{2}\}, \\
q^{\max}(\Pi, p) &= \max\{q^{1}, q^{2}\},
\end{aligned}
$$

                        where $q^{1} := q^{1}(\Pi, p)$ and $q^{2} := q^{2}(\Pi, p)$.
                        return $I(p) = I(p) + q^{\min}(\Pi, p) - q^{\max}(\Pi, p)$.
                    else

$$
q^{\min}(\Pi, p) = v^{\min}_{4,k} \text{ and } q^{\max}(\Pi, p) = v^{\max}_{4,k}
$$

                        return $I(p) = I(p) + q^{\min}(\Pi, p) - q^{\max}(\Pi, p)$.
                    end if
                else
                    return $I(p)$
                end if
            end if
        end if
    end for
end procedure

figures/final_T.eps

Figure 7.19: Target phase space for the two-faceted cup divided into 100 bins. Five different paths are found. The rays with coordinates $(q^{\min}, p)$ and $(q^{\max}, p)$ in T_4 that are located at the boundaries $\partial R(\Pi)$ are depicted with dots, the color of the dots depends on the path Π followed by the rays. Using the ray mapping method, only these rays need to be traced from S to T for the intensity computation.

for every $p = (p^h)_{h=0,\cdots,\mathrm{Nb}}$ where the values p^h are given from the partitioning P used for MC ray tracing. These rays are depicted in Fig. 7.19, where all the rays that follow the same path are shown with the same color. The PS intensity is obtained from Eq. (4.3.4). Note from Fig. 7.19 that only 2Nb rays need to be traced through the system for the intensity computation. The averaged normalized PS intensity is given by Equation (5.3.3) where the integrals are calculated using the trapezoidal rule. The profile of the PS intensity is depicted in in Fig. 7.20 with the dotted green line.

For the two-faced cup, the intensity can be computed analytically. This intensity is taken as the reference intensity $\hat{I}_{\mathrm{ref}}$ and, it is depicted in Fig. 7.20 with a red line. The results in Fig. 7.20 show that all the intensity's profiles are all similar to each other. Therefore, we can claim that our method computes the intensity correctly.

In order to compare the speed of convergence of the two methods, we consider the error between the approximate intensities $\hat{I}_{\mathrm{A}}$ $(\mathrm{A} = \mathrm{MC}, \mathrm{PS})$ and the exact intensity $\hat{I}_{\mathrm{exact}} = \hat{I}_{\mathrm{ref}}$ from Equation (5.3.5) As the accuracy of the ray tracing method depends on the number of rays traced, the MC intensity is calculated for increasing numbers of rays traced through the system and, the error between the approximate intensity and the reference intensity is computed using Equation (5.3.5). In Fig. 7.21

the behavior of the MC error as a function of the CPU-time is depicted with the blue line. Increasing the number of rays the MC error decreases proportionally to the inverse of the square root of the number of rays traced. Next, the PS error is computed using Equation (5.3.5). It is depicted in Fig. 7.21 with the green dot. From the numerical results shown in Fig. 7.21 we can conclude that the PS ray mapping method is able to compute the output intensity of the two-faceted cup exactly. Also, it is much faster than the classical ray tracing approach when an error smaller than 10^{-4} is required.

Figure 7.20: Intensities for the two-faceted cup with three different approaches. The red line shows the exact intensity. The blue line depicts the intensity computed with MC raytracing with 10^7 rays. The dotted green line shows the intensity found with the new method.

7.4 Results for the multi-faceted cup

The method can be generalized to more complicated optical systems. In particular, it can be used for all systems formed by straight line segments. The goal of this section is to show the generalization of the method to the multi-faced cup which is a system with many left and right segments as reflectors. The design of this system is explained below.

A multi-faceted cup is an optical system formed by a source, a target and $\mathrm{Nl}-2$ reflectors, where Nl is the number of optical line segments that form the system. Defining a Cartesian coordinate system (x, z), the multi-faceted cup is symmetric with respect to the optical axis (z-axis). An example of this system is depicted in Fig. 7.22 where all the lines are labeled with numbers. The source $\mathsf{S} = [-a, a]$ (line 1) and the target $\mathsf{T} = [-b, b]$ (line 22) are two segments both perpendicular to the optical axis, figures/error_MC_PS.eps

Figure 7.21: Error between the approximated intensities and the reference intensity as a function of the CPU time (in seconds). The convergence of the ray tracing approach is depicted with the blue line. The error decreases increasing the number of rays traced. The green dot shows the error obtained with the PS method.

with $a = 2$ and $b = 17$. S is located at the height $z = 0$ while T has a height $z = 40$. Both sides of the system are divided into 10 segments which connect S with T. The 10 adjacent segments at the left of the system (lines $2, \cdots, 11$) connect the left extreme of the source with the left extreme of the target. Similarly, 10 adjacent segments at the right of the system (lines $12, \cdots, 21$) connect the right extreme of the source with the right extreme of the target. These segments are designed as follows. The intervals $[-b, -a]$ and $[a, b]$ are divided into 10 subintervals of the same length $(b - a)/10$. The x-coordinates of the end points of the line segments $12, \cdots, 21$ are equal to the x-coordinates of the subintervals of $[a, b]$, while the x-coordinates of the end points of the line segments $2, \cdots, 11$ are equal to the x-coordinates of the subintervals of $[-a, -b]$. The z-coordinates of every end point of the line segments $2, \cdots, 21$ are given substituting their x-coordinates into the equation of the parabola whose symmetric axis is equal to the z-axis and that passes through the points $(-17, 40)$ and $(17, 40)$. The 20-faceted cup is now well defined and can be seen as an approximation of a parabolic reflector. All the optical lines $j$with $j \in \{1, \cdots, 22\}$ are located in air, therefore the refractive index $n_j = 1$ for every j.

Similarly to the two-faceted cup, also for the multi-faceted cup we define the phase spaces of all the lines $j \in \{1, \cdots, \mathrm{Nl}\}$ as in Section **??**, for the 20-faceted cup $\mathrm{Nl} = 22$. Note that we always choose the index of the target equal to the index of the number

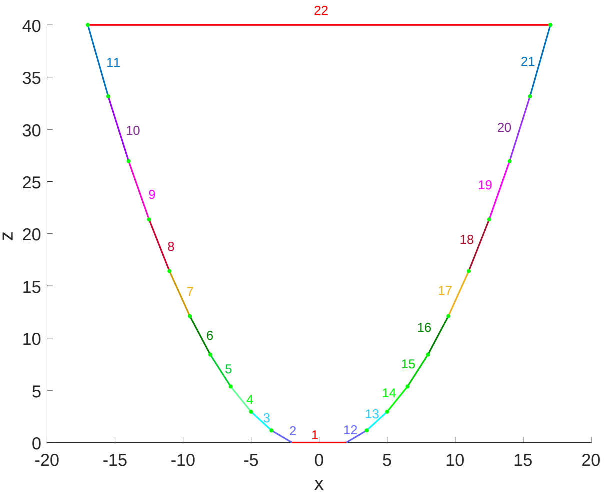

Figure 7.22: Shape of the 20-faceted cup. The system is formed by 22 different line segments: the source S, the target T, 10 left reflectors and 10 right reflectors. S $= [-2, 2]$ is located at $z = 0$. T $= [-17, 17]$ is parallel to the source and it is located at a height $z = 40$. The x-coordinates of the extremes of the reflectors are equidistributed. The z-coordinates are on a parabola that passes through the end points of the target and has as symmetry axis the z-axis. All the lines are located in air.

of lines that form the system Nl. For the system in Figure 7.22, 42 different phase spaces need to be considered. In general, for a system formed by Nl straight line segments, $2\mathrm{Nl}-2$ phase spaces are considered. For all the systems formed by straight line segments, the boundaries $(\partial S_{j,k})_{j\neq k=2,\cdots,\mathrm{Nl}}$ and $(\partial T_{j,l})_{j\neq l=1,\cdots,\mathrm{Nl}-1}$ of the regions that form every PS can be determined as explained in Section **??**.

The boundaries $(\partial T_{Nl,l})_{l=1,\cdots,\mathrm{Nl}-1}$ for the 20-faceted cup are depicted in Fig. 7.23 with red lines. All the possible paths that the rays can follow when propagating within the 20-faceted cup are determined using the same algorithm developed for the two-faceted cup and explained in Section **??**. As the number of optical lines increases, the number of possible paths increases as well. Therefore, we have to construct a more complicated tree than the one in Fig. 7.10. Despite this, the algorithm explained in the previous section still works fine and, also for the multi-faceted cup we are able to determine all the possible paths Π and all the regions $R(\Pi)$ with positive luminance at target PS T_{Nl}. Assuming a Lambertian source, only the rays located at the boundaries of these regions need to be computed. Therefore, for a given direction $p = \text{const}$ only the position coordinates $q^{\min}(\Pi, p)$ and $q^{\max}(\Pi, p)$ of the intersection points between the boundaries $\partial R(\Pi)$ and the line $p = const$ are needed for every possible path Π. Finally, the target intensity $I_{\mathrm{PS}}(p)$ along the direction p is obtained employing Eq. (**??**). Numerical results for a 20-faceted cup are given in the next section.

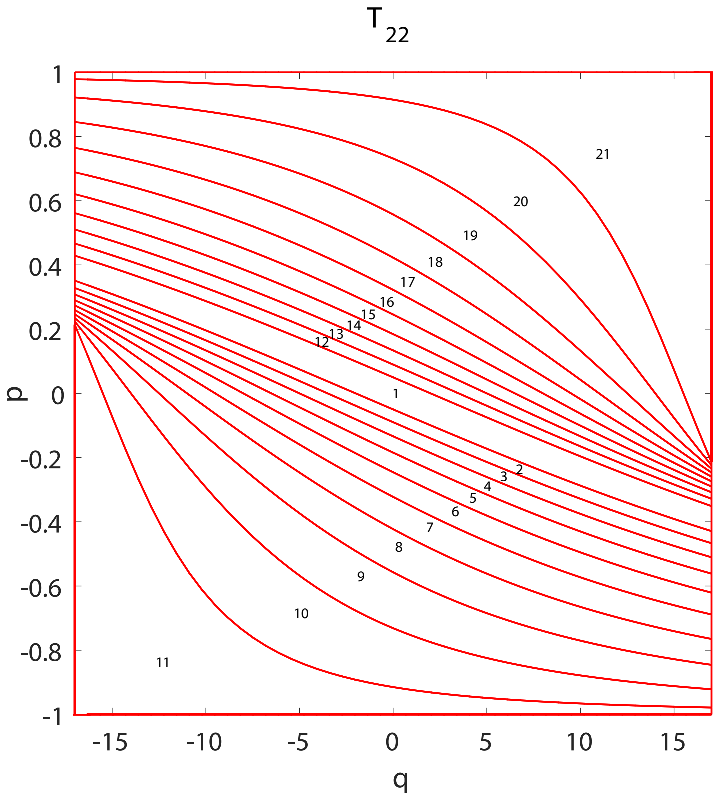

Figure 7.23: Target phase space of the 20-faceted cup. The red lines are the boundaries $(\partial T_{22,l})_{l=1,\cdots,21}$ which are determined analytically. The numbers inside the regions $T_{22,l}$ indicate the value of the index l.

7.5 Numerical results for the 20-faceted cup

In this section the results for the 20-faceted cup are presented. We compute the target intensity both with the inverse ray mapping method and MC ray tracing. The same partitioning P of the interval $[-1, 1]$ used for the two-faceted cup is considered. The normalized MC intensity and the normalized PS intensity $\hat{I}_{\mathrm{PS}}$ are computed. Their profiles are depicted in Fig. 7.24 with a blue line and a green dotted line, respectively. They are compared with a reference intensity $\hat{I}_{\mathrm{ref}}$ (red line) which is computed using MC ray tracing with 10^8 rays. Note that the intensity profile in Fig. 7.24 is more concentrated around the direction $p = 0$ than the intensity of the two-faceted cup (see Fig. 7.20). In particular, increasing the number of left and right reflectors the intensity profile becomes more and more peaked around the center approaching the profile of a parabolic reflector, (see [?]).

In order to show the performance of the new method, we calculate the error between the approximate intensities $\hat{I}_{\mathrm{A}}$ $(\mathrm{A} = \mathrm{MC}, \mathrm{PS})$ and the reference intensity $\hat{I}_{\mathrm{ref}}$ from Eq. (??). In Fig. 7.25 the speed of convergence for MC ray tracing is shown in blue. The better accuracy (the right most red point in Fig. 7.25) is obtained tracing figures/intensities10cup.eps

Figure 7.24: Intensity for the 20-faceted cup. The red line shows the reference intensity computed using MC ray tracing with 10^8 rays. The blue line depicts the MC intensity with 10^7 rays. The green and dotted line shows the intensity found with the ray mapping method.

figures/error_10cup1.eps

Figure 7.25: Error of the approximated intensities as a function of the CPU time. The convergence of MC ray tracing is depicted with the blue line. The PS error is shown with the green dots. The ray mapping method is more accurate than MC ray tracing and it is faster in case an error smaller than, say 10^{-4}, is desired.

10^8 rays. Also, the PS intensity is computed several times increasing every time the number of bins used in the trapezoidal rule to approximate the integrals in Eq. (**??**).

This has to be done in order to find the averaged PS intensity $\hat{I}_{\mathrm{PS}}$ over every bin. The error for the ray mapping method is calculated for all the approximated intensities. Increasing the number of bins in the trapezoidal rule, the PS error decreases. We remark that the PS method gives the value of the intensity pointwise, therefore we can compute the PS intensity without numeric integration. Nevertheless, we calculate the averaged intensity because we want to compare it with the MC intensity $\hat{I}_{\mathrm{MC}}$.

The error convergence is depicted in Fig. 7.25 with the red line. Since all the boundaries of the regions in PS are calculated exactly, the PS intensity is analytic. From Fig. 7.25 we observe that the minimum difference between the reference intensity and the approximated intensity found with the ray mapping method has an order of magnitude of 10^{-6}. This is due to the fact that for the 20-faceted cup the intensity cannot be computed exactly. Therefore, we took as reference intensity an intensity computed with MC ray tracing using $7.5 * 10^8$ rays which is not the exactly intensity. The error between the normalized exact intensity $\hat{I}_{\mathrm{exact}}$ and the normalized approximate intensity $\hat{I}_{\mathrm{A}}$ is given by:

$$\frac{1}{\mathrm{Nb}}\sum_{h=1}^{\mathrm{Nb}}|\hat{I}_{\mathrm{exact}}(p^h)-\hat{I}_{\mathrm{A}}(p^h)| \leq \frac{1}{\mathrm{Nb}}\left(\sum_{h=1}^{\mathrm{Nb}}\left|\hat{I}_{\mathrm{exact}}(p^h)-\hat{I}_{\mathrm{ref}}(p^h)\right|+\sum_{h=1}^{\mathrm{Nb}}\left|\hat{I}_{\mathrm{ref}}(p^h)-\hat{I}_{\mathrm{A}}(p^h)\right|\right). \tag{7.5.1}$$

Extrapolating the MC error we obtain an approximation of the difference between the reference solution (MC ray tracing with $7.5 * 10^8$ rays) and the exact intensity, this error is depicted in Fig. 7.25 with the cyan dot. From numerical symulation we obtain the difference between the extrapolated value and the exact intensity

$$\sum_{h=1}^{\mathrm{Nb}}|\hat{I}_{\mathrm{exact}}(p^h)-\hat{I}_{\mathrm{ref}}(p^h)|/\mathrm{Nb} \approx 1.68 * 10^{-6},$$

where $\mathrm{Nb} = 100$ The results show that

$$\sum_{h=1}^{\mathrm{Nb}}|\hat{I}_{\mathrm{exact}}(p^h)-\hat{I}_{\mathrm{ref}}(p^h)|/\mathrm{Nb} \approx \sum_{h=1}^{\mathrm{Nb}}|\hat{I}_{\mathrm{ref}}(p^h)-\hat{I}_{\mathrm{PS}}(p^h)|/\mathrm{Nb}.$$

Therefore, we claim that the error found with the inverse ray mapping method is also due to the MC error. We can conclude that the inverse ray mapping method performs very well also for more complicated systems. Compared to MC ray tracing the new method is not only faster but also much more accurate.

7.6 Discussions

In this chapter, we presented an inverse method to compute the intensity of light emitted by the source and received by the target of a given optical system. We tested our method for two-dimensional optical systems formed by straight line segments. The method employs the phase spaces of *all* the lines that form the system. All these phase spaces are related to each other through two different kinds of maps. A concatenation of these two maps gives a map that connects the coordinates of the rays at the source with those at the target. Employing the inverse of the concatenated map, all the possible paths that rays can follow during their propagation are found.

Only the rays located on the boundaries of the regions with positive luminance are traced, where every region is formed by rays that follow the same path during their propagation. Assuming constant luminance, only these rays are needed to calculate the output intensity.

We presented numerical results for a simple system: the two-faceted cup. We employ the PS of all the lines that form the system, each of them is divided into regions the boundaries of which are determined exactly. Numerical results show that the exactly output intensity is found. We compared our method with MC ray tracing showing significant advantages in terms of the accuracy and the computational time.

Then, we explained how the method can be extended to more complicated optical systems. We took as an example a system with 10 left and 10 right segments as reflectors, the so-called 20-faceted cup. Also for the generalized system, the boundaries of the regions that form every PS are determined exactly. This is true for all the systems formed by straight lines. This allows finding the analytic output intensity. To validate our method, the intensity found using the new technique is compared with the MC intensity. To demonstrate both the accuracy and speed advantages, numerical results are presented also for the 20-faceted cup.

Chapter 8

The extended ray mapping method

Chapter 9

Extended ray mapping method to systems with Fresnel reflection

Chapter 10

Discussion and conclusions

Appendix A

Implementation of Sobol' sequences

A.1 Van der Corput sequences

In the following we show a particular construction of a low-discrepancy sequence for $d = 1$ that was introduced the first time by Van der Corput in 1935. This kind of sequences, called *van der Corput* sequences, are particular interesting not only because they give an intuition of how to construct low discrepancy sequences but also because many other kind of sequences in higher dimensions are based on this one-dimensional case. Before introducing these sequences we need to give the concept of radical inverse function. Let $\mathrm{b} \geq 2$ be an integer base. Any natural number $n \in \mathbb{N}_0$ can be decomposed in base b as follows:

$$n = \sum_{i=0}^{\infty} d_i \mathrm{b}^i \tag{A.1.1}$$

where $d_i \in \{0, 1, \cdots, \mathrm{b} - 1\}$ are the digit numbers. The radical inverse function $\phi_\mathrm{b} : \mathbb{N}_0 \mapsto [0, 1)$ in base b is defined as:

$$\phi_\mathrm{b}(n) = \sum_{i=1}^{\infty} \frac{d_{i-1}}{\mathrm{b}^i}. \tag{A.1.2}$$

As an example we provide in the following the radical inverse function $\phi_\mathrm{b}(5)$ in base $\mathrm{b} = 2$. The digit expansion in base b of $n = 5$ is:

$$5 = 1 \cdot 2^0 + 1 \cdot 2^2. \tag{A.1.3}$$

Therefore, $d_0 = 1, d_1 = 0$ and $d_2 = 1$. The radical inverse function $\phi_2(5)$ is:

$$\phi_2(5) = \frac{1}{2} + \frac{1}{8} = \frac{5}{8}. \tag{A.1.4}$$

Definition A.1.1. The Van der Corput sequence in base b is defined as $\{\phi_\mathrm{b}(n)\}_{n\in\mathbb{N}_0}$.

For example, suppose we have the finite sequence of numbers $n \in \{0, 1, \cdots, 8\}$ the corresponding Van der Corput sequence $\{\phi_{\rm b}(n)\}_{n\in\{0,1,\cdots,8\}}$ in base $b = 2$ is:

$$\left\{\phi_2(n)\right\}_{n\in\{0,1,\cdots,8\}} = \left\{0, \frac{1}{2}, \frac{1}{4}, \frac{3}{4}, \frac{1}{8}, \frac{5}{8}, \frac{3}{8}, \frac{7}{8}, \frac{1}{16}\right\}. \tag{A.1.5}$$

It can be proved that the Van der Corput sequence in base b is uniformly distributed modulo one, [16]. The van der Corput sequence has been extended to higher dimensions. The most common QMC approach uses Sobol sequence which can be seen as an extended Van der Corput sequence in base $b = 2$. Sobol' sequence uses the same base $b = 2$ for all the dimensions $d \geq 2$.

A.2 Sobol' sequences

The aim is to generate a low-discrepancy sequence in the ipercube $[0, 1]^d$. Let us start from the simplest case of one dimension, i.e. $d = 1$. First, we need to chose a primitive polynomial P_j of degree s_j of the form

$$P_j : x^{\mathrm{s}_j} + a_{1,j}x^{\mathrm{s}_j-1} + \cdots + a_{\mathrm{s}_j-1}x + 1 \tag{A.2.1}$$

where the coefficients $\{a_{i,j}\}_{i=1,\cdots,\mathrm{s}_j-1}$ are either 0 or 1. Then a sequence $\{m_1, m_2, \cdots\}$ is defined such that:

$$m_{k,j} := 2a_{1,j}m_{k-1,j} \oplus 2^2a_{2,j}m_{k-2,j} \oplus \cdots \oplus 2^{\mathrm{s}-1}a_{k-1,j}m_{k-\mathrm{s}+1,j} \oplus 2^{\mathrm{s}}m_{k-1,j} \oplus m_{k-\mathrm{s},j}, \tag{A.2.2}$$

where we have indicated with $\oplus$ the bit by bit exclusive or operator which operates on two bit patterns and operates on each pair of the corresponding bins giving as result 1 if one of the two bits is 1 and 0 if both bits are equal either to 0 or 1. The values $m_{k,j}$, $1 \leq k \leq d$, are chosen such that they are odd and positive numbers less than 2^k. Now, the so-called direction numbers are defined by:

$$v_{k,j} = \frac{m_{k,j}}{2^k}. \tag{A.2.3}$$

Then, the sequence $\{x_{i,j}\}$ is given by

$$x_{i,j} = i_1v_1 \oplus i_2v_2 \oplus \cdots \tag{A.2.4}$$

for every i, where i_k is the k-th digit from the right when i is written in binary $i = (\cdots i_3i_2i_1)_2$, [54]. We provide in the following an example.

Given the primitive polynomial $x^3 + x^2 + 1$ of degree $\mathrm{s}_j = 3$, the first three coefficients $m_{1,j} = 1$, $m_{2,j} = 3$, and $m_{3,j} = 7$ lead to the following direction numbers

$$v_{1,j} = \frac{1}{2}, \qquad v_{2,j} = \frac{3}{4}, \qquad v_{3,j} = \frac{7}{8}, \tag{A.2.5}$$

that in binary notation are:

$$v_{1,j} = (0.1)_2 \qquad v_{1,j} = (0.11)_2, \qquad v_{1,j} = (0.111)_2. \tag{A.2.6}$$

From Eq. (A.2.2) we can derive the others coefficients $m_{4,j} = 5$, $m_{5,j} = 7$, etc. with he corresponding direction vectors:

$$v_{4,j} = \frac{5}{16} = (0.0101)_2 \qquad v_{5,j} = \frac{7}{32} = (0.00111)_2 \tag{A.2.7}$$

From Eq. (A.2.4) we finally find the sequence

$$\tag{A.2.8}$$

The generalization of Sobol's sequence to higher dimensions $d > 1$ is calculated considering a sequence where the i-th point has the form:

$$q_i = (x_{i,1}, x_{i,2} \cdots , x_{i,d}), \tag{A.2.9}$$

where the second index of the variables $x_{i,j}$ it refers to the polynomial P_j (with corresponding degree s$_j$) which is considered to calculate the direction numbers. Therefore, d different sets of direction numbers are generated from a given polynomial P_j using Eq. A.2.3 and each component $x_{i,j}$ is computed using the corresponding direction vector.

Appendix B

Calculation of the boundaries at the target PS

B.1 Analytical method to find the boundaries of the different regions in phase space

In this section, we present an analytical method to find the boundaries of the regions formed by rays that follow the same path. Furthermore, we will represent those regions on source and target phase space.

It is possible to determine the maximum number of times that a ray reflects into the two-faceted cup as follows. Rotating the entire cup we can think of the path as a straight line that hits one of the rotated targets. The idea to rotate the cup comes from the fact that in this way we consider the paths as straight lines, hence it is sufficient to find only one intersection point between the ray and one line segment (also in the case where we have more than one reflection) and finally rotate back the intersection point to find the point on the target. Next we want to explain this procedure in more detail. Our optical system is defined as in the previous section, see Figure 3.1. Let B be defined by:

$$\begin{aligned} B &= \left(h + \tfrac{a}{\tan(\gamma)}\right)\tfrac{1}{\cos(\gamma)} - \tfrac{a}{\tan(\gamma)} \\ &= \tfrac{h}{\cos(\gamma)} + a\tan\left(\tfrac{1}{2}\gamma\right), \end{aligned} \tag{B.1.1}$$

and $P : (0, B)$ is the rotation point. We define B_k as the clockwise ($k < 0$) or counterclockwise ($k \geq 0$) rotations of the point $P : (0, B)$ over an angle $\alpha_k = (2k+1)\gamma$, with γ the angle that the normal to the source forms with the reflectors of the cup and $k \in \mathbb{Z}$. The x and z-coordinates of B_k are indicated with $b_{k,x}$ and $b_{k,z}$, respectively, Figure $B.1$ is illustrative. The position vector for the points B_k is given by $\mathbf{b}_k = \begin{pmatrix} b_{k,x} \\ b_{k,z} \end{pmatrix}$ where

$$\mathbf{b}_k + \begin{pmatrix} 0 \\ \frac{a}{\tan(\gamma)} \end{pmatrix} = \begin{pmatrix} \cos(\alpha_k) & -\sin(\alpha_k) \\ \sin(\alpha_k) & \cos(\alpha_k) \end{pmatrix} \begin{pmatrix} 0 \\ B + \frac{a}{\tan(\gamma)} \end{pmatrix}. \tag{B.1.2}$$

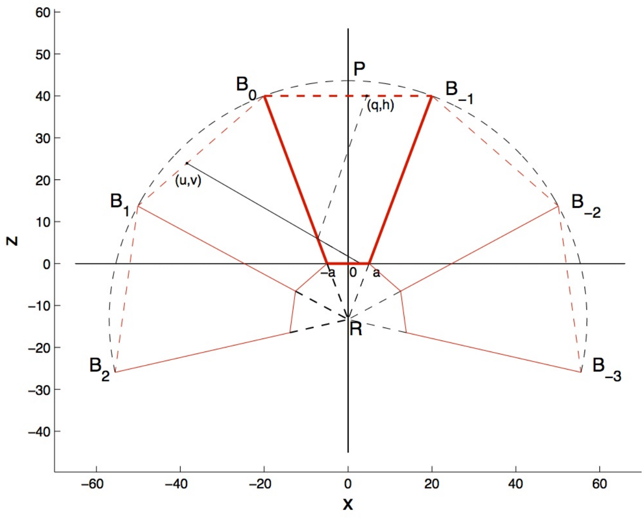

Figure B.1: The two-faceted cup rotated to both sides. The line segment $B_{k-1}B_k$ is the $|k|$ times rotated target. The point (u, v) of the intersection between a ray and the segment B_0B_1 corresponds to the point (q, h) on the target $B_{-1}B_0$. $P(0, B)$ is the point to rotate around the point $R = \left(0, -\frac{a}{\tan\gamma}\right)$. The length of the segments RB_k is equal to the radius of the dashed circle.

Then the maximum number of reflections r is:

$$r = \max\{k \in \mathbb{N} \mid b_{k-1,z} \geq 0\}. \tag{B.1.3}$$

This method of rotating the cup instead of reflecting the ray inside the system can also be applied to find the boundaries of the regions $M_{\mathrm{s},k}$ and $M_{\mathrm{t},k}$. In the following sections we will illustrate how this is done.

B.1.1 Source phase space

We observe that the set of rays that form the boundary of the regions $M_{\mathrm{s},k}$ only consists of rays that either leave the extremes of the source or hit one of the points B_k. In Figure B.1 is shown a ray that on the target phase space is located inside the region $M_{\mathrm{t},1}$, it does not constitute a point on any boundary. Furthermore, we note that the rays emitted from the corner points of the source form vertical lines in $\mathcal{P}_\mathrm{s}$, since $x = const$. On the other hand, rays that hit B_k form vertical lines in $\mathcal{P}_\mathrm{t}$, since $q = const$. Hence for the representation on the source phase space we have to choose rays that hit B_k, their directions are given by the relation

$$\tan t = \frac{x - b_{k,x}}{b_{k,z}}. \tag{B.1.4}$$

This is exactly what we did in the algorithm named *'Source'* (see Appendix **??** for details).

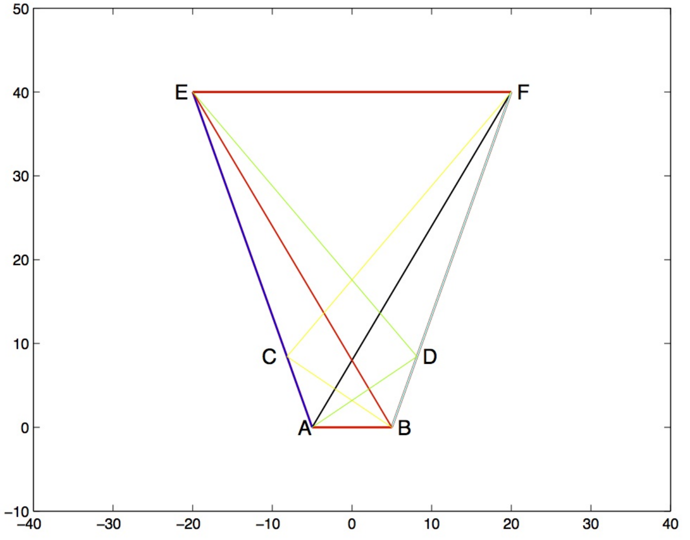

Figure B.2: Rays that leave the corner points of the source. The rays AF, BE, ACE, BDF are rays that do not hit the reflectors of the system. They constitute rays on the boundaries of the regions $M_{\mathrm{s},0}$, $M_{\mathrm{s},1}$ and $M_{\mathrm{s},-1}$. The rays ADE and BCF are rays that hit once the reflectors of the system. They constitute rays on the boundaries of the regions $M_{\mathrm{s},-1}$, $M_{\mathrm{s},-2}$, and $M_{\mathrm{s},1}$ or $M_{\mathrm{s},2}$, respectively.

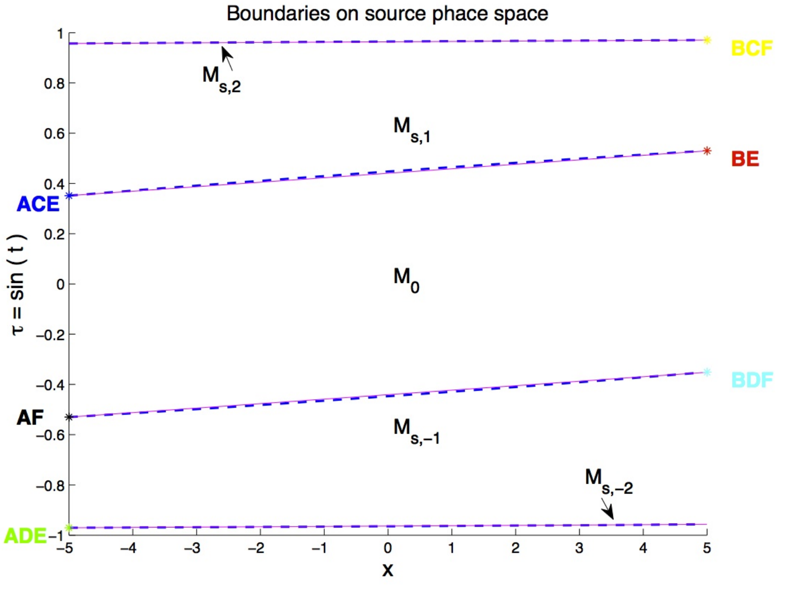

Figure B.3: Regions $M_{s,k}$ of rays that reflect $|k|$ times, with $(x, \tau) \in \mathcal{P}_{\mathrm{s}}$. The parameter values are: $a = 5$, $b = 20$ and $h = 40$. The continuous lines are the boundaries of the regions M_{s} calculated considering rays that leave the source and hit the points B_k at the target. The dashed blue lines are the boundaries calculated using $(B.1.4)$

In Figure $B.2$ are shown some rays that compose the boundaries of $M_{\mathrm{s},k}$ which coordinates are:

$$ADE = \left(-a, \arctan\left(\tfrac{-a+b_{-1,x}}{b_{-1,z}}\right)\right),\ ACE = \big(-a, \sin(\gamma)\big),\ AF = \big(-a, -\sin(\delta)\big),$$
$$BCF = \left(a, \arctan\left(\tfrac{a-b_{1,x}}{b_{1,z}}\right)\right), BDF = \big(a, -\sin(\gamma)\big) \text{ and } BE = \big(a, \sin(\delta)\big).$$

The rays are represented by points in phase space. So we choose a proper number of rays that leave the source to obtain an accurate representation of the boundaries of $M_{\mathrm{s},k}$ regions. The final result is shown in Figure $B.3$. In addition, we derive the exact equation for the map $\mathcal{M}$. From equation $(B.1.4)$ we find the value of the angle for each ray at the source (depending on the ray position). Thus the boundaries are simply straight lines in the $(x, \tan(t))$-plane. The subdivision of phase space into regions is shown in Figure $B.3$, where we can also see the comparison between the two different methods to calculate the boundaries. Note that in this specific case the boundaries appear straight lines also in the $(x, sin(t))$-plane.

B.1.2 Target phase space

In this section we derive an exact expression for the map $\mathcal{M}$ in such a way that it is possible to determine the boundaries of the regions $M_{\mathrm{t},k}$ simply by finding the images of some points on $\partial M_{\mathrm{s},k}$. Given a ray parameterization we are able to calculate the intersections point (u, v) between the ray and the line segment $B_{k-1}B_k$ as we did in *'Target'* (See Appendix **??** for the procedure). The corresponding point (q, h) on the target can be found by rotating or reflecting the point (u, v) back for k even or odd, respectively. Therefore we have the following expression for the point (q, h) on the target:

$$\begin{pmatrix} q \\ h \end{pmatrix} = \begin{pmatrix} (-1)^k & 0 \\ 0 & 1 \end{pmatrix} \begin{pmatrix} \cos(-2k\gamma) & -\sin(-2k\gamma) \\ \sin(-2k\gamma) & \cos(-2k\gamma) \end{pmatrix} \begin{pmatrix} u \\ v + \frac{a}{\tan(\gamma)} \end{pmatrix} - \begin{pmatrix} 0 \\ \frac{a}{\tan(\gamma)} \end{pmatrix}. \tag{B.1.5}$$

We observe that the sign depends on the parity of k. When $k = 0$, i.e. the ray does not reflect, the first and the second matrices become the identity matrix and the cup is not rotated nor reflected. When k is even, the determinant of the product between the first and the second matrixes at the right hand of equation $(B.1.5)$ is equal to 1 and we obtained a rotation matrix, while when k is odd the determinant of the matrix given by the product between the first and the second matrix is equal to -1 and we have a reflection matrix. Also the angle on the target is calculated. It is an addition of an angle and a change of sign depending on k:

$$\theta = (-1)^k(t - 2k\gamma). \tag{B.1.6}$$

For every k, the mapping $(x, t) \mapsto (q, \theta)$ is now well determined and also the regions $M_{\mathrm{s},k}$ of rays that reflect k times are mapped to $M_{\mathrm{t},k}$. We observe that the lines shown if Figure $B.3$ are mapped to vertical lines in target phase space by the map $\mathcal{M}$ (see Figure B.4). Hence, to obtain the boundaries of the target,we will choose rays that are emitted from points close to the boundary of the source. According to what we said so far, the case of the target requires some good calculation to determine where a ray exits the cup. We can obtain those points analytically for a suitable number of rays, as we did in *'Target'*, and then we can drawn those points on the phase space as is shown in Figure $B.4$.
The coordinates of the rays traced in Figure $B.2$ at the target are given by:

$$\begin{gathered} ADE = \big(-b, -(t_1 + 2\gamma))\big),\ ACE = \big(-b, \sin(\gamma)\big),\ AF = \big(-b, -\sin(\delta)\big), \\ BCF = \big(b, -(t_2 - 2\gamma)\big), BDF = \big(b, -\sin(\gamma)\big) \text{ and } BE = \big(b, \sin(\delta)\big). \end{gathered}$$

where $t_1 = \arctan(\frac{(}{-}a + b_{-1,x}b_{-1}))$ and $t_2 = \arctan(\frac{(}{a} - b_{-1,x}b_{-1}))$.

Figure $B.3$ and $B.4$ show also the symmetry of the regions $M_{\mathrm{s},k}$ and $M_{\mathrm{t},k}$. Finally we note that, since $k = 1$ is odd, the position of the regions $M_{\mathrm{t},1}$ and $M_{\mathrm{t},-1}$ are exchanged with respect to the position of $M_{\mathrm{s},1}$ and $M_{\mathrm{s},-1}$.

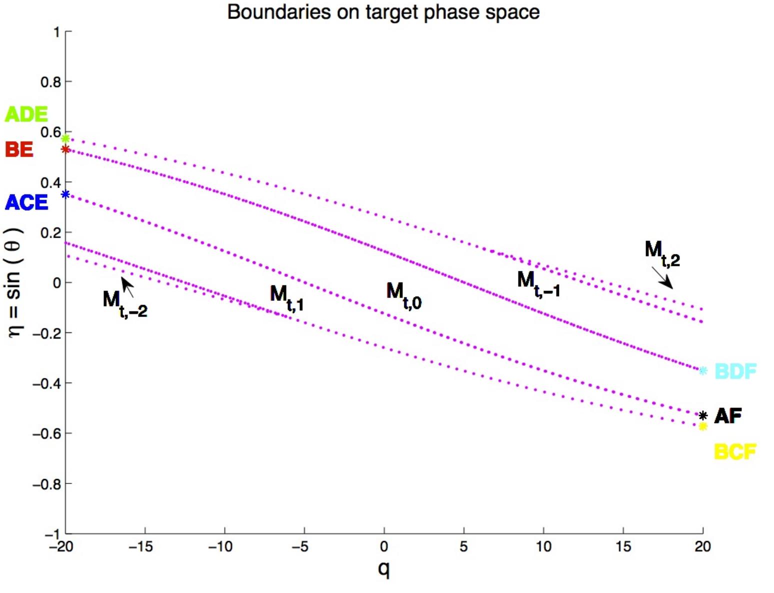

Figure B.4: Regions $M_{t,k}$ of rays that reflect $|k|$ times, for the two-faceted cup. The parameter values are: $a = 5$, $b = 20$ and $h = 40$.

Description of the research

In this thesis we studied the light propagation within optical systems. Optical engineers are interested in design systems in such a way the desired output distribution is obtained. The goal in illumination optics is to obtain the desired output distribution of light. To this purpose the ray tracing procedure is widely used. Ray tracing is a forward method where a set of rays is traced within the system from the source to the target. The propagation of light is determined computing the position and the direction of every ray for all the optical surfaces that it encounters. There are many ways to implement the ray tracing process. Monte Carlo (MC) ray tracing is often used in non-imaging optics. Rays are randomly traced from the source to the target and each time that a ray hits an optical surface the coordinates of the intersection point of the ray with the surface and the new ray direction are calculated. The output variables are computed dividing the target into intervals, the so-called bins, and counting the rays that fall into each bin. To obtain the desired accuracy, millions of rays are required, therefore the method is extremely computationally expensive and it converges as the inverse of the square root of the number of rays traced.

MC ray tracing can be improved using as sample of points a low discrepancy sequence instead of random points. Discrepancy can be interpreted as a measure of how much the sample distribution differs from a uniformly distributed sample. The discrepancy is therefore zero for uniformly distributed points. A low discrepancy sequence gives a sample of points which are regularly distributed but not exactly uniformly distributed. Quasi Monte Carlo (QMC) method considers these kind of sequences as sample of points. Therefore, QMC ray tracing is implemented tracing a set of rays whose position and direction are given by the coordinates of a low discrepancy sequence of points. The main advantage of QMC method is its rate of convergence, it is faster then MC for low dimensional problems. Nevertheless, it has some disadvantages. First, it is not easy to give an error estimation for QMC method. Second, for high dimensional spaces the QMC can become very slow. Third, it is still a binning procedure. Hence, the accuracy depends both on the number of rays traced and on the umber of bins.

In order to improve the existing methods, the phase space (PS) of the optical system is considered in this thesis. The PS of an optical surface gives information about the position and the direction of every ray on that surface where the direction is expressed with respect to the normal of the surface. In PS, the ray's direction is given by the sine of the angle that the ray forms with respect to the normal of the surface multiplied by the index of refraction of the medium in which the ray is located. In two dimensions, the PS is a two-dimensional space where the coordinates of every ray are specified by one position coordinate and one angular coordinate. For three dimensional systems the PS is a four dimensional space because every ray is specified by two position and two angular coordinates. Our idea is to use the structure of PS to trace only the rays close to the discontinuities of the luminance at the target PS. Two new approaches based on PS are presented in this work. They are tested for two-dimensional systems.

The first method is called ray tracing on PS and it is based on the source and the target PS representation of the optical system. It takes into account the sequence of optical lines that each ray hits when it propagates inside the system, that is the ray path. We note that the source and target phase spaces are partitioned into different regions each of them is formed by the rays that follow the same path. The idea is to use the edge-ray principle proved by Ries and Rabl (1994) which states that the area of these regions is conserved: all rays that are neighbors at the source PS remain close to each other at the target PS. To this purpose, a nonuniform triangulation of the source PS is constructed in such a way that new triangles are added to the triangulation only where boundaries occur. Assuming constant brightness, we only need to compute the boundaries of the regions in target PS to obtain the output photometric variables. We test the method for optical systems where both reflection and refraction laws are involved. Numerical results show that ray tracing on PS is faster and more accurate compared to MC ray tracing.

The second method employs not only the source and the target PS, but also the PS of *all* the other lines that constitute the system. All lines can be modeled as detectors of the incident light and emitters of the reflected light. Moreover, we assume that the source can only emit light and the target can only receive light. Therefore, one PS is taken into account for the source and one for the target. For the other surfaces both the source and target PS are considered. Furthermore, instead of starting from the source, the new method starts tracing back rays from target PS. In order to determine the coordinates of these rays, an inverse map from the target to the source PS is constructed as a concatenation of the maps that relate the PS of two different lines. Employing this map we are able to detect the rays that in target PS are located on the boundaries of the regions with positive luminance. First, we implement the method for systems formed by straight and reflective lines. In this particular case, the boundaries of the regions that form every PS can be computed analytically. This allows us to obtain an analytic target intensity distribution. The results are shown for a two-faceted cup and a multi-faceted cup. In both cases we note significant advantages both in terms of the accuracy and the computational time. Second, the method is developed for systems formed by curved lines. In this case the boundaries cannot be determined analytically and therefore a numerical procedure is involved. In particular, we apply a bisection method on target PS. Also in this case we compare our method to MC ray tracing and we observe significant advantages using the PS method. Finally, the ray mapping method in PS is applied to systems where also Fresnel reflection is taken into account. We obtain relevant results also in the last case.

Curriculum Vitae

Carmela Filosa was born on November 28, 1985 in Torre del greco, Italy. She finished the high school in 2003 at Liceo Scientifico Statale "G. Marconi", Colleferro. She obtained a bachelor (2008) and Master (2013) degree in Mathematics at the University of Rome "La Sapienza", Italy. In March 2014, she moved in Eindhoven (the Netherlands) to start a PhD project at the Eindhoven University of Technology in the department of Mathematics and Computer Science. The PhD project was under the supervision of Wilbert IJzerman and Jan ten Thije Boonkkamp. The research conducted in her doctoral studies was funded by Technologiestichting STW and, the daily work took place at the Centre for Analysis, Scientific computing and Applications (CASA) of TU/e and at the department of Philips Lighting of the High Tech Campus in Eindhoven. The results of her research are presented in this thesis.

Acknowledgments

Bibliography

[1] E. F. Zalewski, "Radiometry and photometry," *Handbook of optics*, vol. 2, pp. 24–1, 1995.

[2] J. Chaves, *Introduction to nonimaging optics.* CRC press, 2015.

[3] R. J. Koshel, *Illumination Engineering: design with nonimaging optics.* John Wiley & Sons, 2012.

[4] "Luminous efficacy-wikipedia the free encyclopedia," *https://commons.wikimedia.org/wiki/File:CIE 1931 Luminosity.png media/File:CIE 1931 Luminosity.png.*

[5] A. V. Arecchi, R. J. Koshel, and T. Messadi, "Field guide to illumination," SPIE, 2007.

[6] H. Zhu and P. Blackborow, "Etendue and optical throughput calculations," *Energetiq Technology, Inc., Woburn, MA*, 2011.

[7] R. P. Feynman, "Feynman lectures on physics. volume 2: Mainly electromagnetism and matter," *Reading, Ma.: Addison-Wesley, 1964, edited by Feynman, Richard P.; Leighton, Robert B.; Sands, Matthew*, 1964.

[8] M. Born and E. Wolf, *Principles of optics: electromagnetic theory of propagation, interference and diffraction of light.* Elsevier, 2013.

[9] E. Hecht, *Optics.* Parson Addison-Wesley, 2002.

[10] R. P. Feynman, R. B. Leighton, and M. Sands, *The Feynman lectures on physics, Vol. I: The new millennium edition: mainly mechanics, radiation, and heat*, vol. 1. Basic books, 2011.

[11] P. H. Jones, O. M. Maragò, and G. Volpe, *Optical tweezers: Principles and applications.* Cambridge University Press, 2015.

[12] R. Winston, J. C. Miñano, and P. Benitez, *Nonimaging optics.* Academic Press, 2005.

[13] H. Gross, *Handbook of the Optical Systems*, vol. 1. Wiley-VCH, 2005.

[14] A. B. Owen, "Quasi-monte carlo sampling," *Monte Carlo Ray Tracing: Siggraph*, vol. 1, pp. 69–88, 2003.

[15] C. M. Grinstead and J. L. Snell, *Introduction to probability.* American Mathematical Soc., 2012.

[16] G. Leobacher and F. Pillichshammer, *Introduction to quasi-Monte Carlo integration and applications.* Springer, 2014.

[17] V. M. Zolotarev, *Modern theory of summation of random variables.* Walter de Gruyter, 1997.

[18] R. Y. Rubinstein and D. P. Kroese, *Simulation and the Monte Carlo method*, vol. 10. John Wiley & Sons, 2016.

[19] D. M. Diez, C. D. Barr, and M. Cetinkaya-Rundel, *OpenIntro statistics.* CreateSpace, 2012.

[20] L. Brandolini, L. Colzani, G. Gigante, and G. Travaglini, "A koksma–hlawka inequality for simplices," in *Trends in harmonic analysis*, pp. 33–46, Springer, 2013.

[21] A. B. Owen, "Multidimensional variation for quasi-monte carlo," in *International Conference on Statistics in honour of Professor Kai-Tai FangâĂŹs 65th birthday*, pp. 49–74, 2005.

[22] P. Bratley and B. L. Fox, "Algorithm 659: Implementing sobol's quasirandom sequence generator," *ACM Transactions on Mathematical Software (TOMS)*, vol. 14, no. 1, pp. 88–100, 1988.

[23] K. B. Wolf, *Geometric optics on phase space.* Springer Science & Business Media, 2004.

[24] W. Welford and R. Winston, "On the problem of ideal flux concentrators," *JOSA*, vol. 68, no. 4, pp. 531–534, 1978.

[25] P. Benitez, R. Mohedano, J. C. Miñano, R. Garcia, and J. C. Gonzalez, "Design of cpc-like reflectors within the simultaneous multiple surface design method," in *Proc. SPIE*, vol. 3139, pp. 19–28, 1997.

[26] "Edge ray-principle-wikipedia the free encyclopedia," *https://en.wikipedia.org/wiki/Nonimaging optics Edge ray principle.*

[27] J. C. Miñano, "Two-dimensional nonimaging concentrators with inhomogeneous media: a new look," *JOSA A*, vol. 2, no. 11, pp. 1826–1831, 1985.

[28] J. C. Miñano, "Design of three-dimensional nonimaging concentrators with inhomogeneous media," *JOSA A*, vol. 3, no. 9, pp. 1345–1353, 1986.

[29] P. Davies, "Edge-ray principle of nonimaging optics," *JOSA A*, vol. 11, no. 4, pp. 1256–1259, 1994.

[30] H. Ries and A. Rabl, "Edge-ray principle of nonimaging optics," *JOSA A*, vol. 11, no. 10, pp. 2627–2632, 1994.

[31] J. C. Miñano and J. C. Gonzalez, "New method of design of nonimaging concentrators," *Applied optics*, vol. 31, no. 16, pp. 3051–3060, 1992.

[32] J. Portegies and P. Lighting, "Fast ray tracing in phase space for optical design," 2013.

[33] B. Guo, J. Menon, and B. Willette, "Surface reconstruction using alpha shapes," in *Computer Graphics Forum*, vol. 16, pp. 177–190, Wiley Online Library, 1997.

[34] X. Xu and K. Harada, "Automatic surface reconstruction with alpha-shape method," *The visual computer*, vol. 19, no. 7, pp. 431–443, 2003.

[35] C. Filosa, J. ten Thije Boonkkamp, and W. IJzerman, "A new ray tracing method in phase space using alpha-shapes," 2015.

[36] A. Lucieer and M.-J. Kraak, "Alpha-shapes for visualizing irregular-shaped class clusters in 3 d feature space for classification of remotely sensed imagery," in *Proceedings of SPIE*, vol. 5295, pp. 201–211, 2004.

[37] "Stracciatella (ice cream)," *https://en.wikipedia.org/wiki/Stracciatella (ice cream).*

[38] M. Sabel, C. Sator, T. I. Zohdi, and R. Müller, "Application of the particle finite element method in machining simulation discussion of the alpha-shape method in the context of strength of materials," *Journal of Computing and Information Science in Engineering*, vol. 17, no. 1, p. 011002, 2017.

[39] H. Edelsbrunner, D. Kirkpatrick, and R. Seidel, "On the shape of a set of points in the plane," *IEEE Transactions on information theory*, vol. 29, no. 4, pp. 551–559, 1983.

[40] H. Edelsbrunner and E. P. Mücke, "Three-dimensional alpha shapes," *ACM Transactions on Graphics (TOG)*, vol. 13, no. 1, pp. 43–72, 1994.

[41] E. P. Mücke, "Shapes and implementations in three-dimensional geometry," 1993.

[42] E. L. Lloyd, "On triangulations of a set of points in the plane," in *Foundations of Computer Science, 1977., 18th Annual Symposium on*, pp. 228–240, IEEE, 1977.

[43] P. Knabner and L. Angermann, *Numerical Methods for Elliptic and Parabolic Partial Differential Equations.* Springer Science & Business Media, 2003.

[44] D.-T. Lee and B. J. Schachter, "Two algorithms for constructing a delaunay triangulation," *International Journal of Computer & Information Sciences*, vol. 9, no. 3, pp. 219–242, 1980.

[45] R. J. Renka, "Algorithm 772: Stripack: Delaunay triangulation and voronoi diagram on the surface of a sphere," *ACM Transactions on Mathematical Software (TOMS)*, vol. 23, no. 3, pp. 416–434, 1997.

[46] W. H. Press, *Numerical recipes 3rd edition: The art of scientific computing.* Cambridge university press, 2007.

[47] S. Fortune, “Voronoi diagrams and delaunay triangulations,” *Computing in Euclidean geometry*, vol. 1, no. 193-233, p. 2, 1992.

[48] F. Cazals, J. Giesen, M. Pauly, and A. Zomorodian, “Conformal alpha shapes,” in *Point-Based Graphics, 2005. Eurographics/IEEE VGTC Symposium Proceedings*, pp. 55–61, IEEE, 2005.

[49] K. Q. Brown, “Voronoi diagrams from convex hulls,” *Information Processing Letters*, vol. 9, no. 5, pp. 223–228, 1979.

[50] “Delaunay voronoi.png,” *https://commons.wikimedia.org/wiki/File:Delaunay Voronoi.png.*

[51] H. Edelsbrunner, “Alpha shapes - a survey,” *Tessellations in the Sciences*, vol. 27, pp. 1–25, 2010.

[52] M. Teichmann and M. Capps, “Surface reconstruction with anisotropic density-scaled alpha shapes,” in *Visualization’98. Proceedings*, pp. 67–72, IEEE, 1998.

[53] D. P. Mandal and C. Murthy, “Selection of alpha for alpha-hull in $\mathbb{R}^2$,” *Pattern Recognition*, vol. 30, no. 10, pp. 1759–1767, 1997.

[54] S. Joe and F. Y. Kuo, “Notes on generating sobol sequences,” *ACM Transactions on Mathematical Software (TOMS), 29 (1), 49*, vol. 57, 2008.